COMMUNICATIONS IN COMPUTATIONAL PHYSICS
Vol. **3**, No. 3, pp. 519-581

Commun. Comput. Phys.
March 2008

Study of Simple Hydrodynamic Solutions with the Two-Relaxation-Times Lattice Boltzmann Scheme

Irina Ginzburg[1,*], Frederik Verhaeghe[2] and Dominique d'Humières[3]

[1] *Cemagref, Antony Regional Centre, Parc de Tourvoie – BP 44, 92163 Antony Cedex, France.*
[2] *Department of Metallurgy and Materials Engineering, Katholieke Universiteit Leuven, Kasteelpark Arenberg 44, 3001, Leuven, Belgium.*
[3] *Laboratoire de Physique Statistique, École Normale Supérieure, associated to CNRS and P. and M. Curie and D. Diderot Universities, 24 Rue Lhomond, 75231 Paris Cédex 05, France.*

Received 14 March 2007; Accepted (in revised version) 22 July 2007

Communicated by Shiyi Chen

Available online 30 October 2007

Abstract. For simple hydrodynamic solutions, where the pressure and the velocity are polynomial functions of the coordinates, exact microscopic solutions are constructed for the two-relaxation-time (TRT) Lattice Boltzmann model with variable forcing and supported by exact boundary schemes. We show how simple numerical and analytical solutions can be interrelated for Dirichlet velocity, pressure and mixed (pressure/tangential velocity) multi-reflection (MR) type schemes. Special care is taken to adapt them for corners, to examine the uniqueness of the obtained steady solutions and staggered invariants, to validate their exact parametrization by the non-dimensional hydrodynamic and a "kinetic" (collision) number. We also present an inlet/outlet "constant mass flux" condition. We show, both analytically and numerically, that the kinetic boundary schemes may result in the appearance of Knudsen layers which are beyond the methodology of the Chapman-Enskog analysis. Time dependent Dirichlet boundary conditions are investigated for pulsatile flow driven by an oscillating pressure drop or forcing. Analytical approximations are constructed in order to extend the pulsatile solution for compressible regimes.

PACS: 47.10.ad, 47.56+r, 02.60-x

Key words: Lattice Boltzmann equation, Dirichlet boundary conditions, pressure boundary conditions, two-relaxation-time model, Knudsen layers, exact hydrodynamic solutions, staggered invariants, pulsatile flow.

*Corresponding author. *Email addresses:* `irina.ginzburg@cemagref.fr` (I. Ginzburg), `frederik.verhaeghe@mtm.kuleuven.be` (F. Verhaeghe), `dominiq@lps.ens.fr` (D. d'Humières)

1 Introduction

Lattice Boltzmann multi-relaxation-time (MRT) models were derived from their Lattice Gas predecessor [7] in pioneering works [19, 20, 30]. These models are simple and efficient, explicit in time, numerical schemes for solving the hydrodynamic Navier-Stokes equations in two [21, 27] and three dimensions [22, 23]. When the collision operator is chosen properly, only a few relaxation parameters are related to the transport coefficients of the derived macroscopic conservation laws, e.g., bulk and kinematic viscosities, and the remaining collision parameters can be viewed as "kinetic" degrees of freedoms. They principally distinguish the method from the direct discretization methods, such as, e.g., finite-difference schemes. Although it was rapidly recognized that the "kinetic" degrees of freedom have a determinant impact on the effective accuracy of microscopic boundary schemes (see [9–11]) and play a significant role for stability [23, 27, 28], the BGK scheme [34] without any kinetic degree of freedom still dominates the modeling of incompressible flow and transport phenomena in porous media. Recently, the MRT model based on the polynomial equilibrium functions [21, 23, 34] attracted more attention for solving complex, single and multiphase problems, e.g., in [29, 31–33, 38–40, 42]. The reader can also find in [37] an exhaustive review on the possibility to increase the stability of the BGK model at low viscosity with the help of an alternative, entropy based, equilibrium.

The main goal of this study is to validate the microscopic solutions and Dirichlet boundary schemes on simple problems with analytical solutions. The multi-reflection type (MR) boundary schemes [16] are constructed in the context of the two-relaxation-time (TRT) linear collision operator [12–15] where they are especially simple and efficient. The TRT operator is suitable for both hydrodynamic and advection-diffusion problems and can be regarded as a bridge between MRT and BGK. TRT shares the simplicity of BGK, but possesses one free collision parameter which plays a crucial role for the overall accuracy and stability, at least for incompressible flow.

We apply the methodology developed in [6, 8, 9, 11, 13, 16], both to construct exact solutions of the MRT/TRT models and to verify the effective accuracy of the boundary schemes. Its key point lies in using the Chapman-Enskog expansion [7, 21] which expresses each individual population in the bulk via its local equilibrium value and its gradients. Based on a parity argument and in the framework of the TRT model, infinite Chapman-Enskog series takes a very simple link-wise form [16], independent of the nature of the equilibrium distribution. When the expected steady solutions for the pressure and velocity are polynomial functions of the coordinates, the expansion has only a finite number of terms. Substituting the truncated, but exact, series into the microscopic boundary rule, we derive the solution for the incoming populations in such problems.

The simplest situation takes place when the derived closure condition, i.e., the difference between the expected one from the Chapman-Enskog analysis and the one obtained from the incoming population, fits the directional Taylor expansion with respect to the local equilibrium component (e.g., for velocity or pressure). The coefficients of

the closure relation depend, in general, on the values of the relaxation times, the equilibrium/source weights and the coefficients of the involved microscopic boundary rule. It was first shown for Stokes equilibrium in [6] that the bounce-back locates the parallel boundaries in Couette flow midway the link, whereas the *effective location* or, equivalently, the *effective slip velocity*, depends on the kinematic viscosity and the probability p for a mixture of bounce-back and specular reflections (this or similar condition is called also "diffusive" or "kinetic" scheme, e.g., in [35, 36]). However, using the bounce-back rule, the effective width of the parabolic and, in particular, Poiseuille flow, depends on a special combination of the two relaxation times (hereafter called Λ_{eo}). These relaxation times govern the evolution of the stress and energy fluxes and they are the two collision rates of the TRT operator. For diffusion schemes, the effective location of zero velocity depends not only on the Λ_{eo} value, but also on the viscosity, probability p and grid resolution of the channel. Besides that, the effective width differs for parallel and rotated channels, e.g., by 45°.

The exact Poiseuille solution set by simple reflections can be found in [8, 9, 11, 18] for the bounce-back rule and in [8] for a diffusive boundary. Once the linear or parabolic flows are established, the difference between the assumed "wall" velocity and the effective one, obtained at this location, can be expressed exactly via the first and second "wall" gradients, for any boundary scheme. When modeling hydrodynamic boundary conditions, this mismatch can be interpreted as an error in the location of the Dirichlet boundary values at the wall. In contrast, for the BGK operator, it is fitted, e.g, in [2,35,36], to boundary layer continuum solutions [5, 26]. The coefficients associated with the first and second derivatives in the continuous relations are proportionally to Kn and Kn^2, respectively, where the Knudsen number Kn is proportional to the kinematic viscosity and to the inverse of the channel width. For the BGK, the coefficient Λ_{eo}, appearing in the closure relation with the second derivatives, becomes proportional to the square of the viscosity, giving rise to a "kinetic" interpretation of the closure relations in the hope it can be suitable for modeling microflows. However we emphasize that Λ_{eo} is a free parameter of the TRT and MRT operators. Its particular value, $\Lambda_{eo} = \frac{3}{16}$, enables the bounce-back to locate the prescribed slip velocity exactly midway the link. As one more example, we extend in this paper this solution to linear, based on two-three populations, schemes [4, 16, 41]. The solution $\Lambda_{eo} = \frac{3}{4}\delta_q^2$ locates then the slip-velocity at any prescribed distance $\delta_q > 0$ for "magic" linear schemes [16], with no "boundary layers". We show in this paper how to modify the coefficients of linear schemes for arbitrary rotated Poiseuille flow. This can be achieved also with "parabolic" schemes [10, 11, 16] due to their third-order accuracy.

Usually, a more difficult situation takes place when the incoming population and its Chapman-Enskog solution do not match, developing corrections to the bulk solution, called hereafter Knudsen layers. The appearance of Knudsen layers in a shear flow for a perpendicular orientation of the boundaries was first demonstrated, both analytically and numerically, in [6]. We present here another example, when the correction appears in *parallel* Poiseuille flow, due to the inaccuracy of the multi-reflection schemes with re-

spect to second- and higher-order gradients of the non-linear (Navier-Stokes) equilibrium term. A similar situation takes place for the Couette flow. One remarkable property of this TRT Knudsen layer is that it has not any impact on the macroscopic solution. In other words, the parallel Poiseuille profiles obtained with the Stokes and Navier-Stokes equilibrium coincide for all the multi-reflection boundary schemes considered here, including bounce-back.

Constructing the populations, we get the exact solution not only for the velocity, but also for all the other MRT moments. This enable us to get the Knudsen layer corrections which obey exact link-wise finite-difference type recurrence TRT equations [16] but lie beyond the Chapman-Enskog solution. At the same time, velocity profiles for Couette and Poiseuille flows based on the non-linear equilibrium and the link-wise, in [18], or the diffusion type schemes, in [35], are obtained via the alternative techniques, solving analytically the finite-difference equivalent of 1D BGK equation with respect to the velocity. Both approaches lead to the same velocity solutions for equivalent collision and boundary configurations.

Dropping the Chapman-Enskog expansion at a prescribed order, our methodology naturally applies for the analysis and design of boundary schemes. With its help, the multi-reflection type (MR) approach [11] is further developed for Dirichlet velocity conditions and extended for pressure and mixed (pressure/tangential velocity) Dirichlet conditions in [16]. Each multi-reflection condition specifies a linear combination of the known populations along the outgoing direction for the incoming population. The mixed scheme computes the incoming population as a linear combination of the pressure and velocity multi-reflections, involving then the whole set of locally cut links for each individual incoming population. Every prescribed solution defines a closure relation. Fitting a closure relation to the directional Taylor expansion, the space and time errors with respect to the desired Dirichlet condition are first obtained in a general form. Through an appropriate selection of the coefficients, families of second- and third-order accurate, pressure and velocity boundary schemes are specified.

We show in [16] that the hydrodynamic non-dimensional numbers (Reynolds, Froude, Mach) and the selected Λ_{eo} value completely define the non-dimensional TRT steady solutions for pressure and velocity on a given grid. In the Stokes regime, the coefficients of the Darcy law (i.e., the components of the permeability tensor) do not depend on the specified viscosity value, a well known artifact of the BGK model for computations in porous media (see [11, 32]), provided that the exact microscopic closure relations share the parametrization properties of the TRT bulk solutions. Bounce-back, the five populations based multi-reflection (MR1 in [11]) and new velocity and pressure schemes maintain the parametrization of the bulk solutions exactly. A special local correction yields this property for linear interpolations [4, 41].

The paper is organized as follows. The next section overviews the TRT model and the multi-reflection algorithms: the Dirichlet velocity ($M_q^{(u)}$), the Dirichlet pressure ($M_q^{(p)}$) and the mixed ($M_q^{(m)}$) schemes. A "constant mass flux" condition is discussed in Sec-

tion 2.7. Steady solutions in open and closed boxes, using the Dirichlet velocity and mixed boundary schemes, are evaluated in Section 3, for Poiseuille flow and for linear velocity/parabolic pressure Navier-Stokes solution, and in Appendix A for the "solid rotation" problem. The pulsatile flow is studied in Section 4. It can be viewed as an approximation for blood-flow, e.g., in [3, 43]. Several analytical approximations for the solution of the compressible Stokes equation driven by an oscillating pressure gradient are constructed in Appendix B.

2 Overview of the algorithms

2.1 The TRT model

We assume that the nodes $\vec{r}$ of the regular $d-$dimensional computational grid are connected by velocity vectors $\{\vec{c}_q\}$. The TRT evolution equation [12, 13, 16] describes the relaxation of the populations $\{f_q\}$ to prescribed equilibrium functions $\{e_q^{\pm}\}$:

$$\begin{aligned}
&f_q(\vec{r}+\vec{c}_q,t+1)=\tilde{f}_q(\vec{r},t), \quad \tilde{f}_q(\vec{r},t)=f_q(\vec{r},t)+p_q+m_q^{(F)},\\
&p_q=\lambda_e n_q^+, \quad m_q=\lambda_o n_q^-, \quad m_q^{(F)}=m_q+S_q^-,\\
&f_q=f_q^++f_q^-, \quad f_q^{\pm}=\frac{1}{2}(f_q\pm f_{\bar{q}}), \quad n_q^{\pm}=f_q^{\pm}-e_q^{\pm},\\
&\vec{c}_0=\vec{0}, \quad f_0=f_0^+, \quad f_0^-=0, \quad \vec{c}_q=-\vec{c}_{\bar{q}}, \quad q=0,\cdots,Q-1.
\end{aligned} \tag{2.1}$$

The collision operator has two eigenvalues, λ_e and λ_o. Conditioned by linear stability, the eigenvalue functions Λ_e and Λ_o are positive:

$$\Lambda_e=-(\frac{1}{2}+\frac{1}{\lambda_e}), \quad \Lambda_o=-(\frac{1}{2}+\frac{1}{\lambda_o}), \quad \Lambda_{eo}=\Lambda_e\Lambda_o, \quad -2\le\lambda_e<0, \quad -2\le\lambda_o<0. \tag{2.2}$$

For any prescribed distribution of the external forcing $\vec{F}(\vec{r},t)$ and any selected source variable S_q^-, we define the equivalent equilibrium functions:

$$\begin{aligned}
&e_q^+=\Pi_q^\star(\rho,\vec{j},\rho_0), \quad e_0^+=e_0=\rho-\sum_{q=1}^{Q-1}e_q^+, \quad \rho=\sum_{q=0}^{Q-1}f_q,\\
&\Pi_q^\star(\rho,\vec{j},\widehat{\rho})=t_q^\star(c_s^2\rho+g_S E_q^+(\vec{j},\widehat{\rho})), \quad E_q^+(\vec{j},\widehat{\rho})=\widehat{\rho}\frac{3u_q^2-||\vec{u}||^2}{2}, \quad u_q=(\vec{u}\cdot\vec{c}_q),\\
&\vec{u}=\frac{\vec{j}}{\widehat{\rho}}, \quad \vec{j}=\vec{J}+\frac{\vec{F}}{2}, \quad \vec{J}=\sum_{q=1}^{Q-1}f_q\vec{c}_q, \quad S_q^-=t_q^\star(\vec{\mathcal{F}}\cdot\vec{c}_q), \quad \sum_{q=1}^{Q-1}S_q^-\vec{c}_q=\vec{\mathcal{F}},\\
&e_q^-=j_q^{\mathrm{eq}\star}, \quad j_q^{\mathrm{eq}\star}=t_q^\star j_q^{\mathrm{eq}}, \quad j_q^{\mathrm{eq}}=(\vec{j}^{\mathrm{eq}}\cdot\vec{c}_q), \quad \vec{j}^{\mathrm{eq}}=\vec{j}+\Lambda_o\vec{F}+\frac{\vec{\mathcal{F}}}{\lambda_o}.
\end{aligned} \tag{2.3}$$

This yields the same solutions for $f_q^{\pm}$, p_q and $m_q^{(F)}$ for any $\vec{\mathcal{F}}$. Hereafter, we will use:

$$F_q^\star = t_q^\star F_q, \quad F_q = (\vec{F}\cdot\vec{c}_q), \quad j_q^\star = t_q^\star j_q, \quad j_q = (\vec{j}\cdot\vec{c}_q).$$

Assuming that c_s^2 is a free parameter, the isotropic weights $t_q^\star$ follow [34]: $\{t_I^\star=\frac{1}{3}, t_{II}^\star=\frac{1}{12}\}$ for $d2Q9$, $\{t_I^\star=\frac{1}{3}, t_{III}^\star=\frac{1}{24}\}$ for $d3Q15$, $\{t_I^\star=\frac{1}{6}, t_{II}^\star=\frac{1}{12}\}$ for $d3Q19$, where the Roman numbers are equal to $||\vec{c}_q||$. The exact mass and momentum conservation relations of the TRT model (2.1),(2.3) are:

$$\sum_{q=0}^{Q-1} p_q(\vec{r},t)=0, \quad \sum_{q=1}^{Q-1} m_q^{(F)}(\vec{r},t)\vec{c}_q=\vec{F}. \tag{2.4}$$

Their hydrodynamic approximation is obtained via the Chapman-Enskog analysis and presented in [14, 16]. In this paper, using the Dirichlet velocity and mixed boundary conditions, we will study the TRT modeling of steady solutions for the incompressible Stokes ($g_S=0$) and Navier-Stokes ($g_S=1$) equations:

$$\begin{aligned} &\nabla\cdot\vec{u}=0, \quad \vec{u}=\frac{\vec{j}}{\rho_0}, \\ &g_S\nabla\cdot(\vec{u}\otimes\vec{u})+\frac{1}{\rho_0}(\nabla P-\vec{F})=\nu\Delta\vec{u}, \quad P=c_s^2\rho, \quad \nu=\frac{1}{3}\Lambda_e, \end{aligned} \tag{2.5}$$

and for the compressible time-dependent Stokes-type equation:

$$\frac{1}{\rho_0}\partial_t P+c_s^2\nabla\cdot\vec{u}=0, \quad \vec{u}=\frac{\vec{j}}{\rho_0}, \tag{2.6}$$

$$\partial_t\vec{u}+\frac{1}{\rho_0}(\nabla P-\vec{F})=\nu\Delta\vec{u}+\nu_\xi\nabla\nabla\cdot\vec{u}, \quad \nu_\xi=\Lambda_e(\frac{2}{3}-c_s^2). \tag{2.7}$$

For the TRT, the bulk viscosity ν_ξ is equal to the kinematic viscosity ν when $c_s^2=\frac{1}{3}$. The eigenvalue λ_e, associated with the symmetric collision component, is fixed by the choice of the kinematic viscosity. The eigenvalue λ_o, associated with the anti-symmetric collision component, then the eigenvalue function Λ_o or the eigenvalue combination Λ_{eo}, represent a free "kinetic" parameter.

The non-dimensional solutions $\vec{j}'=\frac{\vec{j}}{\rho_0 U}$ and $P'=\frac{P-P_0}{\rho_0 U^2}$ are "physical" when they are determined by the non-dimensional parameters of the modeled equations (e.g., Reynolds $Re=UL/\nu$ and Froude number $Fr=U^2/Lg$ for incompressible flow), independently of the individual choice of the relaxation parameters. We show in [16] that all higher-order terms in the *exact non-dimensional steady macroscopic mass and momentum equations* (i.e., the terms beyond Eq. (2.5)) depend on the collision eigenvalues only via their combination Λ_{eo}. For time dependent equations, this is true only for the coefficients of the spatial derivatives, in general. The non-dimensional steady solutions of the TRT operator on a

given grid are identical when, in addition to the hydrodynamic numbers, the collision function Λ_{eo} is fixed, provided that the closure relations obey the parametrization properties of the TRT evolution operator. For Stokes flow, if one maintains a fixed value for Λ_{eo}, the stationary distribution $\nu\vec{j}(\vec{r})$ is then independent from the individual values assigned to Λ_e and Λ_o. This is not possible for the BGK operator. With TRT, this can be achieved because of the freedom in the selection of λ_o, then Λ_{eo}.

2.2 Multi-reflection boundary schemes, MR

Before performing the MR at a boundary grid node $\vec{r}_{\rm b}$, one must determine the local set $\{\vec{c}_q\}$ of outgoing links (cut by the solid wall) and, for each cut link, prescribe the distance δ_q to the wall and the type of Dirichlet boundary condition (e.g., velocity or pressure). We will distinguish *standard* links and *special* links. The cut links with two available neighbors are called "standard". The *first type* of special links does not have a second grid neighbor and the *second type* of special links does not have a first grid neighbor. This means that the nodes $(\vec{r}_{\rm b}-2\vec{c}_q)$ and $(\vec{r}_{\rm b}-\vec{c}_q)$, respectively, are outside the computational grid. Depending on the type of the cut link $\{\vec{c}_q,\vec{c}_{\bar{q}}\}$ and the desired accuracy, one selects a particular scheme, $M_q^{(u)}$ (velocity) or $M_q^{(m)}$ (mixed: pressure/tangential velocity), for each incoming solution.

We will say that the MR scheme is characterized by the triplet $j^{(n)}/\Pi^{(k)}/F^{(l)}$ when each incoming population matches exactly the steady solution expansion for $\mathcal{O}(\partial_q^{(n-1)}j_q^\star)$, $\mathcal{O}(\partial_q^{(k-1)}\Pi_q^\star)$ and $\mathcal{O}(\partial_q^{(l-1)}F_q^\star)$ terms. It is noted that in case of *linear Stokes equilibrium* ($g_S=0$), *second-order accuracy* ($j^{(2)}/\Pi^{(1)}/F^{(0)}$) allows to match *exactly* linear velocity and constant pressure solutions when the forcing is absent. *The third-order accuracy* ($j^{(3)}/\Pi^{(2)}/F^{(1)}$) is needed for parabolic velocity and linear pressure distribution when the forcing is uniform.

2.3 Dirichlet velocity condition, $M_q^{(u)}$ schemes

These schemes prescribe the boundary velocity value $\vec{u}^b(\vec{r}_{\rm w},\widehat{t})$ via $M_q^{(u)}$ solution for incoming population $f_{\bar{q}}(\vec{r}_{\rm b},t+1)$:

$$\begin{aligned}
&f_{\bar{q}}(\vec{r}_{\rm b},t+1)=M_q^{(u)}(\vec{r}_{\rm b},t),\quad q\in\Pi^{(u)},\quad \vec{r}_{\rm w}=\vec{r}_{\rm b}+\delta_q\vec{c}_q,\\
&M_q^{(u)}(\vec{r}_{\rm b},t)=R_q(\vec{r}_{\rm b},t)+f_q^{\rm p.c.(u)}(\vec{r}_{\rm b},t)+w_q^{(u)}(\vec{r}_{\rm w},\widehat{t}),\\
&R_q(\vec{r}_{\rm b},t)=\kappa_1\tilde{f}_q(\vec{r}_{\rm b},t)+\kappa_0\tilde{f}_q(\vec{r}_{\rm b}-\vec{c}_q,t)+\kappa_{-1}\tilde{f}_q(\vec{r}_{\rm b}-2\vec{c}_q,t)\\
&\qquad\qquad+\bar{\kappa}_{-1}\tilde{f}_{\bar{q}}(\vec{r}_{\rm b},t)+\bar{\kappa}_{-2}\tilde{f}_{\bar{q}}(\vec{r}_{\rm b}-\vec{c}_q,t),\\
&w_q^{(u)}=-\alpha^{(u)}t_q^\star\rho_0u_q^b,\quad u_q^b=(\vec{u}^b(\vec{r}_{\rm w},\widehat{t})\cdot\vec{c}_q),\\
&\alpha^{(u)}=\kappa_1+\kappa_0-\bar{\kappa}_{-1}+\kappa_{-1}-\bar{\kappa}_{-2}+1.
\end{aligned}\tag{2.8}$$

Table 1: The coefficients κ_0, κ_{-1}, $\bar{\kappa}_{-1}$, $\bar{\kappa}_{-2}$, and the valid range for δ_q for the Dirichlet velocity $M_q^{(u)}$ schemes. The missing coefficient is $\kappa_1 = 1-\kappa_0-\kappa_{-1}-\bar{\kappa}_{-1}-\bar{\kappa}_{-2}$.

$M_q^{(u)}$	κ_0	κ_{-1}	$\bar{\kappa}_{-1}$	$\bar{\kappa}_{-2}$	δ_q
BB	0	0	0	0	$\delta_q=1/2$
ULI,MGULI,MULI	$1-2\delta_q$	0	0	0	$0\le\delta_q\le 1/2$
DLI,MGDLI,MDLI	0	0	$\frac{2\delta_q-1}{2\delta_q}$	0	$1/2\le\delta_q$
YLI,MGYLI, MYLI	$\frac{1-\delta_q}{1+\delta_q}$	0	$\frac{\delta_q}{1+\delta_q}$	0	$0\le\delta_q\le 1$
CLI,MCLI	$\frac{1-2\delta_q}{1+2\delta_q}$	0	$-\kappa_0$	0	$0\le\delta_q\le 1$
MGMR(C)	$\frac{1-2\delta_q-2\delta_q^2-4C\Lambda_o}{(1+\delta_q)^2-2C\Lambda_o}$	$\frac{2C\Lambda_o+\delta_q^2}{(1+\delta_q)^2-2C\Lambda_o}$	$\frac{-1+2\delta_q+2\delta_q^2-4C\Lambda_o}{(1+\delta_q)^2-2C\Lambda_o}$	$\frac{2C\Lambda_o-\delta_q^2}{(1+\delta_q)^2-2C\Lambda_o}$	$0\le\delta_q\le 1$
MR1	$\frac{1-2\delta_q-2\delta_q^2}{(1+\delta_q)^2}$	$\frac{\delta_q^2}{(1+\delta_q)^2}$	$-\kappa_0$	$-\kappa_{-1}$	$0\le\delta_q\le 1$

A two-point equivalent form for $R_q(\vec{r}_b,t)$ is presented in [11, 16]. The $M_q^{(u)}$ solution is computed independently for each cut link as follows:

1. Compute the coefficients $\kappa_1-\bar{\kappa}_{-2}$ from Table 1.
2. Compute $w_q^{(u)}(\vec{r}_w,\widehat{t})=-\alpha^{(u)}t_q^\star\rho_0 u_q^b$ ($\widehat{t}$ is discussed for time dependent boundary conditions in Section 4.1.2).
3. If necessary, compute $f_q^{\text{p.c.}}$ as given in Table 2 using $m_q^{(F)}$ and $F_q^\star$, pre-computed during the collision step.
4. Compute $M_q^{(u)}(\vec{r}_b,t)$ with relations (2.8).

Table 1 summarizes the coefficients of the principal $M_q^{(u)}$ schemes: bounce-back (BB), several linear interpolations from three populations based LI($\alpha^{(u)}$)−family: ULI/DLI from [4], YLI from [41], then CLI, MGULI/MGDLI and MGYLI schemes from "magic" linear sub-family MGLI($\alpha^{(u)}$) built in [16]. It is noted that the following schemes coincide: ULI and YLI for $\delta_q=0$, DLI and YLI for $\delta_q=1$, ULI/DLI, CLI and BB for $\delta_q=\frac{1}{2}$. The (*modified*) MLI($\alpha^{(u)}$) schemes (e.g., MULI/MDLI, MYLI, MCLI) are built in [16] with the coefficients of their LI−counterparts. They remove the second-order error of the LI($\alpha^{(u)}$) family, with the help of the finite-difference approximations. In principle, there is an infinite number of three populations based schemes of equivalent (second-order) accuracy, and therefore, an infinite number of LI($\alpha^{(u)}$) and MLI($\alpha^{(u)}$) schemes, governed by the choice of $\alpha^{(u)}$.

Then follow five populations based schemes: sub-family MGMR(C) and its special member MR1, they represent the MR(k) family [11, 16]. The MGMR(C) sub-family is governed by a free parameter C, related to k and then to $\alpha^{(u)}$, where

$$k=\frac{1}{2}(1+\delta_q)^2-1-C\Lambda_o,\quad \alpha^{(u)}=\frac{2}{1+k}.$$

The coefficients of R_q in relation (2.8) lie inside the heuristic stability interval when $C^{min}\leq C\Lambda_o\leq 0$ and

$$C^{min}=\begin{cases} -2\delta_q-\frac{3}{2}\delta_q^2 & \text{for } 0\leq\delta_q\leq\delta_0, \\ \frac{\delta_q^2}{2}-1 & \text{for } \delta_0\leq\delta_q\leq 1, \end{cases}$$

where $\delta_0=(\sqrt{3}-1)/2$. The limit $C=0$ corresponds to MR1 scheme [11]. When $\delta_q=0$ then $C=0$ and MGMR(C) reduces to MR1. The MR1 coincides with MCLI when $\delta_q=0$. When $C=\delta_q$ then a particular MGMR2 scheme becomes exact for the parabolic velocity and pressure distributions but it remains stable only for very small Λ_o values: when $\Lambda_o\to 0$ then

$$\kappa_1=\frac{(1+\delta_q)^2+2C\Lambda_o}{(1+\delta_q)^2-2C\Lambda_o}\to 1.$$

In what follows we will refer to the LI($\alpha^{(u)}$) family as *second-order or linear* schemes and MR(k) and MLI($\alpha^{(u)}$) families as *third-order or parabolic* schemes. Parametrization properties of $M_q^{(u)}$ schemes are related to value of the coefficient $\beta^{(p\star)}$ (see in Table 2):

$$\beta^{(p\star)}=\frac{\beta^{(p)}}{\alpha^{(u)}},\quad \beta^{(p)}=-(\kappa_0+2\kappa_{-1}+\bar{\kappa}_{-2}+1)+\alpha^{(u)}(\frac{1}{2}-\Lambda_o). \tag{2.9}$$

We show in [16] that BB and CLI yield the exact parametrization of the bulk solutions with $\beta^{(p\star)}=-\Lambda_o$. Other schemes from MGLI($\alpha^{(u)}$) family modify the effective $\beta^{(p\star)}$ values with the help of the special corrections $f_q^{\text{p.c.}(u)}$, given in Table 2. They improve then the deficiency of ULI/DLI and YLI, respectively. The sub-families MGMR(C) and MLI($\alpha^{(u)}$) family yield the exact parametrization as well.

One should keep in mind that the solutions are identical using the distinct boundary schemes if their *exact* microscopic closure relations are equivalent. We recall from [16] that *steady solutions* are equal, respectively, for

1. CLI and MGLI($\alpha^{(u)}$), e.g., {MGULI/MGDLI,MGYLI}.
2. MCLI and MLI($\alpha^{(u)}$), e.g., {MULI/MDLI,MYLI}.

Below, we work with the following configurations:

1. For the link which goes through corner we prescribe the $M_q^{(u)}$ scheme (selected for one of the adjacent walls). A combination of two (or more) $M_q^{(u)}$ schemes is possible, but omitted for the sake of simplicity.
2. The MR(k) family replaces $\kappa_{-1}\tilde{f}_q(\vec{r}_b-2\vec{c}_q,t)$ with $\kappa_{-1}f_q(\vec{r}_b-\vec{c}_q,t)$ for the *first-type links*. MR(k) is switched to the MLI family for the *second-type links* (typically, to MCLI or MULI/MDLI).
3. The MLI($\alpha^{(u)}$) and LI($\alpha^{(u)}$) families replace $\kappa_0\tilde{f}_q(\vec{r}_b-\vec{c}_q,t)$ with $\kappa_0 f_q(\vec{r}_b,t)$ for the *second-type links*:

$$R_q(\vec{r}_b,t)=\kappa_1\tilde{f}_q(\vec{r}_b,t)+\kappa_0 f_q(\vec{r}_b,t)+\bar{\kappa}_{-1}\tilde{f}_{\bar{q}}(\vec{r}_b,t). \tag{2.10}$$

Table 2: Summary of the values of $f_q^{\mathrm{p.c.}(u)}$, $\alpha^{(u)}$ and $\beta^{(p\star)}$ and the accuracy of the different $M_q^{(u)}$ schemes. The $f_q^{\mathrm{p.c.}(u)}$ correction is computed with $m_q^{(F)}=m_q+S_q^-$, $S_q^-=t_q^\star(\vec{\mathcal{F}}\cdot\vec{c}_q)$, $\forall\vec{\mathcal{F}}$. It is noted that $m_q^{(F)}-F_q^\star=m_q$ if $\vec{\mathcal{F}}=\vec{F}$, i.e., $\vec{j}^{\mathsf{eq}}=\vec{J}$. The coefficients $\alpha^{(u)}$ and $\beta^{(p\star)}$ are equal for the schemes with equal coefficients $\kappa_1-\bar{\kappa}_{-2}$, e.g., YLI and {MGYLI, MYLI}, ULI/DLI and {MGULI/MGDLI}, {MULI/MDLI}, respectively.

$M_q^{(u)}$	$f_q^{\mathrm{p.c.}(u)}$	$\alpha^{(u)}$	$\beta^{(p\star)}$	accuracy
BB, $\delta_q=\frac{1}{2}$	0	2	$-\Lambda_o$	$j^{(2)}/\Pi^{(1)}/F^{(0)}$
ULI	0	2	$-\Lambda_o-\lvert\frac{1}{2}-\delta_q\rvert$	$j^{(2)}/\Pi^{(1)}/F^{(0)}$
DLI	0	$\frac{1}{\delta_q}$	$-\Lambda_o-\lvert\frac{1}{2}-\delta_q\rvert$	
YLI	0	$\frac{2}{1+\delta_q}$	$-\Lambda_o-\frac{1}{2}$	
CLI	0	$\frac{4}{1+2\delta_q}$	$-\Lambda_o$	
MGLI($\alpha^{(u)}$):	$-\alpha^{(u)}(\beta^{(p\star)}+\Lambda_o)m_q^{(F)}$			$j^{(2)}/\Pi^{(1)}/F^{(0)}$
MGULI/MGDLI	$\alpha^{(u)}\lvert\frac{1}{2}-\delta_q\rvert m_q^{(F)}$			
MGYLI	$\frac{1}{2}\alpha^{(u)}m_q^{(F)}$			
MLI($\alpha^{(u)}$):	$-\alpha^{(u)}(\beta^{(p\star)}m_q^{(F)}+\Lambda_o F_q^\star-\frac{\delta_q^2}{2}\partial_q^{2\,f.d}j_q^\star)$			$j^{(3)}/\Pi^{(2)}/F^{(1)}$
MR(k):	$-\alpha^{(u)}\Lambda_o(m_q^{(F)}-F_q^\star)$		$-\Lambda_o$	$j^{(3)}/\Pi^{(2)}/F^{(1)}$
MR1		$\frac{4}{(1+\delta_q)^2}$		
MGMR(C)		$\frac{4}{(1+\delta_q)^2-2C\Lambda_o}$		
MGMR2		$\frac{4}{(1+\delta_q)^2-2\delta_q\Lambda_o}$		$j^{(3)}/\Pi^{(3)}/F^{(1)}$

4. The MLI($\alpha^{(u)}$) family computes $\partial_q^2 j_q^\star$ for $f_q^{\mathrm{p.c.}(u)}$ using the following approximation (excepted for the second-type links):

$$\partial_q^{2\,f.d}j_q^\star(\widehat{t})\approx\frac{2}{\delta_q+\delta_{\bar{q}}}\Big(\frac{j_q^\star(\vec{r}_{\mathrm{w}},\widehat{t})-j_q^\star(\vec{r}_{\mathrm{b}},\widehat{t})}{\delta_q}-\frac{j_q^\star(\vec{r}_{\mathrm{b}},\widehat{t})-j_q^\star(\vec{r}_{\bar{\mathrm{w}}},\widehat{t})}{\delta_{\bar{q}}}\Big)+\mathcal{O}(\varepsilon^3),\qquad(2.11)$$
$$\vec{r}_{\mathrm{w}}=\vec{r}_{\mathrm{b}}+\delta_q\vec{c}_q,\quad\vec{r}_{\bar{\mathrm{w}}}=\vec{r}_{\mathrm{b}}+\delta_{\bar{q}}\vec{c}_{\bar{q}},\quad\delta_q\neq0,\quad\delta_{\bar{q}}\neq0.$$

5. For the second-type links we switch relations (2.11) to the non-directional finite-difference approximations:

$$\partial_q^2 j_q^\star(\vec{r}_{\mathrm{b}},\widehat{t})\approx-\frac{m_q^{(F)}-\partial_q{}^{f.d}\Pi_q^\star}{\Lambda_e},\quad\partial_q{}^{f.d}\Pi_q^\star=-\sum_{\alpha=1}^{d}\partial_\alpha^{f.d}\Pi_q^\star c_{\bar{q}\alpha},\qquad(2.12)$$
$$\partial_\alpha^{f.d.}\Pi_q^\star c_{\bar{q}\alpha}=\Pi_q^\star(\vec{r}_{\mathrm{b}}+c_{\bar{q}\alpha},\widehat{t})-\Pi_q^\star(\vec{r}_{\mathrm{b}},\widehat{t}).$$

We set $\widehat{t}$ equal to t (already known solution) in relations (2.11)-(2.12) for the sake of simplicity. The finite difference (f.d) approximation $\partial_\alpha^{f.d}\Pi_q^\star$ is available excepted for very special local geometries (e.g., sharp corners), where MLI can be switched to LI.

6. It is shown in [16] that when applying directly the MR(k) and MLI($\alpha^{(u)}$) schemes at solid grid nodes ($\delta_q = 0$), where their closure relation is *exact* ($u_q(\vec{r}_b) \equiv u_q^b$), the uniqueness of the steady solutions can be lost. Indeed, the non-equilibrium component $n_q^-(\vec{r}_w,t)$ is then conserved in standard boundary nodes for the links perpendicular to the wall.

2.4 "Magic" solutions for linear velocity schemes

Particular Λ_{eo} values enable the linear schemes to get the exact parabolic velocity distribution for a given width when the channel is parallel to one of lattice velocities. These solutions are derived from the exact steady closure relation, given for the LI($\alpha^{(u)}$) family by the relation (5.11) in [16]:

$$\begin{aligned} &\text{LI: } [\alpha^{(u)}(j_q^\star+\delta_q p_q+\beta^{(p\star)}m_q^{(F)}+\beta^{(f\star)}F_q^\star)+f_q^{\text{p.c.}(u)}](\vec{r}_b)=\alpha^{(u)}j_q^\star(\vec{r}_w),\\ &\beta^{(p\star)}=-\Lambda_o+(\frac{1}{2}+\delta_q-\frac{2}{\alpha^{(u)}}),\quad \beta^{(f\star)}=\Lambda_o. \end{aligned} \tag{2.13}$$

The coefficients $\alpha^{(u)}$, $\beta^{(p\star)}$ and the correction $f_q^{\text{p.c.}(u)}$ are given in Table 2. Dropping the third- and higher-order terms, the Chapman-Enskog expansion of the post-collision components p_q and $m_q^{(F)}$ in Eq. (2.1) is given by Eq. (2.22) in [16]:

$$\begin{aligned} &p_q=\partial_t\Pi_q^\star+\partial_q j_q^\star+\mathcal{O}(\varepsilon^3),\\ &m_q^{(F)}=\partial_t j_q^\star+\partial_q\Pi_q^\star-\Lambda_e\partial_q^2 j_q^\star+\mathcal{O}(\varepsilon^3). \end{aligned} \tag{2.14}$$

Substituting these relations into relation (2.13), and dropping the time derivatives, one gets:

$$\begin{aligned} &[\alpha^{(u)}(j_q^\star+\delta_q\partial_q j_q^\star+\Lambda_{eo}\partial_q^2 j_q^\star-\Lambda_o(\partial_q\Pi_q^\star-F_q^\star))](\vec{r}_b)\\ &\quad+[(\alpha^{(u)}\beta^{(p\star)}+\Lambda_o)m_q^{(F)}+f_q^{\text{p.c.}(u)}](\vec{r}_b)=\alpha^{(u)}j_q^\star(\vec{r}_w)+\mathcal{O}(\varepsilon^3). \end{aligned} \tag{2.15}$$

For a steady linear flow, with constant pressure and no forcing, e.g., a Couette flow, relation (2.15) becomes (with $\delta_q=\frac{1}{2}$ for BB):

$$j_q^\star+\delta_q\partial_q j_q^\star=j_q^\star(\vec{r}_w),\quad m_q^{(F)}=0,\quad \partial_q\Pi_q^\star=0,\quad F_q^\star=0,\quad f_q^{\text{p.c.}(u)}=0. \tag{2.16}$$

The linear schemes maintain therefore the Couette flow in arbitrary inclined channels exactly. For those schemes where

$$[\alpha^{(u)}\beta^{(p\star)}m_q^{(F)}+f_q^{\text{p.c.}(u)}](\vec{r}_b)=-\alpha^{(u)}\Lambda_o m_q^{(F)}(\vec{r}_b), \tag{2.17}$$

the relation (2.15) becomes:

$$[j_q^\star+\delta_q\partial_q j_q^\star+\Lambda_{eo}\partial_q^2 j_q^\star-\Lambda_o(\partial_q\Pi_q^\star-F_q^\star)](\vec{r}_b)=j_q^\star(\vec{r}_w)+\mathcal{O}(\varepsilon^3). \tag{2.18}$$

The BB (with $\delta_q=\frac{1}{2}$), CLI, and MGLI($\alpha^{(u)}$) sub-family yield relations (2.17) and (2.18). Let Θ_q denote the projection of $\vec{c}_q$ on the unit normal to the wall for the cut link q. When the flow is invariant along the wall, then $\partial_q^2 j_q^\star=\Theta_q^2\Delta j_q^\star$ and j_q obeys the projection of the Stokes equation on $\vec{c}_q$:

$$\partial_q\Pi_q^\star-F_q^\star=\frac{\Lambda_e}{3\Theta_q^2}\partial_q^2 j_q^\star. \tag{2.19}$$

With the help of relation (2.19), the closure relation (2.18) becomes:

$$[j_q^\star+\delta_q\partial_q j_q^\star+\frac{3\Theta_q^2-1}{3\Theta_q^2}\Lambda_{eo}\partial_q^2 j_q^\star](\vec{r}_{\rm b})=j_q^\star(\vec{r}_{\rm w})+\mathcal{O}(\varepsilon^3). \tag{2.20}$$

Relation (2.20) represents the third-order accurate Taylor expansion when:

$$\Lambda_{eo}=\frac{3\Theta_q^2\delta_q^2}{2(3\Theta_q^2-1)},\quad 0\le\delta_q\le 1, \tag{2.21}$$

namely,

$$\Lambda_{eo}=\frac{3\delta_q^2}{4},\quad \alpha=0^\circ,\quad \Theta_q\equiv 1,\quad \forall q\in\Pi^{(u)}, \tag{2.22}$$

$$\Lambda_{eo}=\frac{3\delta_q^2}{2},\quad \alpha=45^\circ,\quad \Theta_q=\frac{\sqrt{2}}{2}. \tag{2.23}$$

In the last relation, q addresses the links which are not perpendicular to the wall. It is noted that the location of the wall at grid nodes ($\delta_\perp=0$) lies on the stability limit, $\Lambda_o=0$. When the wall is arbitrary inclined, the solution (2.21) can be unavailable for all non-perpendicular cut links. We show below that the exact solution may exist even for inclined channels but it requires to redefine δ_q for each cut link, depending on Λ_{eo} and the grid resolution.

The solutions (2.22)-(2.23) can be extended for "non-magic" linear schemes (ULI/DLI, YLI, etc.) but they do not satisfy relation (2.17) and the effective values differ then for forcing and pressure driven flow. Exact examples are constructed below for Poiseuille flow.

For transient channel flow, we replace the exact steady closure relation (2.13) with the third-order accurate time-dependent one (see relation (5.3) in [16]):

$$[\alpha^{(u)}(j_q^\star+\delta_q\partial_q j_q^\star+\beta^{(p\star)}m_q^{(F)}+\beta^{(f\star)}F_q^\star+\alpha^{(t)}\partial_t j_q^\star)+f_q^{\text{p.c.}(u)}](\vec{r}_{\rm b})=\alpha^{(u)}j_q^\star(\vec{r}_{\rm w},\widehat{t}), \tag{2.24}$$

where $\alpha^{(t)}$ depends on the multi-reflection coefficients (see Table 10). Generalizing Eq. (2.19) to time-dependent flow, the $m_q^{(F)}$ value (2.14) is equal again to

$$F_q^\star-\frac{3\Theta_q^2-1}{3\Theta_q^2}\Lambda_e\partial_q^2 j_q^\star.$$

The solution (2.21) applies then for transient regime, with a proper choice of time dependent boundary value $j_q^\star(\vec{r}_w,\widehat{t})$. The efficiency of the specific choice (2.22) is checked for time-harmonic, pulsatile flow in Section 4.1.

2.4.1 Poiseuille flow

Let us consider the Poiseuille flow in a channel parallel to the x'-axis, arbitrary rotated with respect to the lattice, and perpendicular to the y'-axis:

$$3(\partial_{x'}P-F_{x'})=\Lambda_e\partial^2_{y'}j_{x'},\quad j_{x'}(\pm\frac{H}{2})=0. \tag{2.25}$$

When the Poiseuille flow is modeled with the Stokes equilibrium ($g_S=0$), the closure relations (2.15) and (2.18) are exact. Let us assume that the Poiseuille profile $j_{x'}(y')$ is established and its *effective width* is $H_{\rm eff}$:

$$4j_{x'}(y')=-\frac{1}{2}\partial^2_{y'}j_{x'}(H^2_{\rm eff}-4y'^2). \tag{2.26}$$

The projections j_q satisfy Eq. (2.19). Let y_q be a "link" coordinate, along any axis parallel to $\{\vec{c}_q,\vec{c}_{\bar{q}}\}$, using $\vec{c}_q$ as unit vector, and the center of the directional segment as the origin:

$$4j_q^\star(y_q)=-\frac{1}{2}\partial^2_q j_q^\star(H^2_{q\rm eff}-4y_q^2),\quad H^2_{q\rm eff}=\frac{H^2_{\rm eff}}{\Theta_q^2}. \tag{2.27}$$

Let the "link" distance from the boundary point $\vec{r}_b$ to the assumed wall point, $y_q=\pm H_q/2$, be r_q, then

$$p_q(\vec{r}_b)=\partial_q j_q^\star(\vec{r}_b)=\frac{1}{2}\partial^2_q j_q^\star(H_q-2r_q),\quad H_q^2=\frac{H^2}{\Theta_q^2}. \tag{2.28}$$

Substituting relations (2.27), (2.28) into relation (2.15), one gets the exact closure relation for each cut link, in term of a difference $H^2_{q\rm eff}-H_q^2$:

$$\begin{aligned}&-\frac{\alpha^{(u)}}{2}\partial^2_q j_q^\star[H^2_{q\rm eff}-(H_q-2r_q)^2-4\delta_q(H_q-2r_q)-\frac{16}{3}\Lambda_{qeo}]\\&+4(\alpha^{(u)}(\beta^{(p\star)}+\Lambda_o)m_q^{(F)}+f_q^{\rm p.c.(u)})=0,\quad \Lambda_{qeo}=\frac{(3\Theta_q^2-1)}{2\Theta_q^2}\Lambda_{eo}.\end{aligned} \tag{2.29}$$

2.4.2 Exact solutions with "magic" linear schemes, CLI and MGLI($\alpha^{(u)}$) sub-family

Owing to relation (2.17), the effective width becomes independent of ∇P and $\vec{F}$ for CLI and the MGLI($\alpha^{(u)}$) sub-family:

$$\text{CLI,MGLI}(\alpha^{(u)}):H^2_{q\rm eff}-H_q^2=4r_q(r_q-2\delta_q)+4H_q(\delta_q-r_q)+\frac{16}{3}\Lambda_{qeo}. \tag{2.30}$$

Solution via Λ_{eo}

When the coefficients of these schemes are computed with $\delta_q = r_q$ (i.e., exactly as for linear flow), the difference between the effective and the assumed solution is:

$$\text{CLI,MGLI}(\alpha^{(u)}): H_{q\,\text{eff}}^2 - H_\delta^2 = -4{\delta_q}^2 + \frac{16}{3}\Lambda_{q\,eo}, \quad \text{if } \delta_q = r_q, \quad 0 \le \delta_q \le 1. \tag{2.31}$$

As expected, $H_{q\,\text{eff}}$ becomes equal to H_q when Λ_{eo} is selected with relation (2.21). This implies however that the value of δ_q satisfies the closure relations for all the cut links. The normal links do not depend on velocity in parallel flow and satisfy the closure relations for any distance δ_q for the parallel channel and for channels inclined by 45° with respect to one of the coordinate axes. For these two orientations, it becomes possible to localize exactly the walls with the help of Λ_{eo}. The "magic" values are then given by relations (2.22) and (2.23), respectively. For the bounce-back, these solutions apply with $\delta_q = \frac{1}{2}$ and reduce to the early obtained results (e.g., Eq. (47) and Eqs. (54) in [9], Eq. (42) in [11]). This solution, originally derived for the FCHC model, is valid for all the cubic velocity sets. The effective width of any parallel channel (e.g., in porous media) is therefore larger than the assumed one:

$$H_{\text{eff}} > H, \quad \text{when } \Lambda_{eo} > \frac{3}{4}.$$

This value represents a reasonable limit for Λ_{eo}. It restricts the highest kinematic viscosity to $\frac{1}{2\sqrt{3}}$ for the BGK model.

Solution via δ_q

In contrast, one can *redefine* δ_q for the coefficients of the linear scheme such that $H_{q\,\text{eff}}^2$ becomes equal to H_q^2 in relation (2.31):

$$\begin{aligned} & r_q^2 - H_q r_q + \delta_q(H_q - 2r_q) + \frac{4}{3}\Lambda_{q\,eo} = 0, \quad \text{then} \\ & \delta_q = r_q + \frac{r_q^2 - \frac{4\Lambda_{q\,eo}}{3}}{H_q - 2r_q}. \end{aligned} \tag{2.32}$$

Again, if solution (2.21) is chosen for Λ_{eo}, then $\delta_q = r_q$. Otherwise, in contrast with the linear flow, δ_q differs from the "physical" distance r_q. It is noted that unlike solution (2.21), solution (2.32) is defined for any inclination. With its help, the linear magic schemes model the Poiseuille flow in arbitrary rotated channel *exactly* and even in the frame of the BGK model. However, the coefficients of the interpolations depend then on the size of the channel, via H_q, and on the Λ_{eo} value. When $\Lambda_{eo} \to 0$, then

$$\delta_q = r_q + \frac{r_q^2}{H_q - 2r_q}.$$

The parameter δ_q lies then in interval $[0,1]$ if

$$0<r_q<1+\frac{H_q}{2}-\sqrt{1+\frac{H_q^2}{4}},\quad H_q>2r_q.$$

One can expect that the stability of solution (2.32) depends on Λ_{eo} and the discretization of the channel.

2.4.3 Exact solutions with "non-magic" schemes, e.g. ULI/DLI and YLI

When $f_q^{\text{p.c.}(u)}=0$ and $\beta^{(p\star)}\neq-\Lambda_o$, e.g., ULI/DLI and YLI, one cannot combine the pressure gradient and forcing terms in closure relation (2.20), and the solution of closure relation (2.29) differs for pressure driven and forcing driven flows, e.g, in a parallel channel ($\Theta_q=1$, $\delta=\delta_q=r_q$):

$$\begin{aligned}
&H_{\text{eff}}^2-H_\delta^2=-4\delta^2-\frac{8\Lambda_e}{3}(3\beta^{(p\star)}+\beta^{(f\star)}), && \text{if } F_q^\star=-\frac{\Lambda_e}{3}\partial_q^2 j_q^\star,\quad \nabla P=0,\\
&H_{\text{eff}}^2-H_\delta^2=-4\delta^2-\frac{16\Lambda_e}{3}\beta^{(p\star)}, && \text{if } \partial_q P_q^\star=\frac{\Lambda_e}{3}\partial_q^2 j_q^\star,\quad \vec{F}=0.
\end{aligned}\tag{2.33}$$

Tables 4 and 5 summarize the solutions (2.30) and (2.33) for the non-inclined channel. They tell us that the effective solutions for "non-magic" schemes approach the "magic" solution (2.22) when $\Lambda_e\to 0$. An extension of the "inclined channel" solution (2.32) is straightforward but δ_q will depend on the viscosity for "non-magic" schemes.

2.5 Dirichlet pressure condition, $M_q^{(p)}$ schemes

They prescribe the pressure distribution $P^b(\vec{r}_{\text{w}},t)$ via the $M_q^{(p)}$-solution for the incoming population:

$$\begin{aligned}
&f_{\bar{q}}(\vec{r}_{\text{b}},t+1)=M_q^{(p)}(\vec{r}_{\text{b}},t),\quad q\in\Pi^{(p)},\quad \vec{r}_{\text{w}}=\vec{r}_{\text{b}}+\delta_q\vec{c}_q,\\
&M_q^{(p)}=R_q(\vec{r}_{\text{b}},t)+f_q^{\text{p.c.}(p)}(\vec{r}_{\text{b}},t)+w_q^{(p)}(\vec{r}_{\text{w}},\widehat{t}),\\
&w_q^{(p)}=-\alpha^{(p)}e_q^+(\vec{r}_{\text{w}},\widehat{t})=-\alpha^{(p)}\Pi_q^\star(c_s^{-2}P^b(\widehat{t}),\rho_0\vec{u}(\vec{r}_{\text{w}},\widehat{t}),\rho_0),\\
&f_q^{\text{p.c.}(p)}=-\beta^{(u)}p_q(\vec{r}_{\text{b}},t),\\
&\alpha^{(p)}=\kappa_1+\kappa_0+\bar{\kappa}_{-1}+\kappa_{-1}+\bar{\kappa}_{-2}-1,\\
&\beta^{(u)}=1-(\kappa_0+2\kappa_{-1}-\bar{\kappa}_{-2})-\alpha^{(p)}(\Lambda_e-\frac{1}{2}).
\end{aligned}\tag{2.34}$$

We recall that p_q is a local component of the TRT collision operator (2.1) and R_q is defined by relation (2.8). In principle, it is sufficient to use linear approximations for the non-

Table 3: The coefficients κ_1, κ_0, κ_{-1}, $\bar{\kappa}_{-1}$, $\bar{\kappa}_{-2}$ for the $M_q^{(p)}$-schemes. The accuracy of PLI and PAB increases to $j^{(3)}/\Pi^{(2)}/F^{(2)}$ with the help of the correction (2.36).

$M_q^{(p)}$	PAB	PLI	PMR(k)
κ_1	-1	$\frac{1}{2}-\delta_q$	$1+\lambda_e$
κ_0	0	δ_q-1	$-1+\frac{3\lambda_e(k-2)+\delta_q k(2+3\lambda_e)}{4}$
κ_{-1}	0	0	$-\frac{k\delta_q}{2}+\lambda_e\frac{1-3\delta_q k}{4}$
$\bar{\kappa}_{-1}$	0	$\frac{1}{2}$	$1+\frac{\delta_q k(\lambda_e-2)+\lambda_e(3k-2)}{4}$
$\bar{\kappa}_{-2}$	0	0	$\frac{-k\delta_q(\lambda_e-2)-\lambda_e(k-2)}{4}$
δ_q	$\frac{1}{2}$	$0\le\delta_q\le 1$	$0\le\delta_q\le 1$
accuracy	$j^{(2)}/\Pi^{(2)}/F^{(2)}$	$j^{(2)}/\Pi^{(2)}/F^{(2)}$	$j^{(3)}/\Pi^{(2)}/F^{(2)}$

linear term in $\Pi_q^\star$, e.g.,

$$\begin{aligned}
&\vec{u}(\vec{r}_{\rm w})\approx\vec{u}(\vec{r}_{\rm b})+\delta_q(\vec{u}(\vec{r}_{\rm b})-\vec{u}(\vec{r}_{\rm b}-\vec{c}_q)), \quad \text{if } \vec{c}_{\bar{q}}\notin\Pi^{(u)}(\vec{r}_{\rm b}), \quad \widehat{t}=t,\\
&\vec{u}(\vec{r}_{\rm w})\approx\vec{u}(\vec{r}_{\rm b})+\frac{\delta_q}{\delta_{\bar{q}}}(\vec{u}(\vec{r}_{\rm b})-\vec{u}(\vec{r}_{\bar{\rm w}})), \qquad \text{if } \vec{c}_{\bar{q}}\in\Pi^{(u)}(\vec{r}_{\rm b}), \quad \delta_{\bar{q}}\neq 0.
\end{aligned} \tag{2.35}$$

When the tangential velocity u_τ is prescribed, one must only approximate the normal velocity component, $u_n(\vec{r}_{\rm w},\widehat{t})$. Table 3 summarizes the principal $M_q^{(p)}$ schemes from [16]: (*pressure anti-bounce-back*) PAB, (*pressure linear interpolation*) PLI and five-populations family PMR(k) with k as free parameter. The $M_q^{(p)}-$ algorithm for each cut link is:

1. Compute the coefficients $\kappa_1-\bar{\kappa}_{-2}$ from Table 3.
2. Approximate the boundary velocity if $g_S=1$, e.g., with the help of relations (2.35).
3. Compute $w_q^{(p)}(\vec{r}_{\rm w},\widehat{t})=-\alpha^{(p)}e_q^+(\vec{r}_{\rm w},\widehat{t})$, $t+\frac{1}{2}\le\widehat{t}\le t+1$.
4. Compute $f_q^{\text{p.c.}(p)}$ with relations (2.34) using the pre-computed value p_q.
5. Compute $M_q^{(p)}(\vec{r}_{\rm b},t)$ with relations (2.34).

Below, we work with the following configuration:

1. The five populations based schemes replace $\kappa_{-1}\tilde{f}_q(\vec{r}_{\rm b}-2\vec{c}_q,t)$ with $\kappa_{-1}f_q(\vec{r}_{\rm b}-\vec{c}_q,t)$ for the *first-type links*. They are switched to PLI (or PAB if $\delta_q=\frac{1}{2}$) for the *second-type links*.
2. PLI/PAB is only applied for the second-type links, with the following correction:

$$\begin{aligned}
&f_q^{\text{p.c.}(p)}\to f_q^{\text{p.c.}(p)}+F_q^{\text{p.c.}-}, \quad F_q^{\text{p.c.}-}=-\gamma^{(u)}\partial_q^{2f.d}j_q^\star,\\
&\text{PAB}:\gamma^{(u)}=\Lambda_e, \quad \text{PLI}:\gamma^{(u)}=\delta_q\Lambda_e.
\end{aligned} \tag{2.36}$$

Relation (2.12) can be used to compute $\partial_q^{2^{f.d}} j_q^\star$.

3. We apply PMR1 = PMR $(k=1)$ and PMR2 = PMR $(k=2(1+\delta_q)^{-2})$, the PMR2 increases the formal precision to a triplet $j^{(3)}/\Pi^{(3)}/F^{(2)}$ but it may results in a loss of the uniqueness of the steady solutions when $\delta_q=0$.

2.6 Mixed $M_q^{(m)}$ scheme

A Dirichlet pressure condition is not sufficient to set the solution of the Navier-Stokes equations uniquely. The mixed scheme [16] prescribes the pressure P^b (as a normal condition) and the tangential velocity $\vec{u}_\tau^b$ (as a tangential condition) at a smooth part $\Gamma^{(p)}$ of the solid boundary. The scheme is based on the projections of $M_q^{(u)}$ and $M_q^{(p)}$ solutions on the local coordinate vectors associated with the wall, $\{\vec{n},\vec{\tau}_1,\vec{\tau}_2\}(\vec{r}_{\rm w})$, with $\vec{n}(\vec{r}_{\rm w})$ for the normal and $\{\vec{\tau}_1,\vec{\tau}_2\}$ for the tangential vectors, then $\vec{c}_q=\{c_{qn},c_{q\tau_1},c_{q\tau_2}\}$. Assuming that both $M_q^{(p)}(\vec{r}_{\rm b})$ and $M_q^{(u)}(\vec{r}_{\rm b})$ values are computed for cut links, the mixed scheme adds a correction $\delta f_{\bar{q}}$ to $M_q^{(p)}$:

$$f_{\bar{q}}(\vec{r}_{\rm b},t+1)=M_q^{(m)}(\vec{r}_{\rm b},t),\quad M_q^{(m)}(\vec{r}_{\rm b},t)=M_q^{(p)}(\vec{r}_{\rm b},t)+\delta f_{\bar{q}}(\vec{r}_{\rm b},t),\quad q\in\Pi^{(p)}. \tag{2.37}$$

The local system of normal/tangential constraints is presented in [16] with respect to $\{\delta f_{\bar{q}}(\vec{r}_{\rm b},t)\}$. The solution represents a linear combination of δM_q values:

$$\delta M_q=M_q^{(u)}-M_q^{(p)},\quad q\in\Pi^{(p)}. \tag{2.38}$$

When the solid wall *is perpendicular to one of the coordinate axis*, they can be computed with relations (2.39)-(2.41). The $M_q^{(m)}$-algorithm for the set of cut links, $\{q\}\in\Pi^{(p)}$, consists from the following steps:

1. Prescribe the set of the boundary values for the tangential velocity, $\{u_\tau^b(\vec{r}_{\rm w},\widehat{t})\}$, and pressure $\{P^b(\vec{r}_{\rm w},\widehat{t})\}$, $\{\vec{r}_{\rm w}\}=\{\vec{r}_{\rm b}+\delta_q\vec{c}_q\}$, $q\in\Pi^{(p)}$.
2. Approximate the normal velocity $\{u_n(\vec{r}_{\rm w},\widehat{t})\}$, e.g., with relations (2.35).
3. Compute $\{M_q^{(p)}(\vec{r}_{\rm b})\}$ for all $q\in\Pi^{(p)}$.
4. Compute $\{M_q^{(u)}(\vec{r}_{\rm b})\}$ for all $q\in\Pi^{(p)}$.
5. Compute $f_{\bar{q}}(\vec{r}_{\rm b},t+1)=M_q^{(m)}(\vec{r}_{\rm b})$ in a form (2.37), e.g., with relations (2.39)-(2.41) for $\{\delta f_{\bar{q}}(\vec{r}_{\rm b},t)\}$.

Unless specially indicated, we do not apply $M_q^{(m)}$ in corners. When two anti-parallel velocities prescribe there two different conditions (in this paper, the mixed condition on the vertical boundary and the velocity on the horizontal boundary), the velocities $\{\vec{c}_q\}$ which cut only the vertical boundary use $M_q^{(p)}$ (the pressure condition only, $\delta f_{\bar{q}}(\vec{r}_{\rm b},t)=0$)

and the velocities $\{\vec{c}_q\}$ which cut the horizontal boundary use $M_q^{(u)}$ (including the link going through the corner). As an alternative technique, we use the $M_q^{(m)}$ scheme for all populations which cut the vertical boundary, including the population which goes through the corner, and $M_q^{(u)}$ for the other cut links.

2.6.1 $d2Q9$ velocity set

For the standard node with two incoming diagonal populations and the normal one, the solution is:

$$\text{d2Q9:}\ \ \delta f_{\bar{q}} = -\frac{c_{\bar{q}\tau_1}}{2}\sum_{q\in\Pi^{(p)}} \delta M_q c_{q\tau_1}\,. \tag{2.39}$$

It is noted that the normal link ($c_{\bar{q}\tau_1}=0$) imposes the pressure condition:

$$\delta f_{\bar{q}} = 0, \quad M_q^{(m)} = M_q^{(p)}.$$

2.6.2 $d3Q15$ velocity set

The solution for the 5 incoming populations in a standard boundary node is:

$$\text{d3Q15:}\ \ \delta f_{\bar{q}} = -\frac{c_{\bar{q}\tau_1}}{4}\sum_{q\in\Pi^{(p)}} \delta M_q c_{q\tau_1} - \frac{c_{\bar{q}\tau_2}}{4}\sum_{q\in\Pi^{(p)}} \delta M_q c_{q\tau_2}. \tag{2.40}$$

Again, the normal population ($c_{q\tau_1}=c_{\bar{q}\tau_2}=0$) performs a pressure condition, $\delta f_{\bar{q}}=0$.

2.6.3 $d3Q19$ velocity set

The solution in a standard node has the form:

$$\begin{aligned}
\text{d3Q19:}\qquad & \delta f_{\bar{q}} = -\frac{c_{\bar{q}\tau_1}}{2}\sum_{q\in\Pi^{(p)}} \delta M_q c_{q\tau_1}, \quad c_{qn}c_{q\tau_1}\neq 0,\\
& \delta f_{\bar{q}} = -\frac{c_{\bar{q}\tau_2}}{2}\sum_{q\in\Pi^{(p)}} \delta M_q c_{q\tau_2}, \quad c_{qn}c_{q\tau_2}\neq 0,\\
& \delta f_{\bar{q}} = 0, \quad c_{qn}\neq 0, \quad c_{q\tau_1}=0, \quad c_{q\tau_2}=0.
\end{aligned} \tag{2.41}$$

2.7 "Constant mass flux" condition

The previous solutions are designed for the velocity, pressure and mixed conditions on arbitrarily shaped boundaries. In practice, one often needs to guarantee a constant mass flux at the inlet/outlet. The condition called "constant pressure" is suggested for this purpose in [24] (unfortunately, with an erratum). Let us consider this scheme in more detail.

We assume that the x axis is perpendicular to $\Gamma^{(p)}$ and propose to derive a solution for the incoming population $f_{\bar{q}}(\vec{r}_b,t+1)$ from the following relation:

$$\tilde{f}_q(\vec{r}_b,t)-f_{\bar{q}}(\vec{r}_b,t+1)=\tilde{f}_q(\vec{r}_b-\vec{c}_{qx},t)-f_{\bar{q}}(\vec{r}_b-\vec{c}_{qx},t+1),\quad q\in\Pi^{(p)}. \tag{2.42}$$

Updating $f_{\bar{q}}(\vec{r}_b-\vec{c}_{qx},t+1)$ prior to $f_{\bar{q}}(\vec{r}_b,t+1)$, the boundary rule becomes:

$$f_{\bar{q}}(\vec{r}_b,t+1)=f_{\bar{q}}(\vec{r}_b-\vec{c}_{qx},t+1)+[\tilde{f}_q(\vec{r}_b,t)-\tilde{f}_q(\vec{r}_b-\vec{c}_{qx},t)],\quad q\in\Pi^{(p)}. \tag{2.43}$$

The conditions (2.42),(2.43) are exact for flows invariant along the x-axis, driven by forcing or a constant pressure gradient. Let us assume that the populations $\tilde{f}_q$, $q\in\{q_\perp\}$ stay inside the boundary column after propagation, such that the following relation holds:

$$\sum_{\vec{r}_b}\sum_{q\in\{q_\perp\}}\tilde{f}_q(\vec{r}_b,t)=\sum_{\vec{r}_b}\sum_{q\in\{q_\perp\}}f_{\bar{q}}(\vec{r}_b,t+1). \tag{2.44}$$

This condition includes the mass conserving boundary solutions for the vertical populations and, e.g., the bounce-back condition for the populations incoming through the corners. Assuming than that all other inside populations are obtained either with the condition (2.43) or via a propagation from the next fluid column, let us compute the mass inside the boundary column:

$$\begin{aligned}
&\sum_{\vec{r}_b}\sum_{q=0}^{Q-1}f_q(\vec{r}_b,t+1)\\
&=\sum_{\vec{r}_b}\sum_{q\in\Pi^{(p)}}[f_{\bar{q}}(\vec{r}_b,t+1)+\tilde{f}_q(\vec{r}_b-\vec{c}_{qx},t)]+\sum_{\vec{r}_b}\sum_{q\in\{q_\perp\}}\tilde{f}_q(\vec{r}_b,t)\\
&=\sum_{\vec{r}_b}\sum_{q\in\Pi^{(p)}}[\tilde{f}_q(\vec{r}_b,t)+f_{\bar{q}}(\vec{r}_b-\vec{c}_{qx},t+1)]+\sum_{\vec{r}_b}\sum_{q\in\{q_\perp\}}\tilde{f}_q(\vec{r}_b,t)\\
&=\sum_{\vec{r}_b}\sum_{q\in\Pi^{(p)}}[\tilde{f}_q(\vec{r}_b,t)+\tilde{f}_{\bar{q}}(\vec{r}_b,t)]+\sum_{\vec{r}_b}\sum_{q\in\{q_\perp\}}\tilde{f}_q(\vec{r}_b,t)\\
&=\sum_{\vec{r}_b}\sum_{q=0}^{Q-1}\tilde{f}_q(\vec{r}_b,t)=\sum_{\vec{r}_b}\sum_{q=0}^{Q-1}f_q(\vec{r}_b,t).
\end{aligned} \tag{2.45}$$

The total initial mass at a given inlet/outlet vertical column is kept at a constant value when the conditions mentioned above are satisfied. In channels, one can prescribe then the total mass (pressure) at inlet/outlet sections. When the pressure does not vary across the channel, e.g., for the Poiseuille flow, one prescribes then the inlet/outlet pressure values exactly.

3 Steady solutions

The multi-reflection approach is validated for smooth non-rectangular boundaries in [11, 16,32]. The MR1, MGMR(C) and MLI($\alpha^{(u)}$) demonstrate a very high accuracy for permeability computations. Our purpose here is to check all the developed schemes and their

combinations, with a focus on their exactness for particular flows, competitive accuracy and uniqueness of their steady solutions. We restrict ourselves to rectangular boxes but use, at least, two kinds of boundary conditions. The first setup prescribes the Dirichlet velocity using $M_q^{(u)}$ schemes for all cut links in the system. The second setup combines $M_q^{(u)}$ at the horizontal walls with the $M_q^{(m)}$ at the inlet/outlet. The distances $\delta_q^{(h)}/\delta_q^{(v)}$ to the horizontal/vertical boundaries are prescribed arbitrarily between 0 and 1. When suitable, the solutions are also computed with periodic or constant mass flux boundary conditions (2.42). The time dependent Womersley flow is studied along the same lines in the next section.

All computations are performed with the $d3Q15$ velocity set, $c_s^2=\frac{1}{3}$ and momentum conserving equilibrium:

$$\vec{j}^{\rm eq}=\vec{J},\quad \vec{\mathcal{F}}=\vec{F}.$$

The $L^2(\phi)$-error with respect to an exact solution ϕ^{ex} is measured for all grid points:

$$L^2(\phi)=\sqrt{\frac{\sum_{\vec{r}}(\phi(\vec{r})-\phi^{ex}(\vec{r}))^2}{\sum_{\vec{r}}(\phi^{ex}(\vec{r}))^2}}. \tag{3.1}$$

3.1 Test I: Poiseuille flow with the Stokes equilibrium, $g_S=0$

Non-equilibrium steady bulk solution $n_q^{\pm}$ is given as an infinite Chapman-Enskog series by relations (3.1) in [16]. Dropping the third and higher orders, it becomes for the Stokes equilibrium ($\Pi=P$):

$$\begin{aligned} n_q^+&=n_q^{+(S)}=\frac{\partial_q j_q^\star(\vec{r})}{\lambda_e},\\ n_q^-&=n_q^{-(S)}=\frac{\partial_q P_q^\star-\Lambda_e\partial_q^2 j_q^\star-S_q^-}{\lambda_o},\quad P_q^\star=t_q^\star P. \end{aligned} \tag{3.2}$$

These relations, for any linear combination of the constant pressure gradient and uniform external forcing (i.e., for any choice of $\vec{\mathcal{F}}$), describe the exact solution when $\vec{j}$ obeys the Stokes equation (2.25) describing a Poiseuille flow.

When the parabolic pressure and/or velocity schemes are applied for all the incoming populations, the numerical solution will have the form (3.2) without any approximation. This is verified for parallel and rotated periodic channels in [8–11] using different, third-order accurate, no-slip boundary schemes. Solution (2.32) allows to obtain the Poiseuille flow for any inclination using linear "magic" schemes. We restrict the numerical simulations below to non-inclined channels but using several inlet/outlet boundary conditions. Special attention will be paid to closed (rectangular) corners and the location of flat walls at grid nodes.

Table 4: Test I. Exact solutions for $H^2_{\rm eff}-H^2_\delta$, the difference between the effective and the assumed squared diameters for *non-inclined* Poiseuille flow driven by $\vec{F}$ and/or ∇P.

$M_q^{(u)}$	$H^2_{\rm eff}-H^2_\delta$	$\nabla P, \vec{F}$	$\delta=\delta_q$
BB	$\frac{16}{3}\Lambda_{eo}-1$	$\forall\nabla P, \forall\vec{F}$	$\frac{1}{2}$
CLI, MGLI($\alpha^{(u)}$)	$\frac{16}{3}\Lambda_{eo}-4\delta^2$	$\forall\nabla P, \forall\vec{F}$	$0\le\delta\le1$
ULI/DLI	$\frac{16}{3}\Lambda_{eo}-4\delta^2+4\Lambda_e\lvert1-2\delta\rvert$	$\nabla P=0$	$0\le\delta\le1$
ULI/DLI	$\frac{16}{3}\Lambda_{eo}-4\delta^2+\frac{8}{3}\Lambda_e\lvert1-2\delta\rvert$	$\vec{F}=0$	$0\le\delta\le1$
YLI	$\frac{16}{3}\Lambda_{eo}-4\delta^2+4\Lambda_e$	$\nabla P=0$	$0\le\delta\le1$
YLI	$\frac{16}{3}\Lambda_{eo}-4\delta^2+\frac{8}{3}\Lambda_e$	$\vec{F}=0$	$0\le\delta\le1$
MR(k), MLI($\alpha^{(u)}$)	0	$\forall\nabla P, \forall\vec{F}$	$0\le\delta\le1$

3.1.1 Open channel

Periodic conditions at the inlet/outlet are applied when the flow is driven by a force. The constant mass flux condition (2.42) is suitable for any combination of the constant pressure gradient and forcing. Inlet/outlet pressure values can be prescribed then via the initial distribution provided that the no-slip conditions on the horizontal walls keep the mass inside the inlet/outlet columns, e.g., owing to symmetry.

The parabolic schemes, the MLI($\alpha^{(u)}$) and MR(k) families, maintain the population solution (3.2) *exactly* and localize the horizontal walls at the prescribed distance, $0\le\delta_q\le1$, for any values of the relaxation parameters.

When $\delta_q^{(h)}=0$, then MULI = MYLI, MCLI = MR1 and, in Section 5.5 of [16], it is predicted that $n^-_{q_\perp}(\vec{r}_{\rm b},t)$ is conserved for the normal link $q_\perp$, i.e.,

$$n^-_{q_\perp}(\vec{r}_{\rm b},t)\equiv n^-_{q_\perp}(\vec{r}_{\rm b},0)\ \forall t.$$

Initializing arbitrary distribution $n^-_{q_\perp}(\vec{r}_{\rm b},0)$, we confirm that it is conserved on the obtained solution. A discrepancy between the exact solution,

$$n^-_{q_\perp}(\vec{r}_{\rm b},t)=0,$$

and the conserved initial value causes the development of accommodation solutions. When $n^-_{q_\perp}(\vec{r}_{\rm b},0)$ is distributed uniformly along the top and bottom walls (even when the two values differ for the two boundaries), the accommodation has no impact on the obtained velocity (which remains exact). This type solutions are constructed in Section 3.2.2. However, the accommodation resulting from the non-uniform distributions modifies the velocity solution, which therefore loses its uniqueness.

The linear schemes, BB and LI($\alpha^{(u)}$), obey the exact steady closure relation (2.13). Their effective solutions are derived in Section 2.4.1 and summarized in Table 4 for a parallel channel. With the help of the solutions from Table 5, the "magic" linear schemes (CLI and MGLI($\alpha^{(u)}$)) localize the walls exactly, without any "boundary layers". Alternatively, this

Table 5: Test I. Special solutions for Λ_{eo}. They yield $H_{\text{eff}}=H_\delta$, making non-inclined Poiseuille flows modeled exactly.

$M_q^{(u)}$	$\Lambda_{eo}>0$	$\nabla P, \vec{F}$	$\delta=\delta_q$
BB	$\Lambda_{eo}=\frac{3}{16}$	$\forall\nabla P, \forall\vec{F}$	$\frac{1}{2}$
CLI,MGLI($\alpha^{(u)}$)	$\Lambda_{eo}=\frac{3\delta^2}{4}$	$\forall\nabla P, \forall\vec{F}$	$0<\delta\leq 1$
ULI/DLI	$\Lambda_{eo}=\frac{3}{4}(\delta^2-\Lambda_e\lvert 1-2\delta\rvert)$	$\nabla P=0$	$\Lambda_e<\frac{\delta^2}{\lvert 1-2\delta\rvert}$
ULI/DLI	$\Lambda_{eo}=\frac{3}{4}\delta^2-\frac{\Lambda_e}{2}\lvert 1-2\delta\rvert$	$\vec{F}=0$	$\Lambda_e<\frac{3}{2}\frac{\delta^2}{\lvert 1-2\delta\rvert}$
YLI	$\Lambda_{eo}=\frac{3}{4}(\delta^2-\Lambda_e)$	$\nabla P=0$	$\Lambda_e<\delta^2$
YLI	$\Lambda_{eo}=\frac{3}{4}\delta^2-\frac{\Lambda_e}{2}$	$\vec{F}=0$	$\Lambda_e<\frac{3}{2}\delta^2$
MR(k), MLI($\alpha^{(u)}$)	$\forall\Lambda_{eo}$	$\forall\nabla P, \forall\vec{F}$	$0\leq\delta\leq 1$

is achieved when δ_q is redefined following solution (2.32), with $\Theta_q\equiv 1$ for non-inclined channel.

The staggered invariants. In open channel, the oscillating vertical velocity, $u_y^s(y,t)=-u_y^s(y,t+1)$ is maintained with the BB, CLI, MR1 and, when $\delta_q^{(h)}=0$, with MCLI. It can be provoked, in addition to a developed Poiseuille solution, when the staggered invariants (see [16], Eq. (5.32)) of these schemes are initialized. We only recall here that initializing the uniform vertical velocity $u_y=u^0$ in a box consisting from L_y horizontal lines, one gets the oscillating amplitude:

$$|u^s|=\frac{(1+\kappa_0+\kappa_{-1})|u^0|}{L_y-(L_y-2)\kappa_0+(L_y-4)\kappa_{-1}},$$

when L_y is odd (Eq. (5.34) in [16]). It is noted that the uniform initial vertical velocity is damped when L_y is even.

3.1.2 Dirichlet velocity conditions

Two exact parabolic profiles at the inlet and outlet are prescribed with $M_q^{(u)}$. The profiles may correspond to any selected combination of the modeled forcing and the assumed constant pressure gradient ∇P. We emphasize that the pressure solution is defined up to a constant. When the boundary schemes allow a mass flux across the wall, the obtained density (pressure) distribution can happen to be non-stationary although the velocity field results in a steady distribution.

Parabolic schemes, MLI($\alpha^{(u)}$) and MR(k). Applied to all boundaries, they maintain the *exact Poiseuille profile* for any distances $\delta_q^{(h)}$ and $\delta_q^{(v)}$. When $\delta_q\neq 0$, the steady solution is unique for any initial distribution.

When $\delta_q^{(h)}=0$ and/or $\delta_q^{(v)}=0$, then $n_{q_\perp}^-(t)$ is conserved for all cut links perpendicular to solid walls in standard boundary nodes. The velocity solution generally depends on the initialization of these links. One can check for this taking, e.g., $n_{q_\perp}^-(\vec{r}_{\text{b}},t=0)=0$ for the

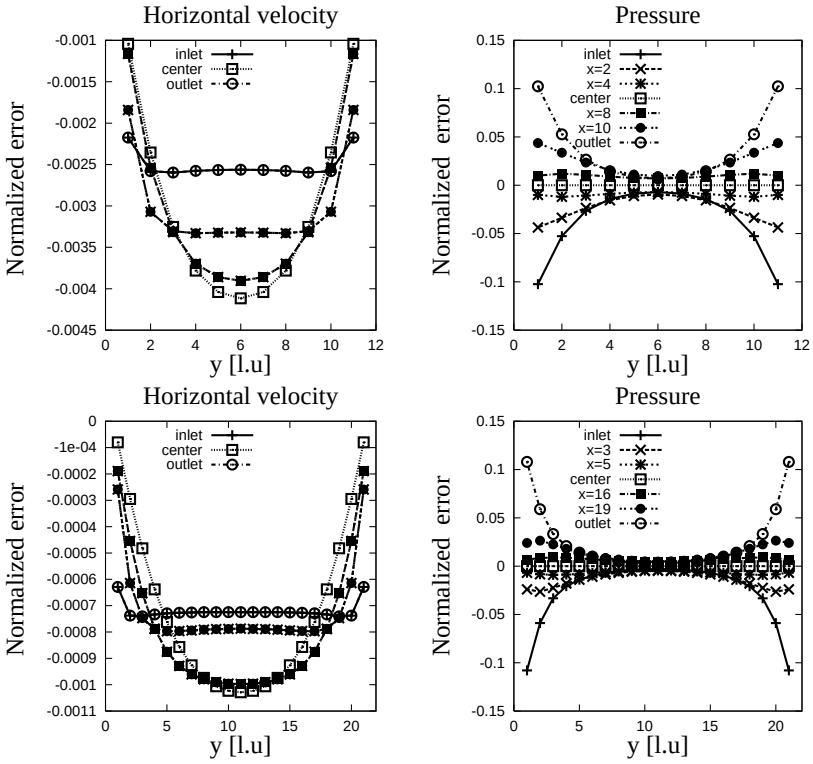

Figure 1: Test I, $\delta_q^{(h)}=\delta_q^{(v)}=\frac{1}{2}$, $\Lambda_{eo}=\frac{3}{16}$. The Dirichlet velocity conditions are modeled with the bounce-back for all links. The closure relation is exact excepted for inlet/outlet horizontal links. The computations are performed in a $L^2=11^2$ box (top) and a $L^2=21^2$ box (bottom). The velocity error is normalized with its highest value: $\frac{u_x(x,y)-u_x^{ex}(y)}{u_x^{max}}$, $u_x^{max}=\frac{(F_x-\nabla_x P)}{8\nu}L^2$. The normalized pressure error is computed as $\frac{P(x,y)-P^{ex}(x)}{|\nabla_x P-F_x)|}$. The solution becomes exact using the correction (3.3) for the incoming horizontal links.

horizontal populations when $\delta_q^{(v)}=0$. The obtained solution differs from the exact one which is get, e.g., starting from the exact solution (3.2) for the horizontal boundary links. Similar, taking a non-zero distribution $n_{q_\perp}^-(\vec{r}_b,t=0)$ for the vertical links when $\delta_q^{(h)}=0$, the velocity solution will differ from the one obtained starting from the exact solution, $n_{q_\perp}^-\equiv 0$. Switching then to LI($\alpha^{(u)}$)-family for the vertical links restores the uniqueness and maintains the exact solution. We recommend to replace the parabolic schemes with MGULI when $\delta_q=0$, or to avoid this discretization, e.g., replacing $\delta_q=0$ with $\delta_q=1$.

Linear schemes: BB and LI($\alpha^{(u)}$). When Λ_o is chosen as indicated in Table 5, the closure relations are exact for the horizontal walls and, due to the vanishing vertical velocity, for the *diagonal links* at the inlet/outlet. The error estimations for Stokes flow are independent of the selected viscosity value provided that the solution $\nu\vec{j}(\vec{r})$ is fixed by Λ_{eo}, i.e., for BB, CLI and MGLI($\alpha^{(u)}$) sub-family. Fig. 1 shows the normalized errors caused by the inexactness of the closure relation for *incoming horizontal populations*. The computa-

tions are performed with a mixture, half forcing and half pressure gradient, using equal forcing for coarse and fine grids (here, $\nabla_x P=-F_x=-10^{-3}$). The pressure distribution is centered around its solution at the center of the box. The picture shows that although the highest pressure error is localized in the inlet/outlet corners, the normalized velocity error reaches the highest value in the middle of the channel. The velocity error decreases as h^2 ($L^2(u_x)\approx 0.4\%$ on the coarse grid and $L^2(u_x)\approx 0.1\%$ on the fine one) but the highest amplitude of the normalized pressure error remains constant.

With the help of the exact closure relation (2.13), one can built the local correction for the *horizontal links* (where $\partial_q^2 j_q^\star=0$, $p_q=0$):

$$f_q^{\text{p.c.}(u)}=-\alpha^{(u)}(\beta^{(p\star)}m_q^{(F)}+\Lambda_o F_q^\star),\quad \text{if } c_{qy}=0,\quad c_{qz}=0. \tag{3.3}$$

For BB and CLI,

$$\beta^{(p\star)}=-\beta^{(f\star)}=-\Lambda_o,$$

then

$$f_q^{\text{p.c.}(u)}=\alpha^{(u)}\Lambda_o m_q\quad \text{if } S_q^-=F_q^\star.$$

The correction (3.3) replaces, for the *horizontal links only*, the correction from Table 2. With its help, *the velocity solution becomes exact using effective Λ_{eo} solutions obtained for an open channel*. We suggest that the correction (3.3) may also become useful in more general channel-type inlet/outlet flows.

When $\delta_q=\delta_{\bar{q}}=0$, then $f_{\bar{q}}(\vec{r}_{\text{b}},t+1)=f_q(\vec{r}_{\text{b}},t)$ and vice versa for *the second type link* using the ULI scheme in the local form (2.10). Since this solution is independent of the evolution of the system, the steady solution depends on the initial distribution. We find that the MGULI scheme leads to a unique steady solution in this case, owing to its $f_q^{\text{p.c.}(u)}$ correction. The steady solutions coincide for all magic schemes of the MGLI($\alpha^{(u)}$) sub-family but the CLI scheme supports the staggered invariants (see in [16]) and it is less stable than MGULI for $\delta_q\to 0$. If the staggered invariant is present initially in the system, the CLI solutions may oscillate in time even when all distances δ_q are different from zero and MGULI/MGDLI is applied in corners. In this test one can trigger the two-dimensional oscillating solution for all variables, initializing a uniform vertical velocity. The combination of MGULI/MGDLI (for the vertical or horizontal boundaries and corners) with CLI (for two other opposite walls) usually works most robust and suppresses the staggered oscillations.

3.1.3 Mixed boundary condition

The $M_q^{(m)}$ scheme prescribes the pressure values (here, $P(x=0)=c_s^2\rho_0$ and $P(x=L)=c_s^2\rho_0+\nabla_x PL$) and $u_y=0$ at the inlet/outlet. The pressure family PMR(k) is *exact* for Poiseuille flow based on the Stokes equilibrium and with/without forcing: PMR1 and PMR2 are applied in this test. Applied to one population in the corner (the second-type link which cuts the vertical boundary), the PLI scheme becomes exact for the parabolic flow with the

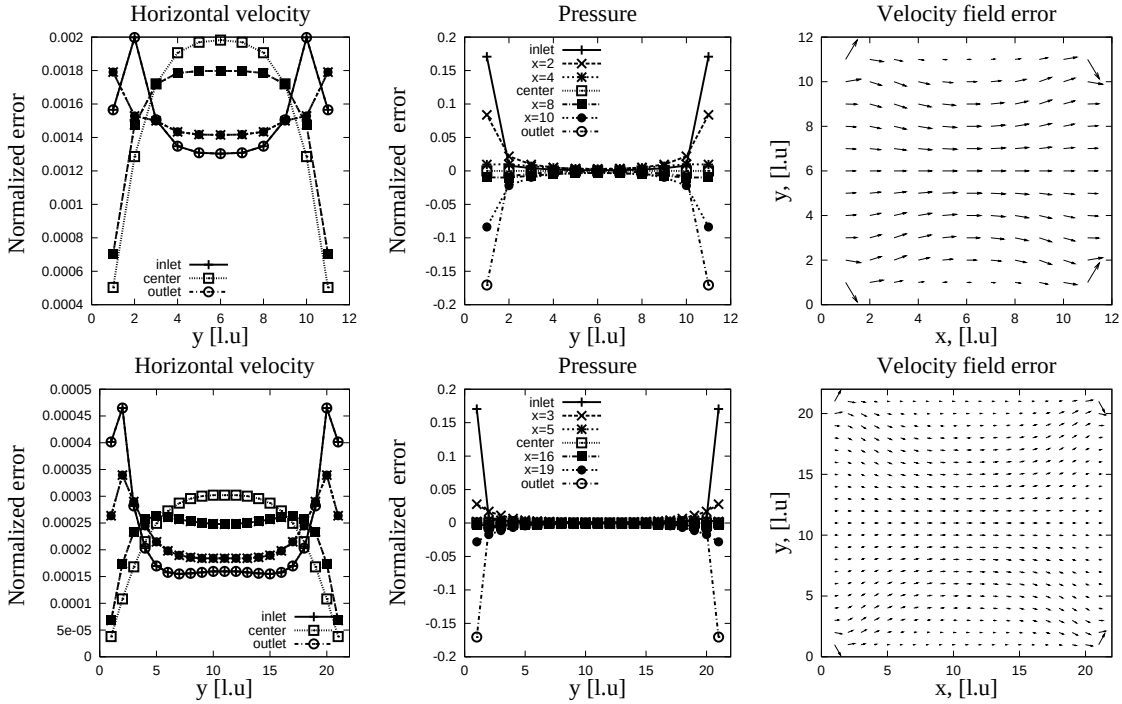

Figure 2: Test I is modeled with the exact BB at the horizontal boundaries and the mixed condition on the vertical boundaries, $\delta_q^{(h)}=\delta_q^{(v)}=\frac{1}{2}$, $\Lambda_{eo}=\frac{3}{16}$. Top row: $L^2=11^2$, $L^2(u_x)=2.1\times10^{-1}\%$. Bottom row: $L^2=21^2$, $L^2(u_x)=3\times10^{-2}\%$. The second-order correction (2.36) is specially omitted for one (pressure) population in corners, resulting in the loss of the exact solution.

help of correction (2.36). The parabolic schemes but also LI−schemes, applied as the $M_q^{(u)}$ component of $M_q^{(m)}$, maintain the *exact* Poiseuille solution for any distance to inlet/outlet. In fact, the terms related to second gradients vanish here from the normal (pressure) closure relation and the linear velocity schemes are sufficient for $M_q^{(m)}$. Moreover, owing to the invariance of the vertical velocity, $u_y=u_\tau^b\equiv0$, the *(modified bounce-back)* MBB scheme yields exact mixed condition for Poiseuille flow at any distance to inlet/outlet:

$$\text{MBB:}\quad M_q^{(u)}=\tilde{f}_q-p_q-2t_q^\star\sum_\tau u_\tau^b c_{q\tau}\,,\ q\in\Pi^{(p)}. \tag{3.4}$$

When the correction (2.36) is omitted, PLI does not work exactly, except for $\delta_q^{(v)}=0$. Fig. 2 shows that the resulting pressure and velocity field errors are mostly concentrated in the corners. The velocity error decreases very rapidly with refining, owing to the exactness of the velocity closure relations for all other links. However, the normalized pressure peak in corners (using the same forcing for fine/coarse grids) again does not reduce. This test confirms the necessity of highly accurate pressure schemes in corners.

When $\delta_q^{(h)}=0$, the same conclusion follows for the parabolic schemes as above: the so-

lution losses the uniqueness, depending on the initial distribution $n^-_{q_\perp}(\vec{r}_{\rm b},t=0)$ prescribed for the vertical links. In contrast, when $\delta^{(v)}_q=0$, the PMR1 constrains the boundary solution for the horizontal links and the solution remains unique, even applying the parabolic schemes as $M^{(u)}_q$ component of the mixed condition. Also, the mixed condition does not maintain the oscillating (two-dimensional) vertical velocity except for $\delta^{(h)}_q=0$, when CLI or MR1 are applied on the horizontal boundaries. However, the PMR2 component of the PMR(k) family results in non-unique solutions when $\delta^{(v)}_q=0$ because of the exactness of its closure relation for this location, similar like the parabolic velocity schemes (see in [16]). We recommend therefore to use PMR1 when $\delta^{(v)}_q=0$.

3.2 Test II: Poiseuille flow with the Navier-Stokes equilibrium, $g_S=1$

3.2.1 Following Chapman-Enskog method

The Chapman-Enskog steady expansion, here $\{p^{ch}_q,m^{ch}_q\}$, can be decomposed into two parts: the Stokes component $\{\lambda_e n^{+(S)}_q,\lambda_o n^{-(S)}_q\}$, given with the relation (3.2), plus the expansion $\{\delta p^{(ch)}_q,\delta m^{(ch)}_q\}$ due to the non-linear equilibrium term $t^\star_q E^+_q(\vec{j},\rho_0)$. In a non-inclined channel,

$$E^+_q(y)=\rho_0 u^2_x(y)\frac{(3c^2_{qx}-1)}{2},\quad u_x(y)=\frac{j_x(y)}{\rho_0}.$$

The exact solution becomes (it is given by the $p^{(2)}_q+p^{(4)}_q$ and $m^{(1)}_q+m^{(3)}_q$ terms of the steady Chapman-Enskog solution, Eq. (3.1) in [16]):

$$\begin{aligned}&p^{ch}_q=\lambda_e n^{+(S)}_q+\delta p^{(ch)}_q,\quad m^{ch}_q=\lambda_o n^{-(S)}_q+\delta m^{(ch)}_q,\\&\delta p^{(ch)}_q=\rho_0 T_q H^+(y)c^2_{qy},\quad \delta m^{(ch)}_q=\rho_0 T_q H^-(y)c_{qy},\quad T_q=t^\star_q(3c^2_{qx}-1),\end{aligned}\tag{3.5}$$

where

$$\begin{aligned}&H^-(y)=H^{-(1)}(y)+H^{-(3)}(y),\quad H^+(y)=H^{+(2)}(y)+H^{+(4)}(y),\\&H^{-(1)}=u_x\partial_y u_x,\\&H^{+(2)}=-\Lambda_o(u_x\partial^2_y u_x+(\partial_y u_x)^2),\\&H^{-(3)}=3(\Lambda_{eo}-\frac{1}{12})(\partial_y u_x\partial^2_y u_x),\\&H^{+(4)}=-3\Lambda_o(\Lambda_{eo}-\frac{1}{6})(\partial^2_y u_x)^2,\quad y=0,1,\cdots,L_y-1.\end{aligned}\tag{3.6}$$

The exact no-slip scheme for the solution (3.5)-(3.6) must fit $\mathcal{O}(\partial^4_y u^2_x)$. However, although no $M^{(u)}_q$ scheme possesses such an accuracy, the macroscopic solution remains the same as with the Stokes equilibrium in an open channel for all $M^{(u)}_q$ schemes. A reason is

that a Knudsen layer population correction "compensates" $\{\delta p_q^{(ch)},\delta m_q^{(ch)}\}$ in the closure relations.

3.2.2 Knudsen layer solution

The Chapman-Enskog expansion assumes that the solution for all populations is obtained via the evolution equation. At the boundary points, the microscopic boundary schemes close the system for the incoming populations. The exact population solution can differ then from the solution obtained via the Chapman-Enskog expansion. Let us decompose then the effective solution $\{p_q,m_q\}$ into two parts: Chapman-Enskog solution $\{p_q^{ch},m_q^{ch}\}$ and an additional solution $g_q^{\pm}(\vec{r})$, hereafter referred to as *Knudsen layer*:

$$p_q = p_q^{ch} + g_q^+, \quad m_q = m_q^{ch} + g_q^-. \tag{3.7}$$

The exact recurrence equations of the TRT operator are given in [16] by relations (3.2). They remain valid if $g_q^{\pm}(\vec{r})$ obeys the following equations for non-incoming populations:

$$\begin{aligned} &g_q^+ = (\Lambda_{eo} - \frac{1}{4})\Delta_q^2 g_q^+, \quad g_q^- = (\Lambda_{eo} - \frac{1}{4})\Delta_q^2 g_q^-, \\ &\sum_{q=0}^{Q-1} g_q^+ = 0, \quad \sum_{q=1}^{Q-1} g_q^- \vec{c}_q = 0, \end{aligned} \tag{3.8}$$

and

$$\Lambda_e \Delta_q^2 g_q^+ = -\bar{\Delta}_q g_q^-, \quad \Lambda_o \Delta_q^2 g_q^- = -\bar{\Delta}_q g_q^+, \tag{3.9}$$

where

$$\begin{aligned} &\bar{\Delta}_q \phi(\vec{r}) = \frac{1}{2}(\phi(\vec{r}+\vec{c}_q) - \phi(\vec{r}-\vec{c}_q)), \\ &\Delta_q^2 \phi(\vec{r}) = \phi(\vec{r}+\vec{c}_q) - 2\phi(\vec{r}) + \phi(\vec{r}-\vec{c}_q), \quad \forall \phi. \end{aligned} \tag{3.10}$$

Remarkable is that when $\Lambda_{eo} = 1/4$, the Knudsen layers $\{g_q^{\pm}\}$ should vanish, except for the boundary points. We present now a particular Knudsen layer solution to Eqs. (3.8)-(3.10):

$$g_q^+ = \rho_0 T_q K^+(y) c_{qy}^2, \quad g_q^- = \rho_0 T_q K^-(y) c_{qy}, \quad y = 0,1,\cdots,L_y - 1. \tag{3.11}$$

It has no impact neither on the mass nor on the momentum. The general form of the solution $K^{\pm}(y)$ is:

$$K^{\pm}(y) = k_1^{\pm} r_0^y + k_2^{\pm} r_0^{-y}, \quad r_0 = \frac{2\sqrt{\Lambda_{eo}}+1}{2\sqrt{\Lambda_{eo}}-1}, \quad \Lambda_{eo} \neq \frac{1}{4}, \quad \Lambda_{eo} \neq 0, \tag{3.12}$$

$$\begin{aligned} &K^{\pm}(0) = k_1^{\pm}, \quad K^{\pm}(L_y-1) = k_2^{\pm}, \quad K^{\pm}(y) = 0, \quad 0 < y < L_y - 1, \quad \Lambda_{eo} = \frac{1}{4}, \\ &K^{\pm}(y) = k_1^{\pm}(-1)^y + k_2^{\pm} y (-1)^y, \quad \Lambda_{eo} = 0. \end{aligned} \tag{3.13}$$

Here, r_0 and $1/r_0$ are the roots of the algebraic equation resulting from Eq. (3.8):

$$(r+1)^2=4\Lambda_{eo}(r-1)^2. \tag{3.14}$$

Substituting relation (3.12) into Eq. (3.9) one can relate the coefficients:

$$k_1^-=2\Lambda_e k_1^+\frac{1-r_0}{1+r_0},\quad k_2^-=2\Lambda_e k_2^+\frac{r_0-1}{1+r_0}, \tag{3.15}$$

or, equivalently,

$$k_1^+=2\Lambda_o k_1^-\frac{1-r_0}{1+r_0},\quad k_2^+=2\Lambda_o k_2^-\frac{r_0-1}{1+r_0}. \tag{3.16}$$

Their equivalence follows from relation (3.14). The boundary schemes fix the remaining coefficients. In case $\Lambda_{eo}=1/4$, then

$$k_1^-=2\Lambda_e k_1^+,\quad k_2^-=-2\Lambda_e k_2^+.$$

In case $\Lambda_o=0$, $k_2^-=-4\Lambda_e k_1^+$, $k_2^+=0$ and k_1^- is related to k_1^+ via the microscopic boundary condition at $y=0$.

The Stokes part of the solution $\{n_q^{+(S)},n_q^{-(S)}\}$, given by relation (3.2), defines the effective width of the channel. The remaining solution, $\{\delta p_q^{(S)}/\lambda_e,\delta m_q^{(S)}/\lambda_o\}$ represents a sum of non-linear term expansion, relations (3.6), and the Knudsen layer (3.11):

$$\begin{aligned}&\delta p_q^{(S)}=\delta p_q^{(ch)}+g_q^+=\rho_0 T_q G^+(y)c_{qy}^2,\quad G^+=(H^++K^+),\\&\delta m_q^{(S)}=\delta m_q^{(ch)}+g_q^-=\rho_0 T_q G^-(y)c_{qy},\quad G^-=(H^-+K^-).\end{aligned} \tag{3.17}$$

Provided that the same (or equivalent) $M_q^{(u)}$ scheme is applied for all incoming links at one wall, their closure relations are *equivalent for all cut links* on the solution (3.17). Let us represent them at the top ($i=t$) and bottom ($i=b$) as:

$$a_p^{(i)}\delta p_q^{(S)}(\vec{r}_b)+a_m^{(i)}\delta m_q^{(S)}(\vec{r}_b)=a_c^{(i)}(\vec{r}_b),\quad q\in\Pi^{(u)}(\vec{r}_b),\quad i=\{t,b\}, \tag{3.18}$$

where

$$\begin{aligned}\text{BB,CLI,ULI/DLI,YLI:}\quad & a_p^{(i)}=\beta^{(u)},\quad a_m^{(i)}=\beta^{(p)},\quad a_c^{(i)}=0,\\&\beta^{(u)}=\alpha^{(u)}\delta_q,\quad \beta^{(p)}=\alpha^{(u)}\beta^{(p\star)};\\\text{MLI}(\alpha^{(u)}):\quad & a_p^{(i)}=\beta^{(u)},\quad a_m^{(i)}=0,\quad a_c^{(i)}=0,\quad \beta^{(u)}=\alpha^{(u)}\delta_q,\\\text{MR1:}\quad & a_p^{(i)}=(4\Lambda_{eo}-(1+\delta_q))\delta_q,\quad a_m^{(i)}=-2\delta_q^2\Lambda_o,\\&a_c^{(i)}=\delta_q^2\Lambda_o(u_x^2(1)-u_x^2(0)),\quad \text{if }\ \Lambda_{eo}\neq\frac{1}{4},\\\text{MR1:}\quad & a_p^{(i)}=-(4+3\delta_q)\delta_q,\quad a_m^{(i)}=-2\delta_q^2\Lambda_o,\\&a_c^{(i)}=\delta_q^2\Lambda_o(u_x^2(2)-u_x^2(1)),\quad \text{if }\ \Lambda_{eo}=\frac{1}{4}.\end{aligned} \tag{3.19}$$

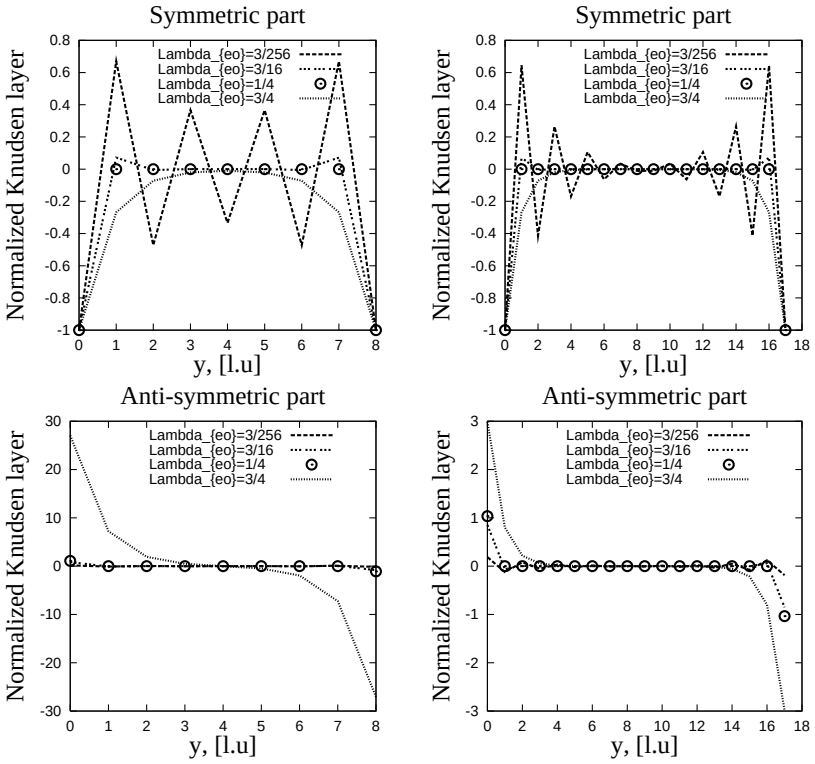

Figure 3: Test II. Normalized, symmetric and anti-symmetric components $K^{\pm}(y)/H^{\pm}(0)$ of the Knudsen layer solution are plotted. They are obtained in an open channel using MULI at the horizontal boundaries. The numerical solution (symbols) lies exactly on the analytical curve (3.12); the parameters are fixed by relations (3.15)–(3.16) and the MLI boundary conditions (3.19). Left: $L_y=9$, Right: $L_y=18$. Data: $\nabla_x P=0$, $\nu=1$, $F_x=10^{-3}$ (coarse grid) and $F_x=\frac{1}{8}\times 10^{-3}$ (fine grid).

For MR1, the steady closure relation involves a neighbor solution along a link. Two TRT evolution relations have been first involved to express $\delta m_q^{(S)}(\vec{r}_{\rm b}-\vec{c}_q)$ and $\delta p_q^{(S)}(\vec{r}_{\rm b}-\vec{c}_q)$ via $\delta m_q^{(S)}(\vec{r}_{\rm b})$ and $\delta p_q^{(S)}(\vec{r}_{\rm b})$. When $\Lambda_{eo}=1/4$, the neighbor point solution is

$$\delta p_q^{(S)}=\delta p_q^{(ch)},\quad \delta m_q^{(S)}=\delta m_q^{(ch)}.$$

It is expressed here with help of the finite-difference equivalent form of the TRT equations.

Finally, the Knudsen layer is described by relations (3.11)-(3.13). Its four coefficients are first related via two relations (3.15) (or (3.16)) and then derived from the boundary relations (3.19), substituting there (3.17) with relations (3.6). These solutions can be computed using the *effective (Stokes) solution* for $u_x(y)$, corresponding to a selected scheme. Numerical results confirm the analytical predictions for all considered schemes. As an example, the solution obtained with MULI is shown in Fig. 3. We plot the normalized values, $K^+(y)/H^+(0)$ and $K^-(y)/H^-(0)$. In agreement with the solution (3.19) for MLI

family, $K^+(y)+H^+(y)=0$ in boundary points $y=0$ and $y=L_y-1$, then $K^+(y)/H^+(0)$ equals to -1 there. For $\Lambda_{eo}=1/4$, the Knudsen layer vanishes at bulk points in agreement with relations (3.13). When $\Lambda_{eo}<1/4$, the accommodation oscillates, otherwise is decreases exponentially toward the center of the channel.

When $\delta_q=0$, MULI and MR(k) do not constrain the non-equilibrium at the boundary point. The coefficients of Knudsen layer solution are then not fixed and the accommodation may vanish. Linear schemes fix the solution (3.12). When $\Lambda_o=0$ (linear stability limit), then $\delta p_q^{(ch)}\equiv 0$ and $a_m^{(i)}$ vanishes except for "non-magic" linear interpolations (e.g., ULI/DLI, YLI). For them, the unique solution is fixed in a form (3.13) and, e.g., if two walls are placed on the same distance, then

$$K^+(y)=k_1^+(-1)^y,\quad K^-(y)=-4\Lambda_e k_1^+(-1)^y(y-\frac{L_y-1}{2}).$$

When $a_m^{(i)}=0$, e.g., BB, CLI, MLI, and MR1, the solution is not fixed and, in particular, the zero Knudsen solution ($K^+\equiv 0$, $K^-\equiv 0$) satisfies the system.

This example of the Poiseuille flow modeled with the Navier-Stokes equilibrium and inexact boundary conditions shows that the Knudsen layer population solution happens to have no impact on the macroscopic solution, invariant along the channel.

3.2.3 Dirichlet velocity and mixed conditions

Let us analyze now the situation in closed boxes. Both $M_q^{(u)}$ and $M_q^{(m)}$ schemes, applied at the vertical boundaries, constrain the Navier-Stokes component of the population solution. They do not maintain the Knudsen layer solution in a form (3.11) unless the non-equilibrium component vanishes from the closure relation. This is the case, e.g., for the MLI closure relations when $\delta_q^{(v)}=0$. The open channel effective solution is valid then in a closed box. The simplest test to check for this consists of using BB for all links which cut the horizontal boundaries and prescribing the effective Stokes solution via MLI at $\delta_q^{(v)}=0$. Similarly, $M_q^{(p)}$ supports the Knudsen layers in a form (3.11) when the non-equilibrium part vanishes from its closure relation, e.g., for the combination of PLI or PMR2 and MLI when $\delta_q^{(v)}=0$.

When $\delta_q^{(v)}\neq 0$, the macroscopic solutions differ in open and closed boxes. On the fixed grid, the non-dimensional velocity and pressure solutions are fixed by Λ_{eo} and the grid Reynolds number $Re_g=U/\nu$. One can check this running two experiments with

$$\frac{\nu^{(1)}}{\nu^{(2)}}=k,\quad \frac{\nabla_x P^{(1)}-f_x^{(1)}}{\nabla_x P^{(2)}-f_x^{(2)}}=k^2$$

(then $\frac{U^{(1)}}{U^{(2)}}=k$, $Re_g^{(1)}=Re_g^{(2)}$, $\forall k$) and

$$\Lambda_{eo}^{(1)}=\Lambda_{eo}^{(2)}.$$

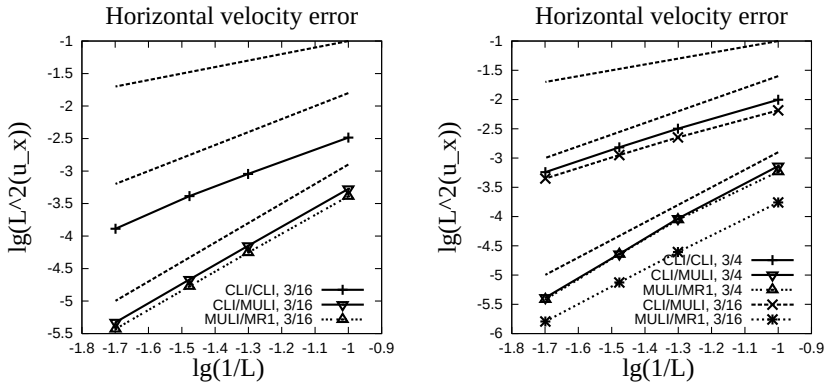

Figure 4: Test II. Convergence rates in an L^2-box, $L=10,20,\ldots,50$, for the Dirichlet velocity conditions. The legend indicates the velocity scheme on the horizontal/vertical walls and the Λ_{eo} value. Left: $\delta_q^{(h)}=1/2$, $\delta_q^{(v)}=1/4$. Right: $\delta_q^{(h)}=1$, $\delta_q^{(v)}=1/10$. The dotted lines with no symbols visualize the h,h^2,h^3-slopes.

Let P_0 be some reference value, e.g., the pressure in the center of the box. We confirm that the parametrization properties of the steady solutions for BB, CLI, MGLI$(\alpha^{(u)})$ and for the parabolic velocity schemes (or their combinations) and for the pressure schemes PMR(k) (with PAB/PLI for second-type link). The two solutions are identical for $\vec{u}'=\vec{j}/(\rho_0 U)$ (hence, for $L^2(u_x)$) and, at least when

$$\frac{\nabla_x P^{(1)}}{\nabla_x P^{(2)}}=k^2$$

or

$$\frac{f_x^{(1)}}{f_x^{(2)}}=k^2, \quad \text{for } P'=\frac{P-P_0}{\rho_0 U^2}.$$

These solutions are independent from the selected value of c_s^2. We emphasize that using the compressible equilibrium form, $t_q^\star E_q^+(\vec{j},\rho)$ in relations (2.3), $\vec{u}'(\vec{r})$ and $P'(\vec{r})$ are fixed only if $Ma^2=U^2/c_s^2$ is kept constant (e.g., adjusting c_s^2).

Next we examine the following configurations. The CLI scheme is applied for the horizontal walls shifted at $\delta_q^{(h)}=1/2$ and $\delta_q^{(h)}=1$. We use the effective solutions (2.22), $\Lambda_{eo}=3/16$ and $\Lambda_{eo}=3/4$, respectively. The velocity condition is first applied at the inlet/outlet for $\delta_q^{(v)}=1/4$ and $\delta_q^{(v)}=1/10$, respectively. We recall that using the Stokes equilibrium ($g_S=0$) and PMR1, PMR2 in combination with the linear/parabolic schemes, the solution is exact for any $\delta_q^{(v)}$. The convergence rates for $g_S=1$ are plotted in Figs. 4 for $\nu=1/18$,

$$F_x=-\nabla_x P=\frac{1}{9n^3}\times 10^{-3}, \quad n=1,2,\cdots,5,$$

from coarse to fine grid. They confirm that CLI and MLI$(\alpha^{(u)})$ applied to the horizontal boundary have equal accuracy when Λ_{eo} is chosen properly for CLI (cf., CLI/MULI, $\Lambda_{eo}=$

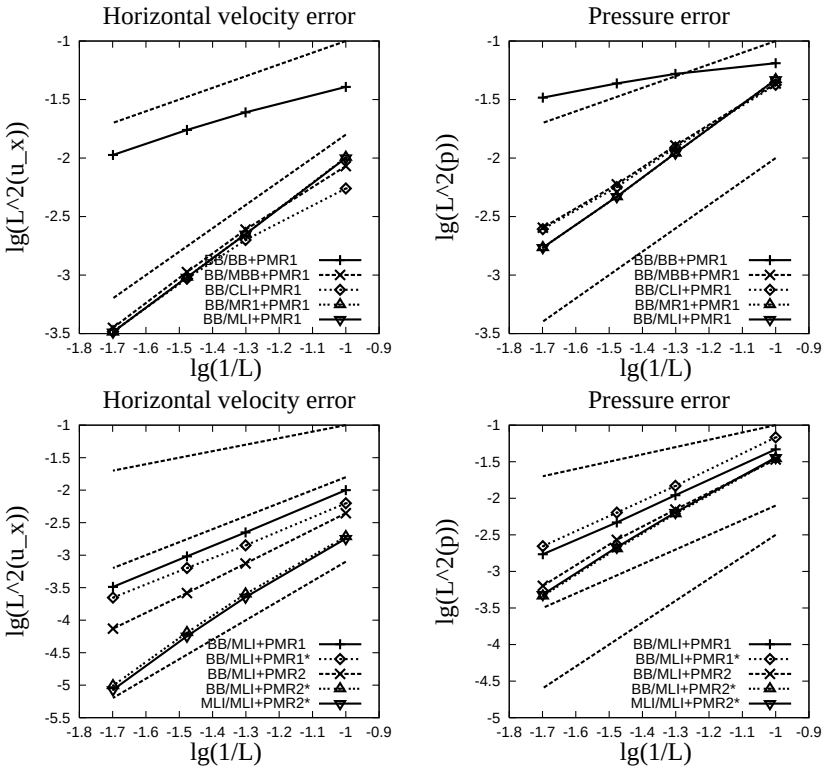

Figure 5: Test II. Convergence rates in an L^2-box, $L=10,20,\ldots,50$. Top row: The bounce-back condition is applied at the horizontal walls for $\delta_q^{(h)}=1/2$. The mixed scheme is applied at the inlet/outlet using PMR1 in combination with BB, MBB, CLI, MR and MLI for $\delta_q^{(v)}=1/4$. Bottom row: BB and MLI are at the horizontal walls, PMR1 and PMR2 are combined with MLI at the vertical walls. MLI+PMR1* and MLI+PMR2* use exact solutions for inlet/outlet normal velocity component instead of the approximations (2.35). The dotted lines with no symbols visualize the h,h^2-slopes (top row) and the h,h^2,h^3-slopes (bottom row). $\Lambda_{eo}=3/16$ for all tests.

$3/16$ (left) and $\Lambda_{eo}=3/4$ (right) to MULI/MR1). Otherwise, e.g., taking $\Lambda_{eo}=3/16$ when $\delta_q^{(h)}=1$ (see CLI/MULI, right picture), or using CLI at the vertical walls when $\delta_q^{(v)}\neq\delta_q^{(h)}$ (see CLI/CLI, both left and right pictures), the decay rates reduce to $\mathcal{O}(h^2)$, in agreement with the predictions. The CLI is applied here in combination with MGULI/MGDLI for the second type links. We find in the different tests that this combination works robustly.

As expected, the parabolic schemes yield third-order convergence rates for distinct Λ_{eo} values. Next, the mixed condition is applied at the inlet/outlet using PMR1 in combination with BB, MBB, CLI, MR and MLI (here, $\delta_q^{(h)}=1/2$, $\delta_q^{(v)}=1/4$, $\Lambda_{eo}=3/16$). The results are plotted in the top row in Fig. 5. As we could expect, PMR1+BB is only first order accurate (asymptotically) for u_x and still worse for the pressure when $\delta_q^{(h)}\neq\delta_q^{(v)}$ (the convergence is one order faster for both pressure and velocity when $\delta_q^{(v)}=\delta_q^{(h)}$ and Λ_{eo} satisfies relation (2.22)). We observe that the velocity error converges less rapidly than we

would expect for all other combinations, fitting $\mathcal{O}(h)-\mathcal{O}(h^2)$ for MBB and CLI, $\mathcal{O}(h^2)$ for MR1 and MLI. The error decays similarly for the pressure. We emphasize that we use the normalized pressure values for the convergence tests: the pressure value obtained in the node closest to the center of the channel is subtracted from the obtained solution (and similarly for the reference one).

We verify first that the slower convergence is not due to the application of BB at the horizontal walls: here the parabolic schemes at the horizontal walls and corners yield nearly the same results. The results plotted in the bottom pictures in Fig. 5 investigate further this problem. Using the exact solution for $u_x(\vec{r}_{\rm w})$ in $w_q^{(u)}(\vec{r}_{\rm w},\widehat{t})$ and $w_q^{(p)}(\vec{r}_{\rm w},\widehat{t})$ for the mixed condition decreases the magnitude of the error but does not alter its convergence (cf. BB/MLI+PMR1 and BB/MLI+PMR1*). However, switching to PMR2 (which is accurate for the term $\partial_q\Lambda_o\partial_q\Pi_q^\star$ in $p_q^{(2)}$), clearly improves the convergence (see BB/MLI+PMR2). Finally, combining PMR2 with the exact solution for the inlet/outlet normal velocity component, instead of the approximations (2.35), we get third-order convergence for both velocity and pressure (see BB/MLI+PMR2$*$ and MLI/MLI+PMR2*, which give nearly the same results owing to Λ_{eo}).

This test shows that the impact of the $\partial_q\Lambda_o\partial_q\Pi_q^\star$ term may spoil the third-order velocity convergence when its distribution is parabolic in space, as for non-linear equilibrium distribution. It was suggested in [16], Section 7.5, that when the velocity profile is not invariant along the normal direction, so that the mixed derivative $\partial^2_{\tau n}u_n$ becomes significant, the second-order approximation errors of the linear approximations (2.35) are no longer canceled due to symmetry. The present test confirms that they may induce the additional second-order errors for the mixed schemes, via the $w_q^{(u)}$ term in their $M_q^{(u)}$ component.

3.3 Test III: Linear velocity/parabolic pressure solution

Let us consider now the inverse situation, when the exact velocity solution is linear and pressure distribution is parabolic. They represent exact steady solution of the incompressible N-S-E (see also in [25]):

$$\begin{aligned}
&u_x(x,y)=ax+by,\quad u_y(x,y)=bx-ay,\\
&P(x,y)=P^{ex}(x,y),\quad \vec{F}(x,y)\equiv 0,\quad \text{or,}\\
&\vec{F}(x,y)=-\nabla P^{ex}(x,y),\quad P\equiv P_0,\\
&P^{ex}(x,y)=P_0-\rho_0\frac{(a^2+b^2)}{2}(x^2+y^2).
\end{aligned}\tag{3.20}$$

Taking $g_S=1$ in relations (2.3), the exact solution is given by the steady form of third-order Chapman-Enskog expansion [16] where we set $\partial^2_{\widehat{q}}j_q^\star\equiv 0$, $\partial^2_{\widehat{q}}F_q^\star=0$, then:

$$\begin{aligned}
&m_q^{ch}=\partial_q\Pi_q^\star-S_q^-,\\
&p_q^{ch}=\partial_q j_q^\star-\partial_q\Lambda_o(\partial_q\Pi_q^\star-F_q^\star).
\end{aligned}\tag{3.21}$$

Prescribing exact Dirichlet values for velocity and pressure one can validate the method for any shape of the external boundary. Giving linear force distribution, one can check the boundary schemes in the presence of a force gradient. Unlike for Poiseuille flow, the closure relations do not need to capture the viscous term $-\Lambda_e\partial_q^2 j_q^\star$ but need to match $\partial_q^2\Pi_q^\star$ (or $\partial_q F_q^\star$). Exact boundary conditions require then $j^{(2)}/\Pi^{(3)}/F^{(2)}$ accuracy.

3.3.1 Exact solutions with the special schemes

Both the MLI($\alpha^{(u)}$) and MR(k) families are exact for linear pressure and/or constant forcing distributions, but not for the next order term $\partial_q\Lambda_o(\partial_q\Pi_q^\star - F_q^\star)$. This term vanishes however from the closure relations for MLI($\alpha^{(u)}$) and MR1 when $\delta_q = 0$. Applying these schemes for all boundaries when $\delta_q^{(h)} = \delta_q^{(v)} = 0$ (with and without forcing) and starting from the exact solution, the method will maintain it. However, as we discussed above, steady solution is not unique for the parabolic schemes when the boundary lies on the grid points. For a particular choice $C = \delta_q$, the MGMR2 scheme from the MGMR(C) subfamily becomes exact for a parabolic pressure distribution. This choice however only approaches the stability limit when $\Lambda_o \to 0$. As an example, we mention that for $\nu = 1/18$ (used below) the solutions are stable when, roughly, $\Lambda_o < 1/50$. When the force is not constant, its gradient can be removed from the closure relation with a help of the special correction:

$$f_q^{\text{p.c.}(u)} \to f_q^{\text{p.c.}(u)} - \delta_q\Lambda_o\partial_q F_q^\star.$$

The special pressure scheme, PMR2 is also exact for this solution. It can be applied in combination with any parabolic velocity scheme (their error for the $\partial_q(\partial_q\Pi_q^\star - F_q^\star)$ vanishes from the mixed constraints due to symmetry). The five populations based schemes can not be applied however for the second-type links. Just for testing, one can compute them with the exact solution (3.21).

3.3.2 Dirichlet velocity and mixed conditions

Let us apply now the general schemes. They are all exact for the linear velocity distribution. We apply the "magic" linear and parabolic velocity schemes and fix the non-dimensional distributions,

$$\vec{j}' = \frac{\vec{j}}{\rho_0 U}, \quad P' = \frac{P - \bar{P}}{\rho_0 U^2}$$

for each grid with Λ_{eo} and $Re_g = U/\nu$ (again, we measure the pressure error centering it around $\bar{P}$, the value obtained in the center nodes). The Dirichlet velocity conditions are first prescribed for all boundaries using BB, MGDLI/MGULI, MR1 and MDLI/MULI. The convergence velocity rates are plotted in Fig. 6 for two cases: $\delta_q^{(v)} = \delta_q^{(h)} = 1$ (left picture) and $\delta_q^{(h)} = 3/4$, $\delta_q^{(v)} = 1/4$ (the middle and right pictures). The convergence and the accuracy are similar for two cases. The results fit, as expected, $\mathcal{O}(h)$ for BB and $\mathcal{O}(h^3)$ for MR1 and MDLI/MULI. The convergence is only between $\mathcal{O}(h)$ and $\mathcal{O}(h^2)$ for MGDLI/MGULI on the coarse grids and it tends asymptotically to $\mathcal{O}(h^2)$. Similar

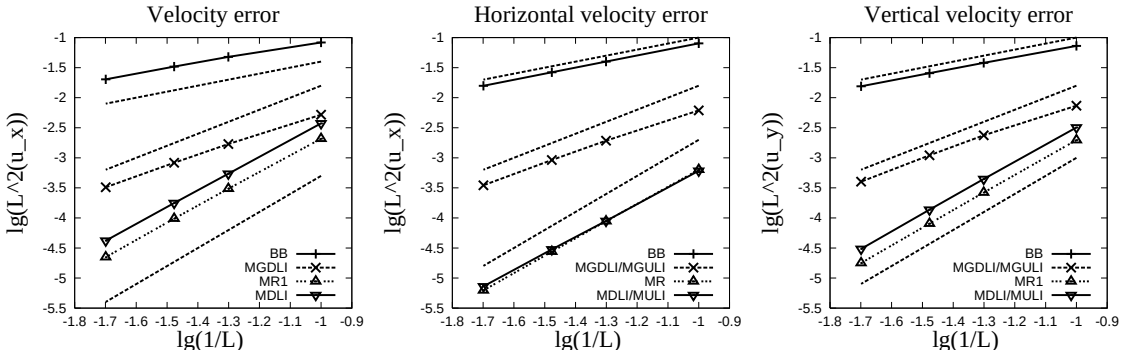

Figure 6: Test III. Convergence tests in case of the Dirichlet velocity conditions at all boundaries in an L^2-box, $L=10,20,\cdots,50$. Left: $\delta_q^{(v)}=\delta_q^{(h)}=1$, $L^2(u_x)=L^2(u_y)$. Middle and Right: $\delta_q^{(h)}=3/4$, $\delta_q^{(v)}=1/4$. Data: $\nu=1/18$, $\Lambda_{eo}=3/16$ and $a=0$, $b=(10n)^{-2}$, $n=1,2,3,5$ from coarse to fine (the coefficients a and b given by relations (3.20)). The dotted lines with no symbols visualize the h,h^2,h^3 slopes.

convergence rates are obtained for the "non-magic", DLI/ULI schemes, but their effective accuracy is not controlled with Λ_{eo}. The parabolic schemes therefore retain their formal third-order accuracy in the presence of the non-linear pressure solution. The convergence behavior is similar for MR1 and MULI/MDLI but we find usually that MR1 is the most accurate.

Next, the mixed schemes prescribe then exact distributions for the pressure and the tangential velocity u_y at the east and west boundaries, linear approximations (2.35) are used for normal velocity u_x. The obtained convergence rates are plotted in Fig. 7. Equal $M_q^{(u)}$ schemes are used for the horizontal and the vertical boundaries, except for the combination MGDLI/(PMR1+MCLI) (MGDLI on the horizontal boundary, $M_q^{(p)}$=PMR1 and $M_q^{(u)}$ = MCLI for the mixed scheme). For the linear velocity schemes, CLI and MGDLI, the convergence is only between $\mathcal{O}(h)$ and $\mathcal{O}(h^2)$ for both velocity components (asymptotically tending to $\mathcal{O}(h^2)$), similar to the previous test. When MBB (modified bounce-back (3.4)) is applied for the mixed scheme, the velocity errors increase with one order of magnitude compared to CLI, in agreement with the predictions for the non-channel flows, but their pressure solutions are similar. Unlike for non-linear Poiseuille flow in the previous test, the parabolic schemes, MCLI and MR1 mixed components result here in $\mathcal{O}(h^3)-\mathcal{O}(h^4)$ rates.

The prescribed value of the central pressure is $P_0=1/3$ in all the tests below. The decay rates of the pressure error with both PMR1 and PMR2 fit $\mathcal{O}(h^3)$ when they are combined with the parabolic schemes, and $\mathcal{O}(h^2)$ when they are combined with the linear schemes, or when the linear scheme is applied to the horizontal boundaries and corners (see MGDLI/PMR1+MCLI). Being exact for the parabolic pressure distribution, the PMR2 scheme shows a smaller pressure error but it does not gain in convergence against PMR1 when the velocity schemes do not yield this property. Altogether both

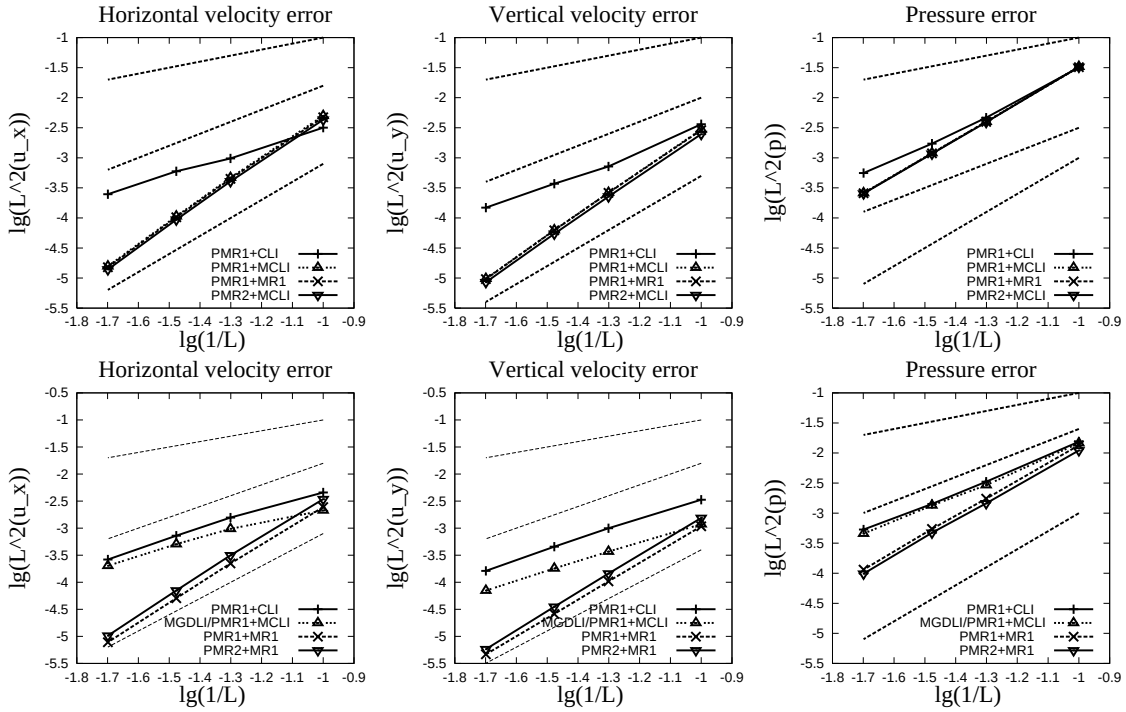

Figure 7: Test III. Convergence tests in case of Dirichlet velocity conditions on the horizontal walls and the mixed conditions at the inlet/outlet. Top row: $\delta_q^{(v)}=\delta_q^{(h)}=1/2$. Bottom row: $\delta_q^{(h)}=3/4$, $\delta_q^{(v)}=1/4$. The same velocity scheme is used for the horizontal/vertical boundaries unless two velocity schemes are indicated. The pressure schemes are PMR1 and PMR2. Data: $\nu=1/18$, $\Lambda_{eo}=3/64$ and $a=0$, $b=(10n)^{-2}$, $n=1,2,3,5$. The dotted lines with no symbols visualize the h,h^2,h^3-slopes.

Test II and Test III, which can be regarded as "viscous dominant" and "convection dominant" flow examples, confirm the advanced accuracy and convergence of the parabolic schemes with respect to the linear ones, for both velocity and mixed conditions. We recall that replacing CLI with MGULI/MGDLI, which do not support the staggered invariants unless $\delta_q=1/2$, will result in the same steady solutions. We find that PMR1 is most stable when the pressure boundaries lie closer to the grid nodes, $\delta_q\in[0,1/2]$ and when $\Lambda_o\to 0$ if $\delta_q\to 1$.

3.3.3 Special case $\delta_q^{(h)}=\delta_q^{(v)}=0$ with mixed scheme

The CLI replaces the parabolic schemes on the horizontal walls. The results are presented in Table 6 and illustrated in Fig. 8 using PMR1 for all tests. They show a substantial discrepancy of BB with other schemes, especially for the pressure. Bounce-back spoils the total results even when it is applied only for one corner link (see (CLI+BB)/CLI, (horizontal boundary+corner)/vertical boundary). One gets then an impressive improving replacing BB with CLI. Applying MCLI as the component of the mixed condition clearly improves the accuracy for the tangential velocity u_y. Fig. 8 demonstrates the highest

Table 6: Test III. The results for the mixed condition when the walls are located at grid nodes ($\delta_q^{(h)}=\delta_q^{(v)}=0$). The first and second columns indicate the $M_q^{(u)}$ schemes used on the horizontal wall for standard and second-type links, respectively. The third column indicates the $M_q^{(u)}$ scheme used in combination with PMR1 for the mixed scheme. Data: $L_x=L_y=10$, $a=b=2.25\times10^{-3}$, $\nu=1$.

			$\Lambda_{eo}=\frac{3}{64}$			$\Lambda_{eo}=\frac{3}{4}$		
$M_q^{(u)}$			$L^2(u_x)$	$L^2(u_y)$	$L^2(p)$	$L^2(u_x)$	$L^2(u_y)$	$L^2(p)$
BB	BB	BB	1.9×10^{-2}	9.9×10^{-2}	14.65	1.8×10^{-1}	8.9×10^{-2}	1.69
CLI	BB	CLI	1.3×10^{-2}	6.2×10^{-3}	2.89	2.2×10^{-2}	4.7×10^{-3}	1.45
CLI	CLI	CLI	3.7×10^{-4}	1×10^{-4}	9.1×10^{-2}	1.9×10^{-3}	1.3×10^{-3}	5.1×10^{-2}
CLI	CLI	MCLI	3.9×10^{-4}	6.8×10^{-5}	9.8×10^{-2}	2.2×10^{-3}	9.3×10^{-5}	3.0×10^{-2}

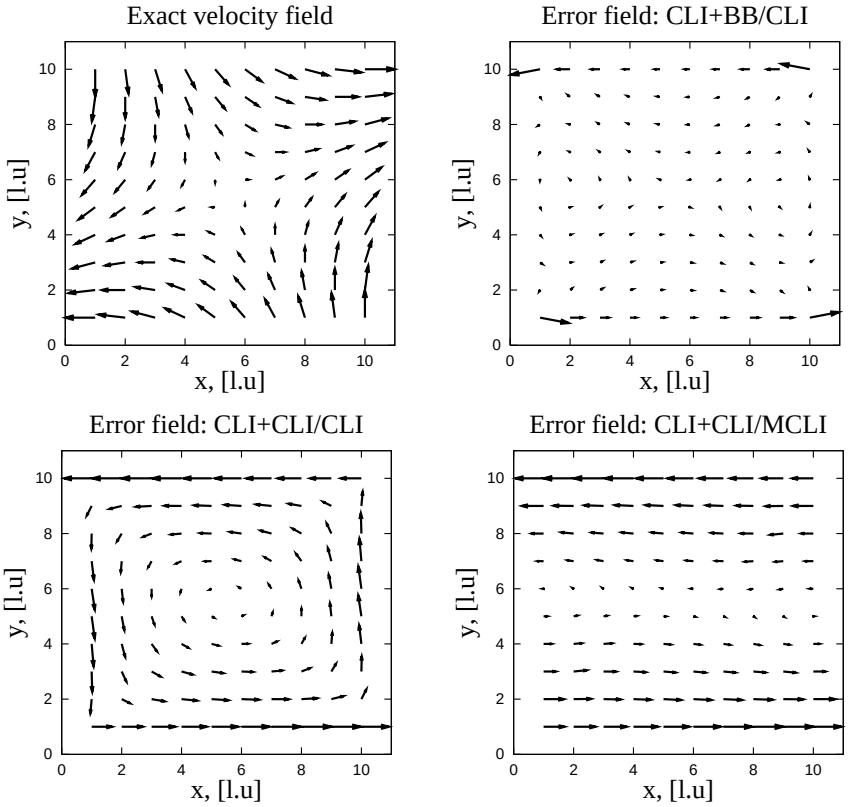

Figure 8: Test III. The exact solution (first picture) and the normalized error distribution when the walls are located at grid nodes, $\delta_q^{(h)}=\delta_q^{(v)}=0$ and the mixed scheme is applied for vertical boundaries. The date corresponds to $\Lambda_{eo}=3/4$ in Table 6. Vector fields are scaled with their highest amplitude, $\sqrt{u_x^2+u_y^2}=0.02025$ and $\sqrt{(u_x-u_y^{ex})^2+(u_y-u_y^{ex})^2)}$ (equal to 8.5×10^{-4} for CLI+BB/CLI, 3.9×10^{-5} for CLI+CLI/CLI and 3.8×10^{-5} for CLI+CLI/MCLI).

errors in corners when (CLI+BB)/CLI are used as the velocity schemes. The error is distributed uniformly for all walls with (CLI+CLI)/CLI. Finally, the error field is mostly concentrated near the horizontal walls for (CLI+CLI)/MCLI, i.e. when MCLI improves the tangential constraint on the vertical boundaries in agreement with the analysis. As above, replacing of CLI with MGULI and MCLI with MULI will lead to the same steady solutions but minimizes the risque of developing of the staggered solutions.

4 Test IV. Womersley-type pulsatile flow

The test problem [17] restricts the pipe-flow solution [43] to infinite two-dimensional channel. Velocity $\vec{u}^{(w)}=\{u_x^{(w)}(y,t),0\}$ and pressure $P^{(w)}(x,t)$ obey incompressible Stokes flow equation governed by an oscillating pressure gradient:

$$\begin{aligned}&\nabla\cdot u_x^{(w)}=0,\quad \partial_t u_x^{(w)}+\partial_x P^{(w)}=\nu\partial_y^2 u_x^{(w)},\\&P^{(w)}(x)=Ax\cos(\omega t),\quad w=\frac{2\pi}{T},\\&u_x^{(w)}(y=\pm l_y)=0,\quad -l_y\le y\le l_y,\quad -\infty\le x\le\infty.\end{aligned}\tag{4.1}$$

The real part of the solution is:

$$\begin{aligned}&u_x^{(w)}(y,t)=u_x^{(w,1)}(Y,t)+u_x^{(w,2)}(t),\quad Y=\frac{y}{l_y},\\&u_x^{(w,1)}(Y,t)=\frac{A}{\omega}u_w(k'_w,k''_w,Y,t),\quad u_x^{(w,2)}(t)=-u_x^{(w,1)}(\pm1,t),\end{aligned}\tag{4.2}$$

where

$$\begin{aligned}&u_w(k',k'',Y,t)=r(k',k'',Y)\cos(\omega t)+p(k',k'',Y)\sin(\omega t),\\&r(k',k'',Y)=\frac{2}{\gamma}(\sin(k')\sinh(k'')\cos(k'Y)\cosh(k''Y)\\&\qquad\qquad-\cos(k')\cosh(k'')\sin(k'Y)\sinh(k''Y)),\\&p(k',k'',Y)=\frac{2}{\gamma}(\cos(k')\cosh(k'')\cos(k'Y)\cosh(k''Y)\\&\qquad\qquad+\sin(k')\sinh(k'')\sin(k'Y)\sinh(k''Y)),\\&\gamma=\cos(2k')+\cosh(2k'')=2(\cos^2(k')+\cosh^2(k'')).\end{aligned}\tag{4.3}$$

The Stokes Eq. (4.1) is satisfied if k'_w and k''_w are related to the Womersley number Wn as

$$k'_w=-k''_w=-\sqrt{\frac{\mathrm{Wn}^2}{2}},\quad k_w^2=(k'_w+ik''_w)^2=-i\mathrm{Wn}^2,\quad \mathrm{Wn}^2=\frac{l_y^2\omega}{\nu}.\tag{4.4}$$

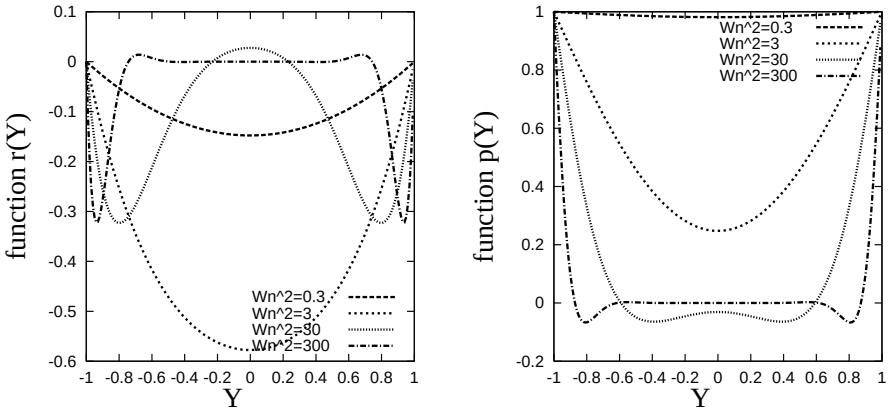

Figure 9: The functions $r(Y)$ and $p(Y)$.

The functions $r(Y,\mathrm{Wn}^2)$ and $p(Y,\mathrm{Wn}^2)$ are plotted in Fig. 9. They obey the following boundary conditions:

$$r(k',k'',\pm 1=0, \quad p(k',k'',\pm 1)=1, \quad \forall k',k'',$$

then

$$u_x^{(w,2)}(t)=-\frac{A}{\omega}p(k'_w,k''_w,\pm 1)\sin(\omega t)=-\frac{A}{\omega}\sin(\omega t). \tag{4.5}$$

The simplest way to verify the LB method for the incompressible Womersley-type solution is to replace the pressure gradient with a prescribed local forcing. We study first this case for both periodic and closed boxes. The pressure drop is then prescribed via the time dependent mixed conditions at the ends $x=\pm l_x$. The pressure oscillation $\partial_t P$ becomes negligible in continuity equation only when $c_s \gg L_x/T$, $L_x=2l_x$ (see in [17]). With the purpose to verify also the rapid oscillations, we construct in Appendix B the approximate solution to compressible Stokes Eq. (2.7), setting the exact velocity profiles as a Dirichlet boundary condition for all boundaries.

4.1 Modeling of Womersley flow with forcing

Except for one special test below, we use forcing explicit in time:

$$F_x(t)=-\rho_0\partial_x P^{(w)}(x,t)=-A\rho_0\cos(\omega t), \quad \omega=\frac{2\pi}{T}. \tag{4.6}$$

We set $\rho_0=1$, then $\vec{u}=\vec{j}$ for all simulations below.

4.1.1 Open channel

Using periodic conditions, the density $\rho(x,y,t)$ is constant, the velocity is linear with respect the amplitude A and the solutions are identical for both the Stokes and Navier-Stokes equilibriums. We recall that the Poiseuille solution has this property owing to the special form of the Knudsen layer solution in an open channel. In closed boxes, the macroscopic solutions differ for linear and non-linear equilibrium, and we use the Stokes equilibrium function for all simulations below.

Experiment 1

Let us first set the distance to the horizontal walls $\delta_q^{(h)}$ equal to 1 and put $\lambda_e=\lambda_o=-1$ ($\Lambda_e=\Lambda_o=1/2$), then

$$f_q(\vec{r},t+1)=e_q(\vec{r}-\vec{c}_q,t)+S_q^-,\ \forall\vec{r}.$$

If the pulsatile solution would be an exact solution of the TRT operator with the forcing (4.6), and prescribing then the exact equilibrium solution for the incoming populations,

$$f_{\bar{q}}(\vec{r}_b,t+1)=e_{\bar{q}}(\vec{r}_b+\vec{c}_q,t)+S_{\bar{q}}^-,$$

the model would stay on the exact solution starting from the exact equilibrium distribution (in this particular set-up). Table 7 shows the mean error we get,

$$L^{2T}(u_x)=\frac{1}{n_T}\sum_t L^2(u_x,t)$$

(hereafter, when the time-harmonic motion is attained, we mostly measure the error every 5^{th} time step, $n_T=T/5$).

In fact, the inexactness of the obtained solution is partially due to the discretization of the forcing. The finite-difference equivalent of the TRT model in case $\Lambda_e=\Lambda_o=1/2$, $\rho\equiv\rho_0$, $\vec{j}(y,t)=\vec{J}(y,t)+\frac{\vec{F}(t)}{2}$ is:

$$j_x(y,t+1)-j_x(y,t)-\frac{1}{2}(F_x(t)+F_x(t+1))=\frac{1}{6}\Delta_x j_x(y,t). \tag{4.7}$$

Assuming the forcing (4.6) in relation (4.7), the discretized equation

$$\partial_t u_x^{(w,2)}(t)-F_x(t)=0$$

becomes:

$$\begin{aligned}
&-A\rho_0\left(\frac{\sin[\omega(t+1)]-\sin(\omega t)}{\omega}-\frac{\cos(\omega t)+\cos(\omega(t+1))}{2}\right)\\
&=A\rho_0\frac{\cos(\omega(t+\frac{1}{2}))}{\omega}\left(\omega\cos\left(\frac{\omega}{2}\right)-2\sin\left(\frac{\omega}{2}\right)\right)\\
&\approx A\rho_0\cos\left(\omega\left(t+\frac{1}{2}\right)\right)\frac{\omega^2}{12}+\mathcal{O}(\omega^4).
\end{aligned} \tag{4.8}$$

Table 7: The mean error $L^{2T}(u_x)$ of the pulsatile solution in a periodic channel for standard (explicit) forcing (left column) and the modified one (right column) when $\Lambda_e=\Lambda_o=1/2$, $l_y=10$.

Wn^2	T	F_x with Eq. (4.6)	F_x with Eq. (4.8)
$\frac{3}{4}\pi$	1600	2.39×10^{-6}	1.46×10^{-6}
$\frac{3}{2}\pi$	800	7.29×10^{-6}	3.64×10^{-6}
3π	400	2.4×10^{-5}	7.67×10^{-6}
6π	200	8.8×10^{-5}	1.9×10^{-5}
12π	100	3.4×10^{-4}	6.6×10^{-5}
24π	50	1.3×10^{-3}	2.5×10^{-4}
48π	25	5×10^{-3}	9.3×10^{-4}

Table 8: Mean error over the period, $L^{2T}(u_x)$ versus Λ_{eo}, using the CLI scheme for two positions of the horizontal wall, $\delta_q^{(h)}=1/2$ and $\delta_q^{(h)}=1$ and small/high frequency in each case. We measure the error each 5^{th} time step for $T=800$ and each time step for $T=25$. The periodic channel has a width of $2l_y=20$. The data confirms that the best precision is reached with the solution (2.22), $\Lambda_{eo}=3/16$ for $\delta_q^{(h)}=1/2$ and $\Lambda_{eo}=3/4$ for $\delta_q^{(h)}=1$.

$\delta_q^{(h)}=\frac{1}{2}$			$\delta_q^{(h)}=1$		
	$T=800$	$T=25$		$T=800$	$T=25$
Λ_{eo}	$\mathrm{Wn}^2=12\pi$	$\mathrm{Wn}^2=48\pi$		$\mathrm{Wn}^2=12\pi$	$\mathrm{Wn}^2=48\pi$
$\frac{3}{64}$	1.7×10^{-2}	5.6×10^{-2}	$\frac{3}{16}$	4.4×10^{-2}	6.8×10^{-2}
$\frac{3}{16}$	4.4×10^{-3}	1.9×10^{-2}	$\frac{1}{4}$	4.0×10^{-2}	5.8×10^{-2}
$\frac{1}{4}$	8.4×10^{-3}	2.6×10^{-2}	$\frac{3}{4}$	2.7×10^{-2}	5.4×10^{-2}
$\frac{3}{4}$	5.9×10^{-2}	9.8×10^{-2}	1	3.7×10^{-2}	7.0×10^{-2}

The leading w^2-error can be canceled, e.g., replacing relation (4.6) with

$$F_x(t)=A\rho_0\left[-\cos(\omega t)+\frac{\omega^2}{24}\left(\cos(\omega(t-\frac{1}{2}))+\cos(\omega(t+\frac{1}{2}))\right)\right]. \tag{4.9}$$

The results in Table 7 confirm that the correction (4.9) improves the solution, especially for rapid oscillations.

Experiment 2

Let us verify now the efficiency of the solution (2.22) for translation invariant, time-harmonic flow. We apply the forcing (4.6) and place the horizontal boundaries at $\delta_q^{(h)}=1/2$ and $\delta_q^{(h)}=1$. We expect that $\Lambda_{eo}=3/16$ ($\Lambda_{eo}=3/4$, respectively) will remove the coupled time/space second-order error from the closure relation for CLI and MGLI($\alpha^{(u)}$) schemes. The results in Table 8 confirm that the effective Λ_{eo} values result in the most accurate solutions, even for very rapid oscillation ($T=25$). Figs. 10 and 11 show, for distinct

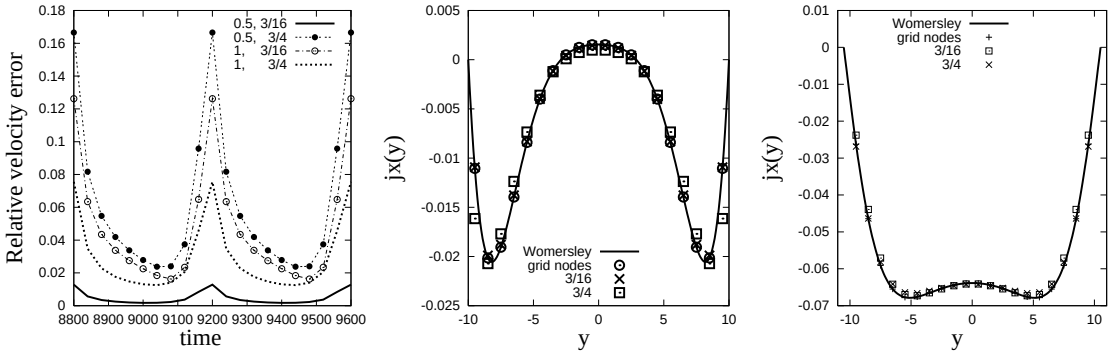

Figure 10: Test V, Experiment 2. Left: Relative error $L^2(u_x)$ along the period $T=800$ for pulsatile flow in an open channel. The legend indicates $\delta_q^{(h)}$ and Λ_{eo} values. Middle and right: the obtained profile $j_x(y,t)$ when $\delta_q^{(h)}=1/2$, $t=0$ and $\delta_q^{(h)}=1$, $t=T/4$, respectively. Data corresponds to Table 8, $\mathrm{Wn}^2=12\pi$. The effective solution (2.22) is $\Lambda_{eo}(\delta_q^{(h)}=1/2)=3/16$ and $\Lambda_{eo}(\delta_q^{(h)}=1)=3/4$.

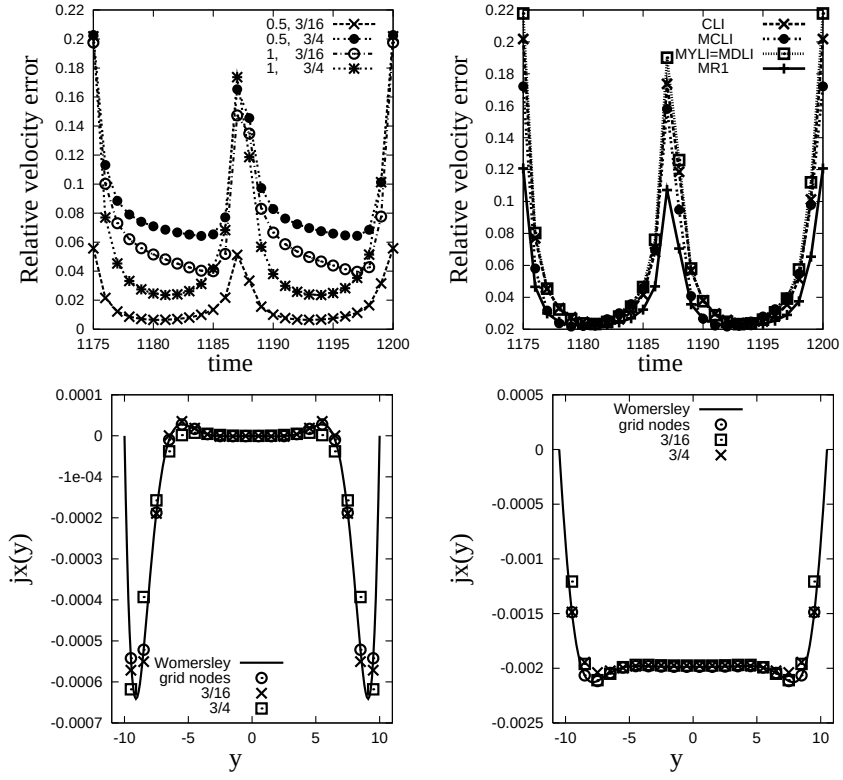

Figure 11: Test V, Experiment 2. The top row pictures plot the relative error $L^2(u_x)$ versus Λ_{eo} along the period $T=25$. Left: CLI, $\delta_q^{(h)}=1/2$ and $\delta_q^{(h)}=1$. Right: different schemes, $\delta_q^{(h)}=1$, $\Lambda_{eo}=3/4$. The data correspond to Tables 8 and 9, $\mathrm{Wn}^2=48\pi$. The bottom row pictures show the profiles $j_x(y,t)$. Left: $\delta_q^{(h)}=1/2$, $t=0$. Right: $\delta_q^{(h)}=1$, $t=6T/25$. The legends give the values of $\delta_q^{(h)}$ and Λ_{eo}.

Table 9: $L^{2T}(u_x)$ for parabolic schemes versus Λ_{eo} when $\mathrm{Wn}^2=48\pi$, $T=25$, $\delta_q^{(h)}=1$. The corresponding CLI results are presented in the last column in the previous table.

Λ_{eo}	MDLI=MYLI	MCLI	MR1
$\frac{3}{16}$	6.6×10^{-2}	3.9×10^{-2}	4.6×10^{-2}
$\frac{1}{4}$	5.8×10^{-3}	3.3×10^{-2}	4.2×10^{-2}
$\frac{3}{4}$	5.7×10^{-2}	4.9×10^{-2}	3.8×10^{-2}
$\frac{3}{4}$	7.0×10^{-2}	6.3×10^{-2}	4.4×10^{-2}

Table 10: Approximation for $\widehat{t}=t+\alpha^{(t)}$ when all schemes get third-order spatial accuracy near the boundaries.

$M_q^{(u)}$	MULI, MGULI	MDLI, MGDLI	MYLI,MGYLI	MR1, MCLI, CLI, BB
$\alpha^{(t)}$	$1-\delta_q$	δ_q	1	$\frac{1}{2}$

Λ_{eo} values, the distribution of the error along the period and several velocity profiles. The results confirm that for linear schemes the effective values of Λ_{eo} improve the accuracy at the boundary points, despite very high velocity gradients, and gain for the overall errors. For both slow and rapid oscillations the role of the effective Λ_{eo} value is especially important for $\delta_q\leq 1/2$ (we find this also in next experiment, see $\delta_q=1/10$). Let us stress that when the effective Λ_{eo} value increases with δ_q, so does the discretization errors in the bulk. This becomes noticeable for $T=25$ where a gain owing to Λ_{eo} becomes much less important for $\delta_q=1$ (see left top picture in Fig. 11). The relative error $L^2(u_x)$ has a sharp peak at the highest forcing ($t=0$ and $t=T/2$) in all computations.

Table 9 shows the results for $\delta_q^{(h)}=1$, $T=25$ when the parabolic schemes, MCLI, MR1 and MDLI model no-slip at the horizontal boundaries. The top right picture in Fig. 11 illustrates the error distribution along the period for $\Lambda_{eo}=3/4$. The results tell us that MCLI and especially MR1 still overhead CLI even for very high frequency but that MDLI (and therefore, MYLI($\delta_q^{(h)}=1$)) and CLI behave rather alike for $\delta_q^{(h)}=1$. As usual, the MR1 depends less than the other schemes on the selected Λ_{eo} value.

4.1.2 Time dependent velocity conditions (closed box)

We prescribe the exact profile for the vertical boundaries:

$$u_x(x=\pm l_x)=u_x^{(w)}(x,\widehat{t}),\quad u_y=0$$

and the no-slip condition for the horizontal boundaries. The precision depends then on the value selected for $\widehat{t}$ via the $w_q^{(u)}(\vec{r}_{\mathrm{w}},\widehat{t})$. The theoretical estimates for $\widehat{t}=t+\alpha^{(t)}$ are given in Table 10, based on the analysis in [16]. We suggest that for linear schemes these estimates are efficient only when their second-order spatial error is removed with Λ_{eo}. In such a case, $\alpha^{(t)}$ has the same value for parabolic and linear schemes. Let us perform a series of experiments.

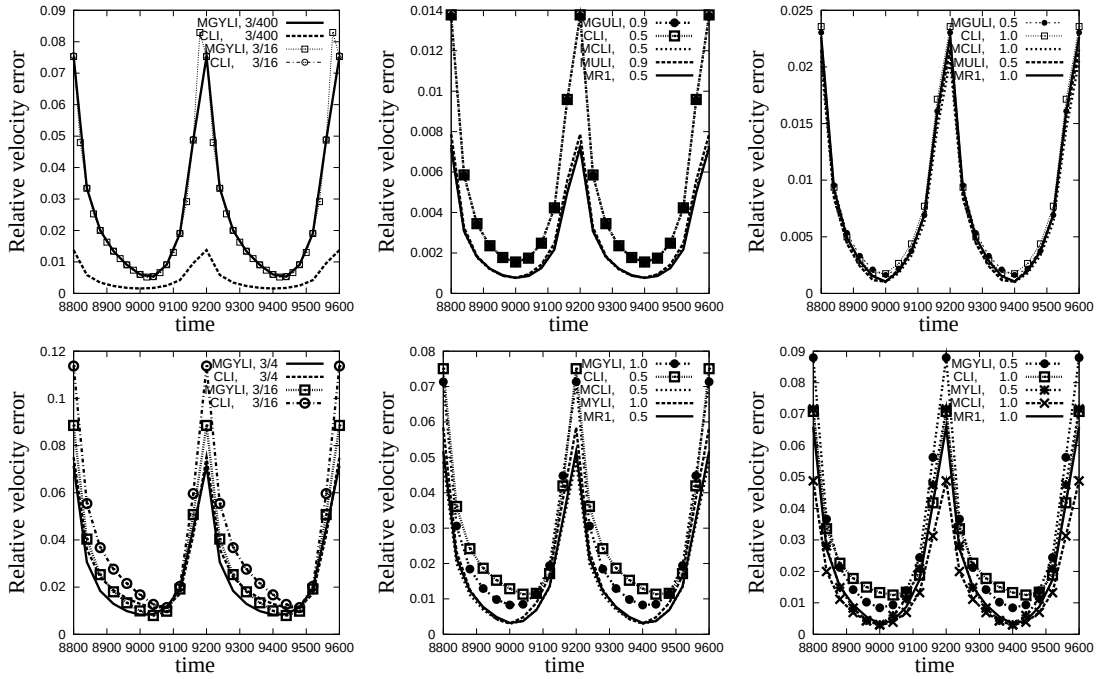

Figure 12: Test V, Experiment 3. Relative error $L^2(u_x)$ for Womersley-type solution along the period $T=800$. The computations are done with the Dirichlet velocity schemes for all boundaries on a 20^2 box. For both vertical and horizontal walls, $\delta_q=1/10$ (top row) and $\delta_q=1$ (bottom row). The effective solutions are $\Lambda_{eo}=3/400$ for $\delta_q=1/10$ and $\Lambda_{eo}=3/4$ for $\delta_q=1$. The legends give the values of Λ_{eo} (left column) and $\alpha^{(t)}$ (middle and right columns).

Experiment 3

All horizontal and vertical boundaries are shifted at the same distance,

$$\delta_q=\delta_q^{(h)}=\delta_q^{(v)},$$

which is set equal to $1/10$ and 1. We verify that the solution (2.22) still efficiently removes the second-order spatial error for both boundaries. The distribution of the error $L^2(u_x)$ is plotted in Fig. 12 for the case of $T=800$, $\mathrm{Wn}^2=12\pi$, $\nu=1/48$. The results shown in the left pictures confirm that the "magic" linear schemes CLI and MGYLI obtain a better precision with $\Lambda_{eo}=3/400$ (top picture) and $\Lambda_{eo}=3/4$ (bottom picture) , comparing to the "middle" value $\Lambda_{eo}=3/16$. This difference is most significant for the small distance, $\delta_q=1/10$: here, $\Lambda_{eo}=3/400$ gains by a factor 5 over $\Lambda_{eo}=3/16$. The experiment with $\delta_q=1/10$ is run with $\alpha^{(t)}=1/2$ for CLI and $\alpha^{(t)}=1$ for MGYLI, in agreement with Table 10. We emphasize that the solutions obtained with CLI and MGYLI are very similar for slow flow (we recall that they are identical at steady state).

Let us now verify the efficiency of $\alpha^{(t)}$ values. The results in the middle and right pictures of Fig. 12 are computed with $\Lambda_{eo}=\frac{3}{4}\delta_q^2$ for the linear schemes and $\Lambda_{eo}=3/16$ for the parabolic ones, less dependent on Λ_{eo}. The results in the middle column are

computed with the $\alpha^{(t)}$ value given in Table 10. We select then an alternative value for the computations in the right column: $\alpha^{(t)}=1$ for {CLI,MCLI,MR1} and $\alpha^{(t)}=1/2$ for {MGYLI,MGULI,MYLI,MULI}. In all computations, the effective $\alpha^{(t)}$ value gains in accuracy and the parabolic schemes are more accurate then the linear ones, especially for $\delta_q=1/10$. In the right pictures, the second-order spatial and time errors are coupled and all schemes behave rather alike. It is noted that when using $\Lambda_{eo}=3/16$ the error also decreases for all schemes when $\delta_q=1$, most probably because of the larger spatial/mixed discretization errors. The second-type links are treated here with MGULI. We find again that CLI works more robustly in combination with MGULI/MGDLI for second-type links when $\delta_q^{(h)}\to 0$. Applied at all four boundaries, MR1 losses here stability for $\delta_q=1$. The results for $\delta_q=1$ are computed with MR1 at the vertical boundaries and MCLI at the horizontal walls. The MGMR(C) with $C\neq 0$ behaves more robustly but less accurately than MR1.

Altogether this experiment validates the efficiency of the estimates in Table 10 and indicates that a proper selection of $\widehat{t}$ is especially important when the walls are located close to the grid nodes and the spatial errors have been efficiently reduced.

Experiment 4

We fix now the horizontal walls at $\delta_q^{(h)}=1/2$ (using BB and $\Lambda_{eo}=3/16$) but place the vertical boundaries at $\delta_q^{(v)}=\{\frac{1}{10},\frac{1}{2},1\}$. The results are presented in Fig. 13. We study two principal cases: $\alpha^{(t)}=1/2$ and $\alpha^{(t)}=1$. In the left pictures, the parameter $\alpha^{(t)}$ takes approximately the values from Table 10, e.g. $\alpha^{(t)}=1/2$ for MR1 and MCLI and $\alpha^{(t)}=1$ for MYLI and MULI when $\delta_q^{(v)}=1/10$. The pictures in the right column are computed with another $\alpha^{(t)}$ value. The second-type links are treated with CLI=BB for the horizontal boundaries and MGULI/MGDLI for the vertical boundaries. The linear schemes, MGYLI and CLI lose accuracy for $\delta_q^{(v)}=1/10$ and $\delta_q^{(v)}=1$ because of the inefficiency of $\Lambda_{eo}=3/16$ for these distances, but they regain it for $\delta_q^{(v)}=1/2$. The accuracy of all parabolic schemes is very similar when $\delta_q^{(v)}=1/10$ (top row pictures). When $\alpha^{(t)}$ values are exchanged, the error increases with a factor 2 for all schemes. It is noted that MR1, MCLI (and even CLI and MGYLI in the right column) clearly overhead MYLI for $\delta_q^{(v)}\geq 1/2$, similarly as in Experiment 2. We suggest that truncation spatial errors are smaller for MCLI, compared to MULI or MYLI, when $\delta_q>1/2$.

Altogether we find that MR1 and MCLI have the best accuracy depending less on the distance $\delta_q^{(v)}$. We suggest to use $\alpha^{(t)}=1/2$ for MR1 and $\alpha^{(t)}=1$ for MULI and MYLI and their second-order analogs for all distances. For MCLI and CLI, $\alpha^{(t)}=1/2$ works noticeably better than $\alpha^{(t)}=1$ only for small distances, then the difference between the two is less significant. The temporal Couette flow and Taylor vortex flow modeled with Dirichlet velocity conditions lead us to very similar conclusions. We find that the pulsatile flow represents a more efficient test for time dependent boundary conditions since the solution is independent of the initial distributions.

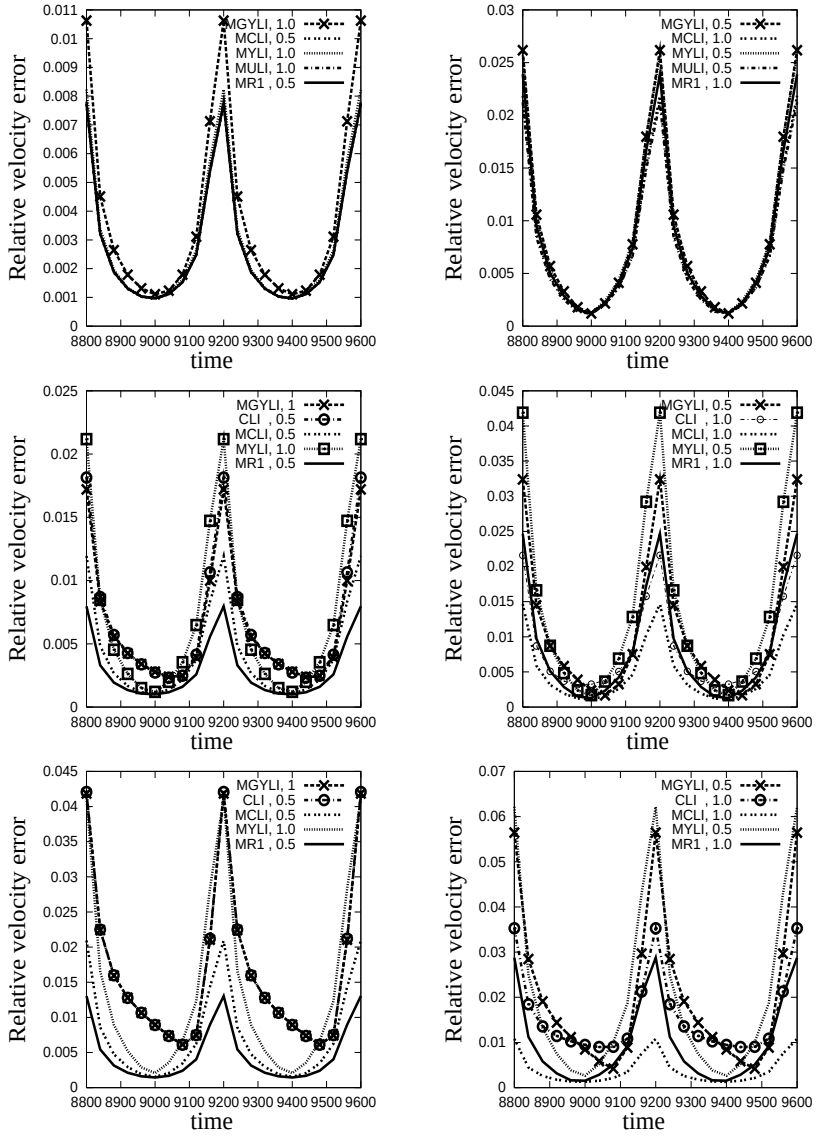

Figure 13: Test V, Experiment 4. The computations are similar to the ones on the previous picture but the horizontal walls are placed halfway the link. The distance $\delta_q^{(v)}$ to the vertical boundaries varies. Top row: $\delta_q^{(v)}=1/10$. Middle row: $\delta_q^{(v)}=1/2$. Bottom row: $\delta_q^{(v)}=1$. The prescribed values of $\alpha^{(t)}$ ($\alpha^{(t)}=1/20$ or $\alpha^{(t)}=1$) are given in the legends.

4.1.3 Periodic, velocity and mixed conditions

Experiment 5

We compare the solutions obtained with the Dirichlet velocity and mixed conditions on the vertical boundaries ($P(x=\pm l_x)=const$, $u_y=0$) to the open channel solutions, using

Table 11: Mean error $L^{2T}(u_x)$ for the Womersley-type flow at $\mathrm{Wn}^2=12\pi$, using the periodic, Dirichlet velocity and mixed conditions at the vertical boundaries. First three columns correspond to forcing driven flow, two last columns address the modeling without forcing.

		with forcing			without forcing	
ν	T	periodic	velocity	mixed	velocity	mixed
$\frac{1}{96}$	1600	4.49×10^{-3}	6.34×10^{-3}	5.16×10^{-3}	5.8×10^{-3}	6.3×10^{-3}
$\frac{1}{48}$	800	4.49×10^{-3}	6.3×10^{-3}	5.08×10^{-3}	8.2×10^{-3}	1.3×10^{-2}
$\frac{1}{24}$	400	4.06×10^{-3}	6.2×10^{-3}	4.7×10^{-3}	2.9×10^{-2}	5.1×10^{-2}
$\frac{1}{12}$	200	2.4×10^{-3}	5.2×10^{-3}	5.1×10^{-3}	1.4×10^{-1}	2.3×10^{-1}
$\frac{1}{6}$	100	4.4×10^{-3}	8.4×10^{-3}	3.4×10^{-3}	1.09	1.8
$\frac{1}{3}$	50	3.5×10^{-2}	3.9×10^{-2}	3.5×10^{-2}		
$\frac{2}{3}$	25	1.6×10^{-1}	1.5×10^{-1}	1.64×10^{-1}		

forcing in all cases. The three first columns in Table 11 show the results obtained for $\mathrm{Wn}^2=12\pi$. They are computed on a fixed grid, $l_x=l_y=10$, and for an equal distance

$$\delta_q^{(h)}=\delta_q^{(v)}=\frac{1}{2},\quad \Lambda_{eo}=\frac{3}{16},$$

applying CLI=BB as the $M_q^{(u)}$ and PMR1 as $M_q^{(p)}$ for the mixed scheme.

The dimensional analysis [16] predicts that, in contrast to steady solutions, time-dependent non-dimensional solutions *at a given grid are not necessarily identical* when the hydrodynamic governing numbers (Womersley number here) and Λ_{eo} are fixed. In agreement with these predictions, $L^{2T}(u_x)$ in Table 11 differs even if Wn and Λ_{eo} are fixed. When the oscillation becomes slow ($T\to\infty$) then

$$L^{2T}(u_x)\to const,$$

in agreement with the dimensional analysis for steady flow. The order of the magnitude of the mean error is the same for the three type boundary conditions.

The solutions are illustrated in Fig. 14 for T=240, $\mathrm{Wn}^2\approx$34.6, $A=5\times10^{-4}$. The solution is plotted at the moment when the forcing reaches its highest and smallest values, $t=0$ and $t=T/4$, respectively, when the time-harmonic motion is attained. Except for the periodic channel, the pressure distribution is not constant and the vertical velocity is not zero. The obtained pressure distribution is centered with respect to the center of the box. The results tell us that the pressure fluctuation around zero is similar for both Dirichlet conditions. It is noted that using the Stokes equilibrium function the horizontal velocity varies linearly with the amplitude A for all boundary conditions (velocity error is then independent of A), but the pressure error increases linearly with A, i.e., with the forcing. The obtained vertical velocity is smaller for the mixed condition, except in the corners. The mixed condition is applied here for the ensemble of the links which bisect

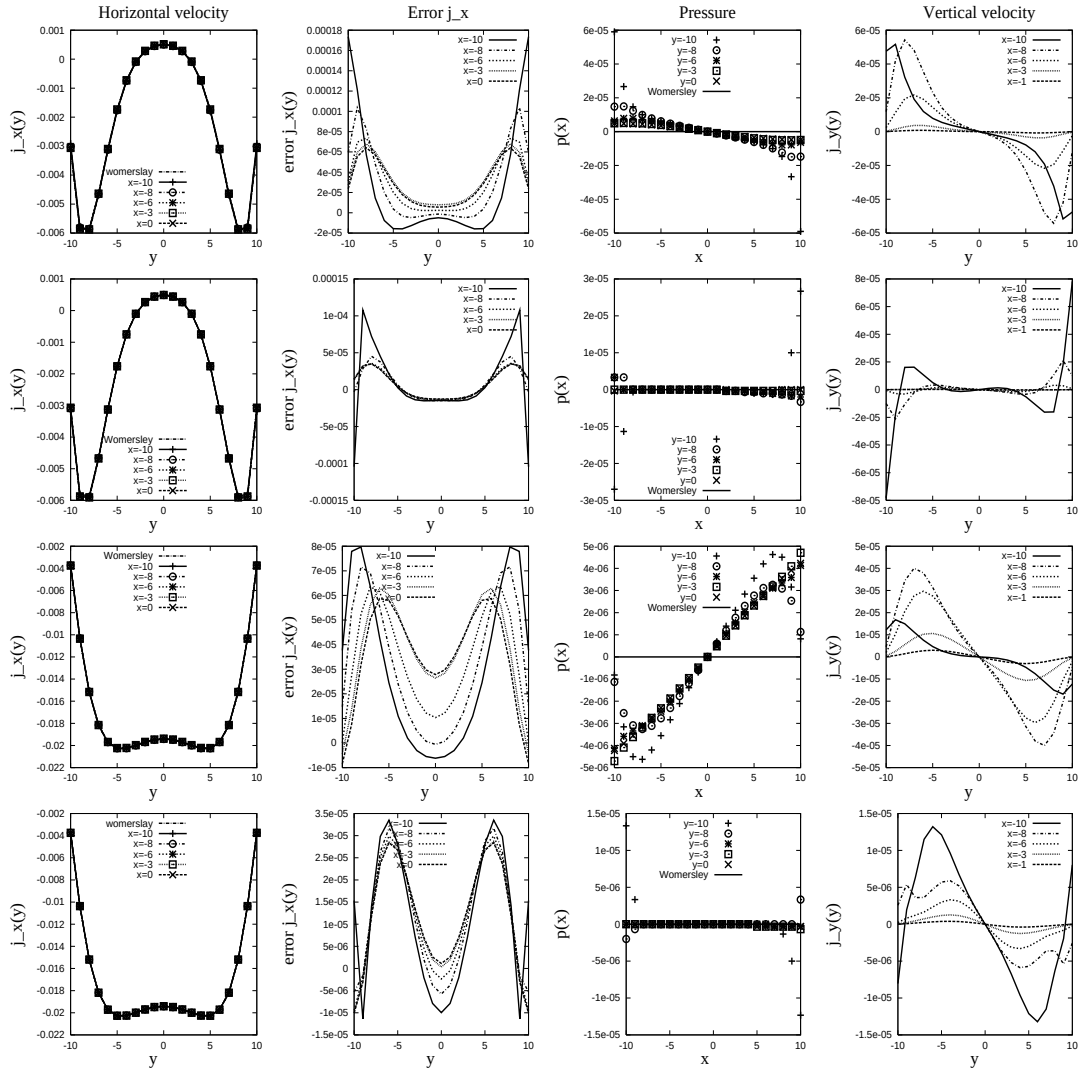

Figure 14: Test V, Experiment 5. Comparison of the LB pulsatile solutions obtained *with forcing* for $T=240$, $\mathrm{Wn}^2\approx 34.6$ with the Womersley-type solution $j_x^{(w)}$. Left to Right: $j_x(y)$, $j_x(y)-j_x^{(w)}(y)$, $p(x)$ and $j_z(y)$. Top and third row: $t=0$ and $t=T/4$, velocity conditions at the vertical boundaries. Second and bottom row: $t=0$ and $t=T/4$, mixed conditions at the vertical boundaries. The computations are done in a 21^2 box.

the vertical boundary. We have observed that when applying the no-slip condition for all links bisecting the horizontal boundary and only pressure conditions for the other corner links (as in all experiments above), the amplitude of the vertical velocity becomes higher in corners.

Altogether this numerical experiment confirms the applicability of the mixed scheme for time dependent flow with a prescribed constant pressure. Time dependent boundary conditions impose oscillating pressure drop in the next experiment.

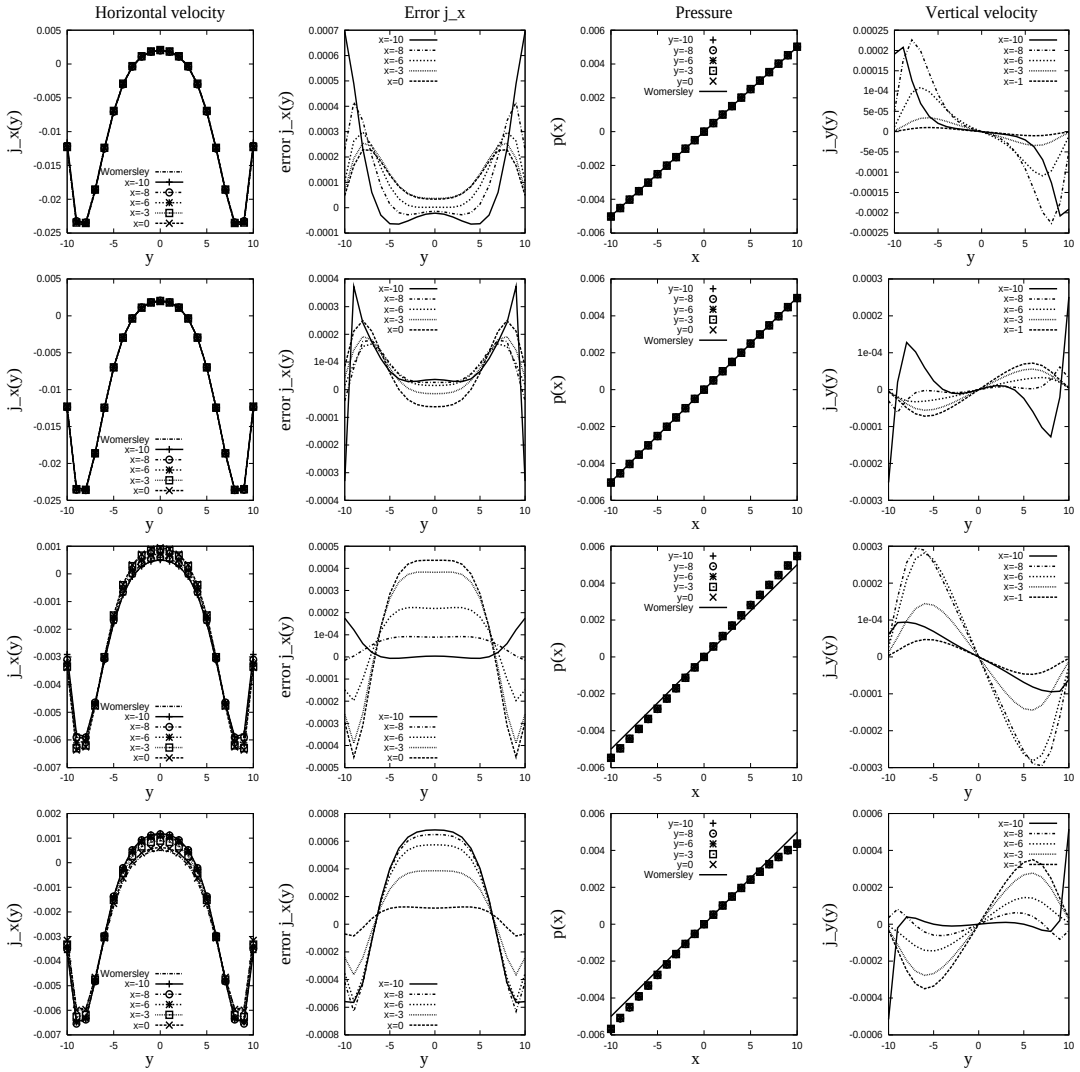

Figure 15: Test V, Experiment 6. The computations of the pulsatile flow *without forcing*, $t=0$. Top and third row: $T=960$ and $T=240$, velocity conditions at the vertical boundaries. Second and bottom row: $T=960$ and $T=240$, mixed conditions. The computations are done in a 21^2 box.

4.2 Modeling of pulsatile flow without forcing

Experiment 6

We consider simulations without forcing in a closed box applying the Dirichlet velocity and mixed boundary conditions to the vertical boundaries. The oscillating exact pressure solution is prescribed at the ends with the mixed condition via $w_q^{(p)}(\vec{r}_{\rm w},\widehat{t})$ in rela-

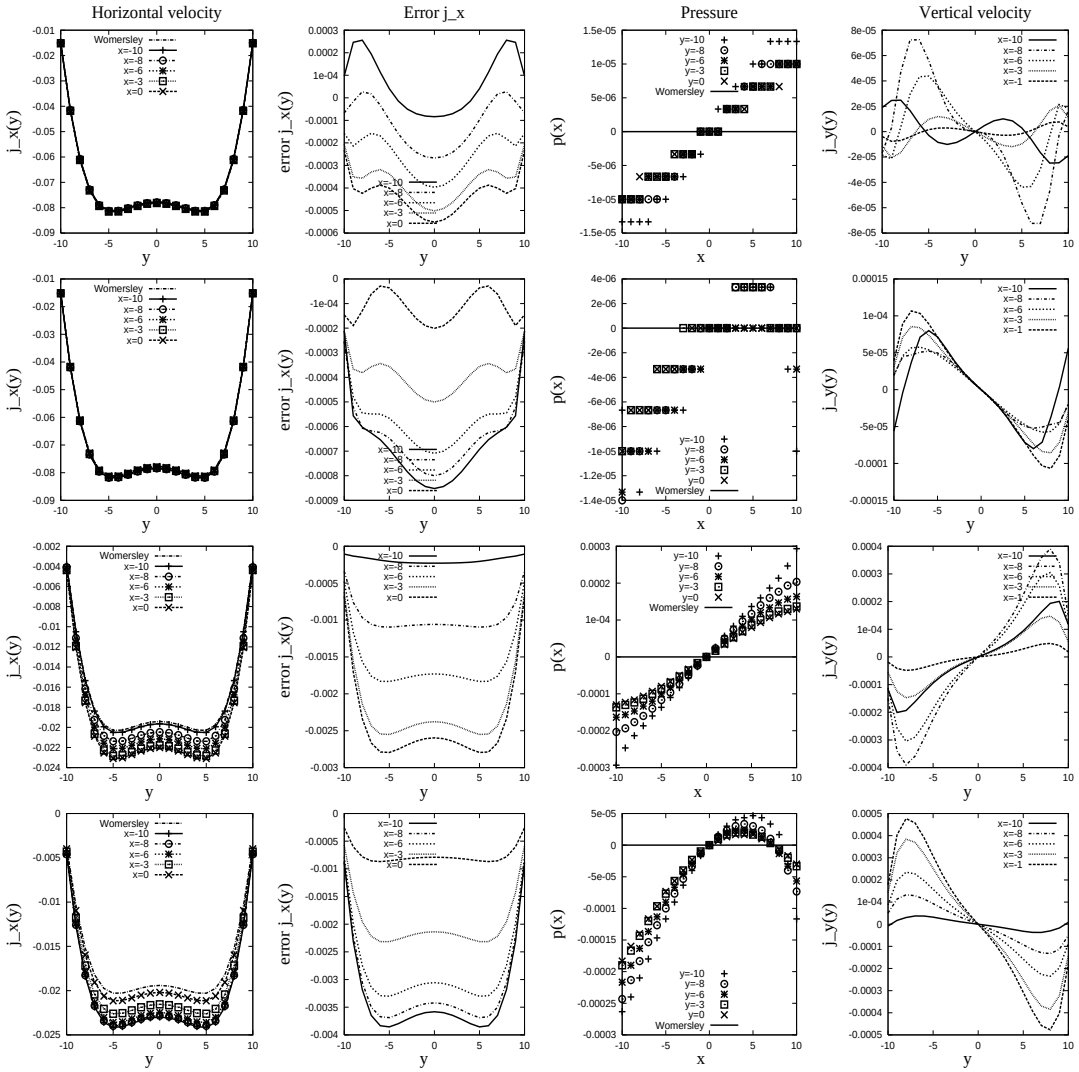

Figure 16: Same data as that of the previous picture at $t=T/4$.

tions (2.34). For the pressure schemes, a formal estimation for

$$\widehat{t}=t+\alpha^{(t)}$$

is presented in Table IX in [16]. It tells us that

$$\alpha^{(t)}=\frac{1}{2}+\Lambda_e(2+\delta_q)$$

for PMR1 (without taking into account second pressure gradient). We find that the obtained pressure solutions are a bit more accurate for $\alpha^{(t)}=1/2$ than for $\alpha^{(t)}=1$, at least

when $\Lambda_e \ll 1$ (i.e. for large T when the compressible effect is not significant). In this regime, obtained horizontal velocity varies linearly with the amplitude, but the relative pressure error increases again approximately linearly with A, for both Dirichlet conditions.

When the pressure varies in time, the obtained velocity field $\vec{j}$ becomes divergence free only in the limit $\omega \to 0$. The results in Table 11 and the pictures in Figs. 15, 16 show that the velocity and pressure distributions agree well with the incompressible solution for $T \geq 800$ (with a mean error below $\approx 1\%$). The deviation increases however very rapidly for faster oscillation. The results for $T=240$ in Figs. 15 and 16 can be compared to the ones plotted in the previous pictures, obtained with the forcing. In pressure driven flow, the horizontal velocity gets a dependence on x but, at the same time, the pressure is almost independent on y and still varies mainly along the x-axis.

Experiment 7

We continue the previous experiment for even more rapid pressure drop oscillations using the Dirichlet velocity conditions. They correspond to the incompressible exact solution. We are looking then for an analytical solution for the "acoustic" correction $\vec{j}^{(a)}(x,y,t)$, restricted to the no-slip boundary conditions at all ends:

$$\vec{j}^{(a)}(x=\pm l_x,y,t)=0, \quad \vec{j}^{(a)}(x,y=\pm l_y,t)=0. \tag{4.10}$$

We could construct only an approximative solution, $\vec{j}^{(c)}(x,y,t)$ and $P^{(c)}(x,t)$ here, to Eqs. (2.7) with the boundary conditions (4.10):

$$\begin{aligned} &\vec{j}^{(c)}(x,y,t)=\rho_0 \vec{u}^{(w)}(y,t)+\vec{j}^{(a)}(x,y,t), \\ &P^{(c)}(x,t)=P^{(w)}(x,t)+P^{(a)}(x,t). \end{aligned} \tag{4.11}$$

The idea of this solution is to keep $\nabla \cdot \vec{j}^{(c)}$ (and therefore, $P^{(c)}(t)$) independent of y. The solution for $j_x^{(a)}(x,y,t)$ has the form (B.8) with the coefficients (B.28)-(B.29). The principal vertical component $j_y^{(a,1)}(x,y,t)$ is given by relation (B.20). The pressure solution is then fixed with relations (B.18), (B.22). The solution (4.11) with the correction $j_x^{(a)}(x,y,t)$, $j_y^{(a,1)}(x,y,t)$ and $P^{(a)}(x,t)$ satisfies the compressible Stokes-type equations (2.7) and the prescribed Dirichlet conditions for the horizontal velocity. However, the second component of the vertical velocity, $j_y^{(a,2)}$, which we need to adjust the no-slip condition at the horizontal boundaries, satisfies the compressible Stokes equation only in the limit $\nu \to 0$. Based on a simple inspection (at the end of Appendix B), we suggest that the approximation approaches the solution for high Womersley numbers and, when Wn^2 is fixed, for smaller ν. In fact, the obtained solutions represent the linear combinations of the functions $r(Y,\mathrm{Wn}^2)$ and $p(Y,\mathrm{Wn}^2)$ (see Fig. 9), which vary only near the boundaries for high Womersley numbers.

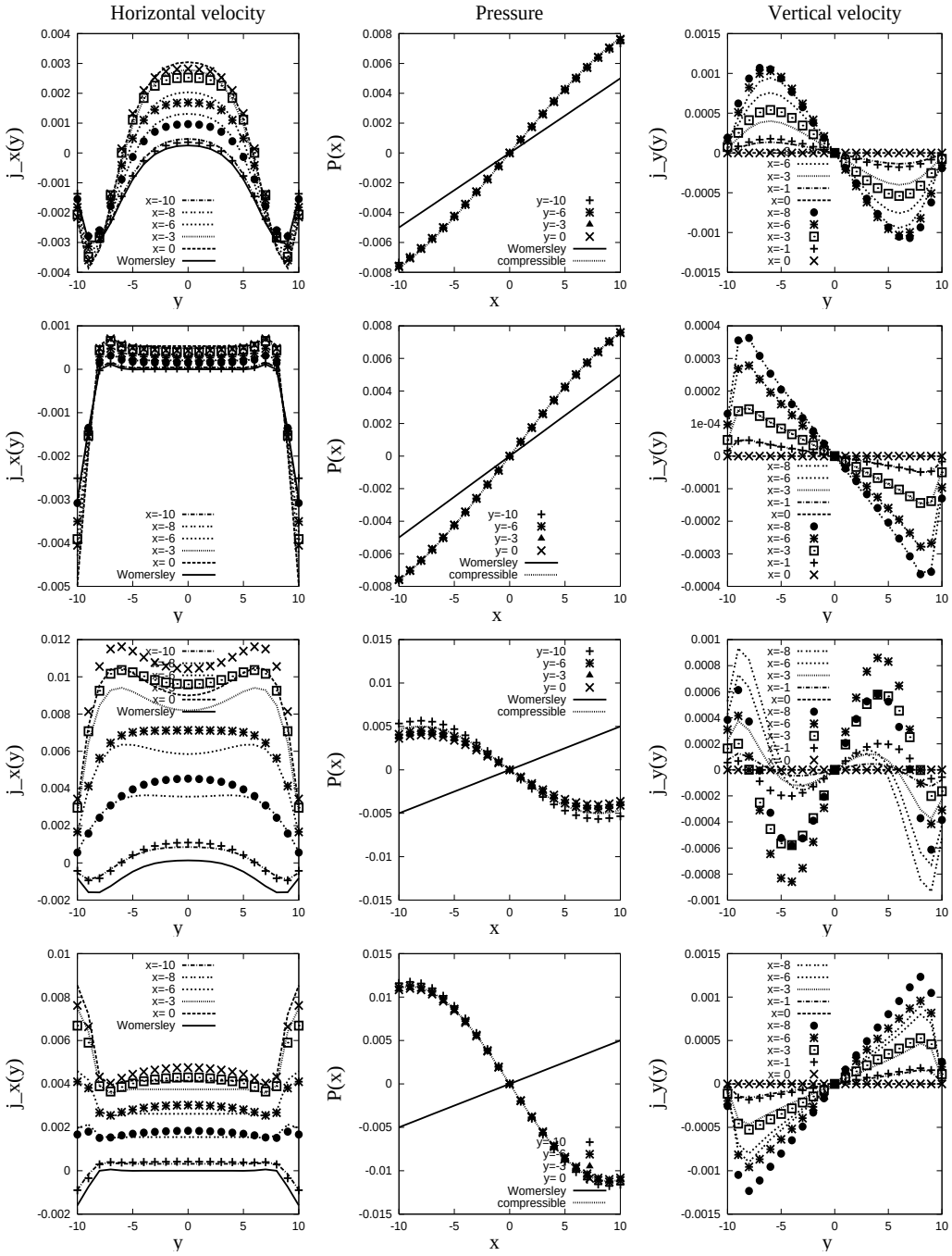

Figure 17: Test V, Experiment 7. Comparison of the LB pulsatile solutions without forcing (symbols) at $t=0$ to the Womersley-type solution (solid line) and to the approximated compressible solution (4.11) (dotted lines), using the Dirichlet velocity conditions at all boundaries. Top row: $T=120$, $\mathrm{Wn}^2\approx 34.6$. Second row: $T=120$, $\mathrm{Wn}^2\approx 346$. Third row: $T=64$, $\mathrm{Wn}^2\approx 34.6$. Bottom row: $T=64$, $\mathrm{Wn}^2\approx 346$. The computations are done in a 21^2 box.

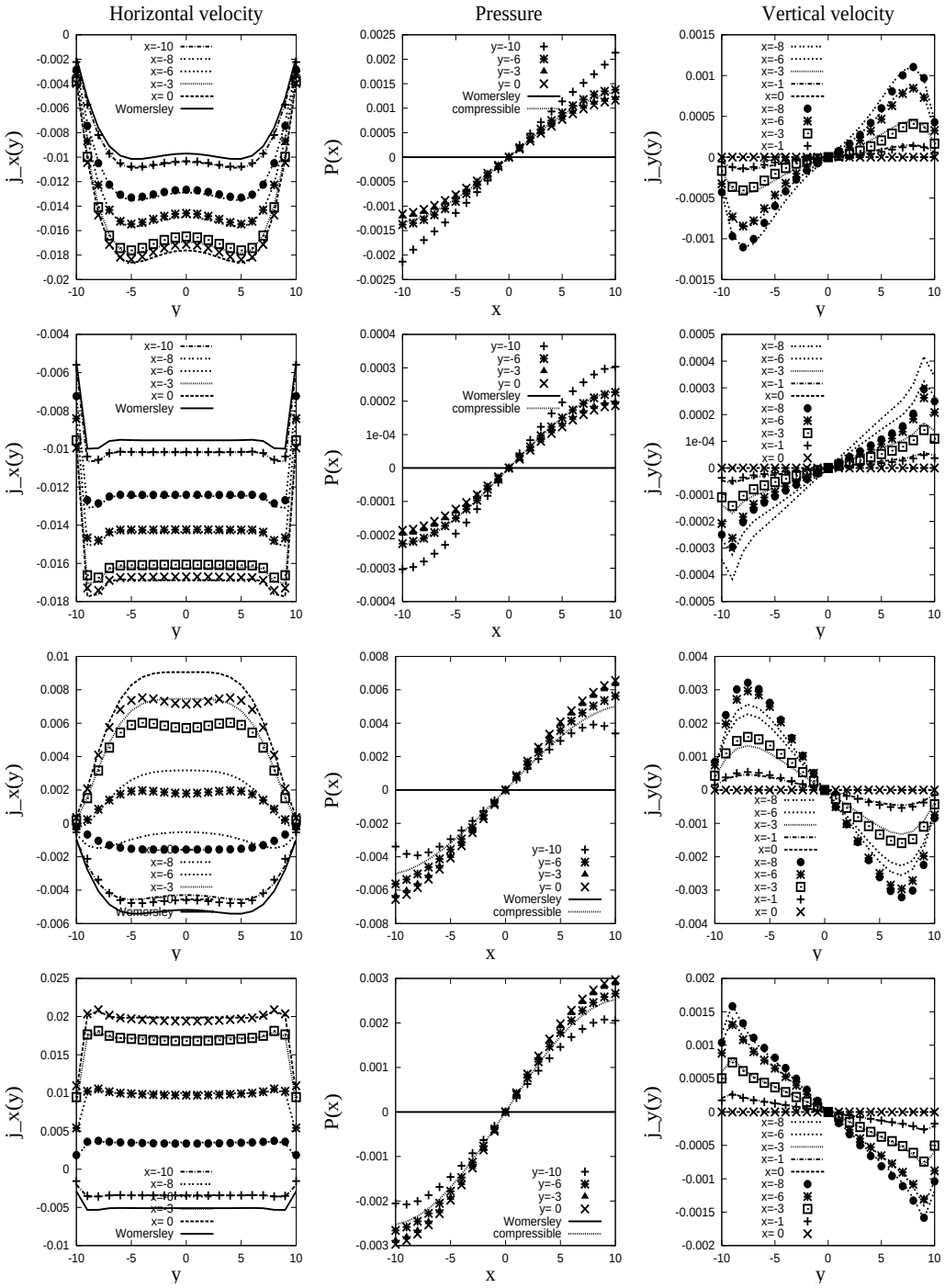

Figure 18: Same data as that of the previous picture at $t=T/4$.

Table 12: The L^2 error is computed with respect to the Womersley-type incompressible solution ($L^2(j_x^{(w)})$) and with respect to the compressible approximation (4.11) ($L^2(j_x^{(c)})$) and is shown for several samples in time. The results correspond to Fig. 17 for $t=0$ and Fig. 18 for $t=T/4$.

$T=120$	$\nu=\frac{1}{6}$, $\mathrm{Wn}^2=34.64$		$\nu=\frac{1}{60}$, $\mathrm{Wn}^2=346.4$		$\nu=\frac{1}{300}$, $\mathrm{Wn}^2=1732$	
t	$L^2(j_x^{(w)})$	$L^2(j_x^{(c)})$	$L^2(j_x^{(w)})$	$L^2(j_x^{(c)})$	$L^2(j_x^{(w)})$	$L^2(j_x^{(c)})$
0	0.81	0.12	0.38	0.18	0.34	0.55
$\frac{T}{8}$	0.42	0.019	0.5	0.021	0.51	0.084
$\frac{T}{4}$	0.59	0.018	0.54	0.012	0.52	0.046
$\frac{3T}{8}$	0.8	0.031	0.58	0.023	0.54	0.012
$T=64$	$\nu=0.3125$, $\mathrm{Wn}^2=34.64$		$\nu=0.03125$, $\mathrm{Wn}^2=346.4$		$\nu=0.00625$, $\mathrm{Wn}^2=1732$	
t	$L^2(j_x^{(w)})$	$L^2(j_x^{(c)})$	$L^2(j_x^{(w)})$	$L^2(j_x^{(c)})$	$L^2(j_x^{(w)})$	$L^2(j_x^{(c)})$
0	8.7	0.13	7.1	0.1	3.7	0.43
$\frac{T}{8}$	2.9	0.032	4	0.0095	3.8	0.087
$\frac{T}{4}$	1.6	0.19	3.4	0.023	3.7	0.042
$\frac{3T}{8}$	0.4	0.47	2.8	0.065	3.5	0.02

We show in Table 12 the relative $L^2(u_x)$ errors measured with respect to the incompressible solution (4.2) and with respect to the compressible approximation. These solutions are illustrated in Figs. 17 and 18. The approximation fits roughly but mainly correctly the amplitude of the obtained horizontal velocity and its variation along x axis. It gains about two orders of the magnitude for the velocity error in case $T=64$, $\mathrm{Wn}^2=346.4$ and $\mathrm{Wn}^2=1732$. The figures show that the obtained pressure solution fits the analytical prediction $P^{(c)}(x,t)$ surprisingly well, even when both velocity components are fitted very roughly (see pictures in two bottom rows in Fig. 17).

We recall that using the TRT model and $c_s^2=1/3$, both bulk and kinematic viscosities coincide. Using different c_s^2 values or the MRT model with distinct kinematic/bulk viscosity eigenvalues, one can investigate the role of the bulk viscosity in these solutions. Preliminary computations with the MRT model confirm that the constructed approximation works when the kinematic and bulk viscosity differ. We do not expect any significant impact of the compressible corrections in the population solution on the effective precision of the boundary scheme at first order. The obtained results confirm these assumptions. Indeed, the exact Womersley-type solution and the constructed approximation differ already at boundary nodes for compressible flow (see $x=10$ on the left pictures in Figs. 17 and 18). We observe that bounce-back localizes the horizontal velocity quite accurately with respect to the compressible solution (see symbols "+"), at least when $\delta_q^{(v)}=1/2$, $\Lambda_{eo}=3/16$, like for incompressible flow. At second-order, the incompressibility assumption was involved into the analysis and construction of the pressure and velocity boundary schemes. Detailed study of the parabolic $M_q^{(u)}$ schemes in the compressible regime is left to future work.

5 Concluding remarks

We have presented several multi-reflection algorithms for velocity and pressure boundary conditions and for their mixed combination. Numerical computations validate the Chapman-Enskog and the dimensional analysis [16], based on exact population solutions, in simple problems with an analytical solution. They show that highly accurate boundary schemes are needed in corners and for small resolutions, typically for flow through soil pores. A very similar performance can be achieved with the Dirichlet velocity and mixed schemes when they are based on the multi-reflection components which are equivalent in accuracy. Whereas an effective accuracy of "linear" schemes depends drastically on the choice of the "kinetic" collision components, this effect is strongly reduced for "parabolic" pressure and velocity schemes. We find that the MGMR(C) (and especially MR1) and MLI$(\alpha^{(u)})$ velocity families and the PMR1/PMR2 pressure schemes are superior in overall accuracy for steady and pulsatile flow. We expect that the developed boundary schemes work similarly in the frame of the TRT and MRT models in the incompressible regime, at least.

We emphasize that there is freedom in the selection of the coefficients for "linear" (three populations based, second-order accurate) and "parabolic" (five populations based, third-order accurate) schemes. Two representatives, the CLI and MR1 schemes yield an exact parametrization of the steady solutions with non-dimensional hydrodynamic numbers and Λ_{eo} but their coefficients lie at the limits of the heuristic stability intervals. The extension of MR1 to the MGMR(C) sub-family improves its stability properties. We also get an exact parametrization of the steady solutions for linear MGLI$(\alpha^{(u)})$ sub-family, with the help of a special local correction. This gives the chance to combine the best stability and parametrization properties as well as to avoid the development of the staggered invariants. We find that CLI in combination with MGULI/MGDLI and MGMR(C) in combination with MULI/MDLI/MCLI, e.g., in corners and/or adjacent boundaries, are the most robust.

We emphasize that the development of the accommodation layers reflects the "kinetic nature" of Lattice Boltzmann approach for boundary conditions. For one specific value, $\Lambda_{eo}=1/4$, the Knudsen layers should vanish in bulk points, at least for steady solutions. This value also yields distinct properties for the stability of the TRT operator (see [15]) but is not necessarily the most accurate. Linear schemes obtain exact parabolic solutions in a straight channel when $\Lambda_{eo}\in[0,\frac{3}{4}]$. Its smaller values reduce the discretization errors in the bulk and we suggest to choose Λ_{eo} inside the interval $[0,1]$. The Knudsen layers are caused by a mismatch between the incoming populations and their exact solution, expected from the bulk. One exact example, constructed in this paper, demonstrates that the accommodation may carry useful properties, both for robustness and accuracy. We show that the "parabolic" boundary conditions minimize the impact of the accommodation layers on the second-order terms in the population expansion and, therefore, on the derived hydrodynamic solutions.

A "Solid rotation" solution

This solution satisfies incompressible Navier-Stokes Eq. (2.5) with

$$\begin{aligned}&\vec{u}(x,y)=\vec{u}^{\tau}(r),\quad \vec{u}^{\tau}(r)=\Omega\vec{i_z}\otimes\vec{r},\quad \text{i.e. } u_x^{\tau}=-\Omega y,\quad u_y^{\tau}=\Omega x,\\&P(x,y)=P_0+\rho_0\frac{\Omega^2r^2}{2},\quad r^2=x^2+y^2.\end{aligned}\tag{A.1}$$

Using the equilibrium distribution (2.3) with $g_S=1$, yields:

$$\begin{aligned}u_q(x,y)&=-yc_{qx}+xc_{qy}=(-y-c_{qy})c_{qx}+(x+c_{qx})c_{qy}\\&=u_q(x+c_{qx},y+c_{qy}),\\t_q^{\star}(P+E_q^{+}(\vec{u},\rho_0)&=t_q^{\star}(\frac{3}{2}\rho_0u_q^2+P_0),\quad \forall\, q=0,\cdots,Q-1.\end{aligned}\tag{A.2}$$

Substituting the first condition into the second one, one gets

$$e_q^{\pm}(x+c_{qx},y+c_{qy})=e_q^{\pm}(x,y),$$

then

$$f_q^{\pm}(x,y)=e_q^{\pm}(x,y),\quad p_q\equiv0,\quad m_q\equiv0,\quad \forall\,\{x,y\},\,\forall q.\tag{A.3}$$

The solution is therefore constant along any link and equal to the local equilibrium value. Any link-wise ($j^{(1)}/\Pi^{(1)}$-accurate) boundary scheme, e.g., all $M_q^{(u)}$ schemes, will support it exactly for any shape of boundary. When the mixed boundary conditions are applied, all $M_q^{(m)}$ pressure schemes support this solution exactly in a static coordinate system.

In the moving coordinate system $\vec{u}^{m}(r)=\vec{u}(r)-\vec{u}^{\tau}(r)$, the velocity is equal to zero, $\vec{u}(x,y)=\vec{u}^{b}\equiv0$, and the solution (A.1) can be obtained with the help of the centrifugal force:

$$\vec{F}(x,y)=\rho_0\Omega^2\vec{r},\quad \nabla P=\vec{F}.\tag{A.4}$$

Using, e.g., the momentum conserving equilibrium ($\vec{j}^{\rm eq}=\vec{J}=\vec{j}-\frac{1}{2}\vec{F}$ with $\vec{j}=0$), the exact population solution is

$$\begin{aligned}&e_q^{-}=-\frac{1}{2}F_q^{\star},\quad e_q^{+}=\Pi_q^{\star},\\&m_q^{ch}=(\partial_q\Pi_q^{\star}-F_q^{\star})=0,\quad p_q^{ch}=-\partial_q\Lambda_o(\partial_q\Pi_q^{\star}-F_q^{\star})=0.\end{aligned}\tag{A.5}$$

Although the solution remains at equilibrium, the equilibrium itself varies along the link. Velocity schemes maintain this solution if $\beta^{(p)}=-\alpha^{(u)}\Lambda_o$ or when $\partial_q\Pi_q^{\star}$ and $-F_q^{\star}$ have equal coefficients in closure relation. The solution is then supported by MGLI($\alpha^{(u)}$), MLI($\alpha^{(u)}$), MR1 and MGMR(C) schemes, but not by ULI/DLI/YLI. The Dirichlet pressure closure relation must fit exactly $\mathcal{O}(\partial_q^2\Pi_q^{\star})/\mathcal{O}(\partial_qF_q^{\star})$. The pressure schemes remove the forcing and its gradient from their closure relation. Then the $\Pi^{(3)}$-accurate schemes can maintain the exact parabolic pressure solution, e.g., PMR2. The mixed $M_q^{(m)}$ scheme maintains the exact solution when both components, $M_q^{(u)}$ and $M_q^{(p)}$, are exact.

B Approximate solutions for compressible pulsatile flow

We set $\rho_0=1$ and looking for the solution $\{\vec{j}=(j_x,j_y),P\}$ in a rectangular $2d$ domain (x,y), $x\in[-l_x,l_x]$, $y\in[-l_y,l_y]$, which satisfies the compressible, Stokes-type equation:

$$\partial_t P+c_s^2\nabla\cdot\vec{j}=0, \tag{B.1}$$

$$\partial_t\vec{j}+\nabla P=\nu\Delta\vec{j}+\nu_\xi\nabla\nabla\cdot\vec{j}. \tag{B.2}$$

Here c_s^2 is the sound velocity, ν is the kinematic viscosity, ν_ξ is the bulk viscosity, $\nabla\phi=(\partial_x\phi,\partial_y\phi)$, $\nabla\cdot\phi=\partial_x\phi+\partial_y\phi$, and $\Delta\phi$ is the Laplace operator, $\Delta\phi=\partial_x^2\phi+\partial_y^2\phi$, $\forall\,\phi(x,y)$. Let mean density of the incompressible flow be ρ_0. We are interested to solve Eqs. (B.1)- (B.2) with the following Dirichlet boundary conditions:

$$\vec{j}(x,y=\pm l_y)=0,\quad \vec{j}(x=\pm l_x,y,t)=\vec{j}^{(w)}(y,t), \tag{B.3}$$

where

$$\vec{j}^{(w)}(y,t)=\{\rho_0 u_x^{(w)}(y,t),0\}$$

is the solution (4.2)-(4.4) for the incompressible Womersley flow [43]. We are looking for the deviation to the Womersley solution, $P^{(a)}(x,y,t)$ and $\vec{j}^{(a)}(x,y,t)$:

$$\vec{j}(x,y,t)=\vec{j}^{(w)}(y,t)+\vec{j}^{(a)}(x,y,t),\quad P=P^{(w)}(x,t)+P^{(a)}(x,y,t). \tag{B.4}$$

They should satisfy the following equations and the no-slip boundary conditions:

$$\partial_t P^{(a)}+c_s^2\nabla\cdot\vec{j}^{(a)}=-\partial_t P^{(w)}, \tag{B.5}$$

$$\partial_t\vec{j}^{(a)}+\nabla P^{(a)}=\nu\Delta\vec{j}^{(a)}+\nu_\xi\nabla\nabla\cdot\vec{j}^{(a)}, \tag{B.6}$$

$$\vec{j}^{(a)}(x=\pm l_x,y,t)=0,\quad \vec{j}^{(a)}(x,y=\pm l_y,t)=0. \tag{B.7}$$

B.1 Approximation 1

We consider 1D solution $\vec{j}^{(a)}=(j_x^{(a)},0)$, where $j_x^{(a)}(x,y,t)$ is presented in the form:

$$\begin{aligned}
&j_x^{(a)}(x,y,t)=j_x^{(a,1)}(X,Y,t)+j_x^{(a,2)}(X,t),\quad Y=\frac{Y}{l_y},\quad X=\frac{x}{l_x},\\
&j_x^{(a,1)}(X,Y,t)=\sum_{k\geq 1}\cos(k_x l_x X)(D_k u_w(Y,t)+C_k u_c(Y,t)),\quad k_x=\frac{k\pi}{2l_x},\\
&j_x^{(a,2)}(X,t)=-j_x^{(a,1)}(X,\pm 1,t),
\end{aligned} \tag{B.8}$$

with

$$\begin{aligned}
u_w(Y,t)&=r(k',k'',Y)\cos(\omega t)+p(k',k'',Y)\sin(\omega t),\\
u_c(Y,t)&=-p(k',k'',Y)\cos(\omega t)+r(k',k'',Y)\sin(\omega t).
\end{aligned} \tag{B.9}$$

The solution (B.8)-(B.9) should obey the no-slip conditions:

$$j_x^{(a)}(x=\pm l_x,y,t)=0,\quad j_x^{(a)}(x,y=\pm l_y,t)=0. \tag{B.10}$$

We substitute the x-derivative of the continuity equation (B.5),

$$\partial_t\partial_x P^{(a)}=-c_s^2(\partial_x^2 j_x^{(a,1)}+\partial_x^2 j_x^{(a,2)})-\partial_t\partial_x P^{(w)} \tag{B.11}$$

into the time derivative of the Stokes equation (B.6):

$$\partial_t^2 j_x^{(a,1)}=\nu(\partial_t\partial_x^2 j_x^{(a,1)}+\partial_t\partial_y^2 j_x^{(a,1)})+c_s^2\partial_x^2 j_x^{(a,1)}+\nu_\xi\partial_t\partial_x^2 j_x^{(a,1)}, \tag{B.12}$$

$$\partial_t^2 j_x^{(a,2)}=\nu\partial_t\partial_x^2 j_x^{(a,2)}+c_s^2\partial_x^2 j_x^{(a,2)}+\nu_\xi\partial_t\partial_x^2 j_x^{(a,2)}+\partial_t\partial_x P^{(w)}. \tag{B.13}$$

Using then the Fourier series to represent a constant impulse $\partial_t\partial_x P^{(w)}=-Aw\cos(\omega t)$:

$$\partial_t\partial_x P^{(w)}=-4A\omega\sin(\omega t)\sum_{k\geq 1}\cos(k_x l_x X)\frac{\sin(\frac{\pi k}{2})}{\pi k}, \tag{B.14}$$

and substituting relation (B.8), we obtain the solution for k', k'' from Eq. (B.12) and for $\{C_k,D_k\}$ from Eq. (B.13). The solution for k' and k'' is:

$$\begin{aligned} &k'=\frac{-l_y}{\sqrt{2\nu\omega}}\sqrt{d_0-d_1},\quad k''=\frac{l_y}{\sqrt{2\nu\omega}}\sqrt{d_0+d_1},\\ &d_1=\omega k_x^2(\nu+\nu_\xi),\quad d_2=c_s^2k_x^2-\omega^2,\quad d_0=\sqrt{d_1^2+d_2^2}. \end{aligned} \tag{B.15}$$

The solution (B.15) reduces to incompressible solution (4.4) when $k_x\equiv 0$. The solution for $\{C_k,D_k\}$ is:

$$C_k=-4A\omega\frac{d_1}{d_0}\frac{\sin(\frac{\pi k}{2})}{\pi k},\quad D_k=-4A\omega\frac{d_2}{d_0}\frac{\sin(\frac{\pi k}{2})}{\pi k}. \tag{B.16}$$

The obtained solution verifies Stokes equation (B.6) and the boundary conditions (B.7) but there exist a non-zero gradient $\partial_y P^{(a)}$. The Stokes equation is therefore violated for the vertical velocity component. The one-dimensional approximation gives then only a very qualitative approximation of the obtained numerical solution.

B.2 Approximation 2

The numerical computations suggest that a reasonable approximation is to keep $P^{(a)}$ as independent from y, at least away from the boundaries. Let us represent $P^{(a)}$ as:

$$P^{(a)}(x,y,t)=P^{(a)}(x,t)+P^{(a)}(y,t)+\delta P^{(a)}(x,y,t), \tag{B.17}$$

and drop first $P^{(a)}(y,t)$ and $\delta P^{(a)}(x,y,t)$. We present the $2d$ solution as:

$$\begin{aligned}
&\partial_t P^{(a)} = -(c_s^2\Psi(X,t)+\partial_t P^{(w)}),\\
&j_x^{(a)}(x,y,t) = j_x^{(a,1)}(X,Y,t)+j_x^{(a,2)}(X,t),\\
&j_y^{(a)}(x,y,t) = j_y^{(a,1)}(X,Y,t)+j_y^{(a,2)}(X,Y,t),\\
&\partial_x j_x^{(a,1)}+\partial_y j_y^{(a,1)} = 0, \quad \partial_x j_x^{(a,2)}+\partial_y j_y^{(a,2)} = \Psi(X,t),\\
&j_x^{(a,2)}(X,t) = -j_x^{(a,1)}(X,\pm 1,t),\\
&j_y^{(a,2)}(X,\pm 1,t) = -j_y^{(a,1)}(X,\pm 1,t).
\end{aligned} \tag{B.18}$$

Assuming the boundary conditions (B.7), $\vec{j}^{(a)}$ should vanish also at the $x-$bounds:

$$j_x^{(a)}(\pm l_x,y,t) = 0, \quad j_y^{(a)}(\pm l_x,y,t) = 0. \tag{B.19}$$

Relations (B.18) yield for $j_y^{(a,1)}$ and $j_y^{(a,2)}$:

$$j_y^{(a,1)}(X,Y,t) = -I(X,Y,t), \quad I = l_y\int^Y \partial_x j_x^{(a,1)}(X,Y',t)dY', \tag{B.20}$$

$$j_y^{(a,2)}(X,Y,t) = l_y(\Psi(X,t)-\partial_x j_x^{(a,2)}(X,t))Y, \tag{B.21}$$

then

$$\Psi(X,t) = \partial_x j_x^{(a,2)}(X,t)-\frac{1}{l_y}j_y^{(a,1)}(X,1,t), \tag{B.22}$$

namely,

$$j_y^{(a,2)}(X,Y,t) = -j_y^{(a,1)}(X,1,t)Y. \tag{B.23}$$

The last relation of (B.18) was used to derive relation (B.22) from relation (B.21). Keeping the form (B.8) for $j_x^{(a,1)}$ and $j_x^{(a,2)}$, we can satisfy with help of k', k'', C_k and D_k the following equations:

$$\partial_t P^{(a)}+c_s^2\Psi = -\partial_t P^{(w)}, \tag{B.24}$$

$$\partial_t^2 j_x^{(a,1)} = \nu(\partial_t\partial_x^2 j_x^{(a,1)}+\partial_t\partial_y^2 j_x^{(a,1)}), \tag{B.25}$$

$$\partial_t^2 j_y^{(a,1)} = \nu(\partial_t\partial_x^2 j_y^{(a,1)}+\partial_t\partial_y^2 j_y^{(a,1)}), \tag{B.26}$$

$$\partial_t^2 j_x^{(a,2)} = \nu\partial_t\partial_x^2 j_x^{(a,2)}+c_s^2\partial_x\Psi+\nu_\xi\partial_t\partial_x\Psi+\partial_t\partial_x P^{(w)}, \tag{B.27}$$

where

$$j_y^{(a,1)} = -l_y\int^Y \partial_x j_x^{(a,1)}(X,Y',t)dY',$$

and hence $j_y^{(a,1)}$ satisfies Eq. (B.26) provided that $j_x^{(a,1)}$ satisfies Eq. (B.25). The solution to Eq. (B.25) is:

$$\begin{aligned} k' &= -\frac{1}{\sqrt{2}}\sqrt{-k_x^2 {l_y}^2+\sqrt{(k_x^2 {l_y}^2)^2+\mathrm{Wn}^4}}, \\ k'' &= \frac{1}{\sqrt{2}}\sqrt{k_x^2 {l_y}^2+\sqrt{(k_x^2 {l_y}^2)^2+\mathrm{Wn}^4}}, \quad \mathrm{Wn}^2=\frac{l_y^2\omega}{\nu}. \end{aligned} \tag{B.28}$$

Using again the Fourier series (B.14), Eq. (B.27) is satisfied when $\{C_k, D_k\}$ obey the following linear equations:

$$\begin{aligned} &a_k C_k + b_k D_k = 0, \\ &b_k C_k - a_k D_k = -4Aw\frac{\sin(\frac{\pi k}{2})}{\pi k}, \quad \forall k \geq 1, \end{aligned}$$

where

$$\begin{aligned} &a_k = d_2 - (d_4\sin(2k') - d_3\sinh(2k'')), \\ &b_k = -d_1 + (d_3\sin(2k') + d_4\sinh(2k'')), \\ &d_1 = \omega k_x^2(\nu+\nu_\xi), \quad d_2 = c_s^2 k_x^2 - \omega^2, \\ &d_3 = k_x^2\gamma'(k'\omega\nu_\xi - c_s^2 k''), \quad d_4 = k_x^2\gamma'(k''\omega\nu_\xi + c_s^2 k'), \\ &\gamma' = \frac{1}{\gamma(k'^2+k''^2)}, \quad \gamma = \cos(2k') + \cosh(2k''). \end{aligned} \tag{B.29}$$

The solution (B.20)-(B.23) becomes

$$\begin{aligned} j_y^{(a,1)}(X,Y,t) &= 2\sum_{k\geq 1}\sin(k_x l_x X) j_{y,k}^{(a,1)}(Y,t), \\ j_{y,k}^{(a,1)}(Y,t) &= \cos(\omega t)(h_k\cosh(k''Y)\sin(k'Y) + g_k\cos(k'Y)\sinh(k''Y)) \\ &\quad -\sin(\omega t)(h_k\cos(k'Y)\sinh(k''Y) - g_k\cosh(k''Y)\sin(k'Y)), \\ j_y^{(a,2)}(X,Y,t) &= -j_y^{(a,1)}(X,1,t)Y = -Y\sum_{k\geq 1}\sin(k_x l_x X) j_{y,k}^{(a,2)}(t), \\ j_{y,k}^{(a,2)}(t) &= \cos(\omega t)(e_k^-\sinh(2k'') - e_k^+\sin(2k')) \\ &\quad +\sin(\omega t)(e_k^-\sin(2k'') + e_k^+\sinh(2k'')), \end{aligned} \tag{B.30, B.31}$$

where

$$\begin{aligned} &h_k = e_k^-\sin(k')\sinh(k'') - e_k^+\cos(k')\cosh(k''), \\ &g_k = e_k^-\cos(k')\cosh(k'') + e_k^+\sin(k')\sinh(k''), \\ &e_k^+ = l_y\gamma' k_x(C_k k' + D_k k''), \quad e_k^- = l_y\gamma' k_x(D_k k' - C_k k''). \end{aligned} \tag{B.32}$$

When $\omega \to 0$, the coefficients C_k and D_k vanish and so does the compressible correction $\{P^{(a)}, \vec{j}^{(a)}\}$. The constructed solution (B.8) with the parameters (B.28)-(B.29) satisfies Stokes Eqs. (B.25)-(B.27) for $j_x^{(a)}$. These equations are independent from $\partial_y P^{(a)}(Y,t)$. The principal vertical component $j_y^{(a,1)}$ satisfies the Stokes Eq. (B.26) but not the second component

$$j_y^{(a,2)} = -j_y^{(a,1)}(Y=1)Y,$$

which we need to adjust the no-slip conditions on the horizontal boundaries. Besides that $j_y^{(a)}(\pm 1, Y, t)$, being proportional to $\sin[\frac{k\pi}{2}X]$ by the construction, can not satisfy the no-slip conditions at x ends. Let us analyze if the constructed solution could nevertheless represent a suitable approximation to Eqs. (B.5)- (B.7).

The deviation from Stokes equation (B.6) (keeping $\partial_y P^{(a)} = 0$) is:

$$\begin{aligned} err(j_y^{(a,2)}) &= \partial_t j_y^{(a,2)} - \nu \partial_x^2 j_y^{(a,2)} \\ &= -Y([\partial_t j_y^{(a,1)} - \nu \partial_x^2 j_y^{(a,1)}]|_{Y=1}) \\ &= -Y\nu \partial_y^2 j_y^{(a,1)}(X,1,t). \end{aligned} \tag{B.33}$$

It is noted that $err(j_y^{(a,2)})$ vanishes when $Y=0, \forall X$ and when $X=0, \forall Y$, i.e., the constructed solution (B.8) with (B.28)-(B.29) satisfies the problem on the axis. We find then that the highest error, which occurs on the boundaries, is bounded and we can expect that the approximation fits the solution better in the limit $\nu \to 0$ for fixed Wn^2. We suggest also that the leading form of the correction $j_y^{(a,3)}$ which annihilates the vertical velocity at the X-bounds when $\nu \to 0$, should have a form:

$$\begin{aligned} &j_y^{(a)} = j_y^{(a,1)} + j_y^{(a,2)} + j_y^{(a,3)}, \\ &j_y^{(a,3)} = -(j_y^{(a,1)} + j_y^{(a,2)})|_{X=1} p(k'_w, k''_w, X) X. \end{aligned} \tag{B.34}$$

The function $p(k'_w, k''_w, X) = p(\mathrm{Wn}^2, X)$ differs from zero only very close to the boundaries $X = \pm 1$ when $\mathrm{Wn} \to \infty$ and therefore, $j_y^{(a,3)}$ has a small impact on the derived bulk solution in this limit. Therefore, we conclude that the deficiency of the constructed approximation should decrease in the limit $\mathrm{Wn} \to \infty$ and, for fixed Wn, when $\nu \to 0$.

References

[1] S. Ansumali, I. V. Karlin, Kinetic boundary conditions in the lattice Boltzmann method, Phys. Rev. E, 66 (2002), 26311.

[2] S. Ansumali, I. V. Karlin, S. Arcidiacono, A. Abbas and N. I. Prasianakis, Hydrodynamics beyond Navier-Stokes: Exact solution to the lattice Boltzmann hierarchy, Phys. Rev. Lett., 98 (2007), 124502.

[3] A. M. Artoli, A. G. Hoekstra and P. M. A. Slot, Simulation of a syctolic cycle in a realistic artery with the lattice Boltzmann BGK method, Int. J. Mod. Phys. B, 17(1/2) (2003), 95-98.

[4] M. Bouzidi, M. Firdaouss and P. Lallemand, Momentum transfer of a Boltzmann-lattice fluid with boundaries, Phys. Fluids, 13 (2001), 3452-3459.
[5] C. Cercignani, Theory and Application of the Boltzmann Equation, Scottish Academic, New York, 1975.
[6] R. Cornubert, D. d'Humières and D. Levermore, A Knudsen layer theory for lattice gases, Physica D, 47 (1991), 241-259.
[7] U. Frisch, D. d'Humières, B. Hasslacher, P. Lallemand, Y. Pomeau and J. P. Rivet, Lattice gas hydrodynamics in two and three dimensions, Complex Syst., 1 (1987), 649-707.
[8] I. Ginzbourg, Boundary conditions problems in lattice gas methods for single and multiple phases, Ph.D. Thesis, University Paris VI, 1994.
[9] I. Ginzbourg and P. M. Adler, Boundary flow condition analysis for the three-dimensional lattice Bolzmann model, J. Phys. II France, 4 (1994), 191-214.
[10] I. Ginzbourg and D. d'Humières, Local second-order boundary method for lattice Boltzmann models, J. Stat. Phys., 84(5/6) (1996), 927-971.
[11] I. Ginzburg and D. d'Humières, Multi-reflection boundary conditions for lattice Boltzmann models, Phys. Rev. E, 68 (2003), 066614.
[12] I. Ginzburg, Equilibrium-type and link-type lattice Boltzmann models for generic advection and anisotropic-dispersion equation, Adv. Water Resour., 28 (2005), 1171-1195.
[13] I. Ginzburg, Generic boundary conditions for lattice Boltzmann models and their application to advection and anisotropic-dispersion equations, Adv. Water Resour., 28 (2005), 1196-1216.
[14] I. Ginzburg, Lattice Boltzmann modeling with discontinuous collision components. Hydrodynamic and advection-diffusion equations, J. Stat. Phys., 126 (2007), 157-203.
[15] I. Ginzburg and D. d'Humières, Lattice Boltzmann and analytical modeling of flow processes in anisotropic and heterogeneous stratified aquifers, Adv. Water Resour., 30 (2007), 2202-2234.
[16] I. Ginzburg, F. Verhaeghe and D. d'Humières, Two-relaxation-time lattice Boltzmann scheme: About parametrization, velocity, pressure and mixed boundary conditions, Commun. Comput. Phys., 3 (2008), 427-478.
[17] X. He, L.-S. Luo, Lattice Boltzmann model for the incompressible Navier-Stokes equation, J. Stat. Phys., 88 (1997), 927-945.
[18] X. He, Y. Zou, L.-S. Luo and M. Dembo, Analytic solutions of simple flows and analysis of nonslip boundary conditions for the lattice Boltzmann BGK model, J. Stat. Phys., 87 (1997), 115-135.
[19] F. J. Higuera, S. Succi and R. Benzi, Lattice gas dynamics with enhanced collisions, Europhys. Lett., 9 (1989), 345-349.
[20] F. J. Higuera and J. Jiménez, Boltzmann approach to lattice gas simulations, Europhys. Lett., 9 (1989), 663-668.
[21] D. d'Humières, Generalized lattice-Boltzmann equations, in: Rarefied Gas Dynamics: Theory and Simulations, Progress in Astronautics and Aeronautics, AIAA, Vol. 59, 1992, pp. 450-548.
[22] D. d'Humières, M. Bouzidi and P. Lallemand, Thirteen-velocity three-dimensional lattice Boltzmann model, Phys. Rev. E, 63 (2001), 066702.
[23] D. d'Humières, I. Ginzburg, M. Krafczyk, P. Lallemand and L.-S. Luo, Multiple-relaxation-time lattice Boltzmann models in three dimensions, Philos. T. Roy. Soc. A, 360 (2002), 437-451.
[24] D. d'Humières, Boundary conditions for LB Methods, Lecture Notes, Erlangen, LBM Work-

shop 2001; Lecture Notes, Braunschweig, ICMMES 2004.
[25] M. Junk and Z. Yang, Asymptotic analysis of lattice Boltzmann boundary conditions, J. Stat. Phys., 121 (2005), 3-37.
[26] G. E. Karniadakis and A. Beskok, Micro Flows: Fundamentals and Simulation, Springer, New York, 2002.
[27] P. Lallemand and L.-S. Luo, Theory of the lattice Boltzmann method: Dispersion, dissipation, isotropy, Galilean invariance, and stability, Phys. Rev. E, 61 (2000), 6546-6562.
[28] P. Lallemand and L.-S. Luo, Theory of lattice Boltzmann methods: Acoustic and thermal properties in two and three dimensions, Phys. Rev. E, 68 (2003), 036706.
[29] Y. Liu, R. M. C. So and Z. X. Cui, Bluff body flow simulation using lattice Boltzmann equation with multiple relaxation time, Comput. Fluids, 25 (2006), 951-956.
[30] G. R. McNamara and G. Zanetti, Use of the Boltzmann equation to simulate lattice-gas automata, Phys. Rev. Lett., 61(20) (1988), 2332-2335.
[31] A. Mezhab, M. Bouzidi and P. Lallemand, Hybrid lattice Boltzmann finite-difference simulation of convective flows, Comput. Fluids, 33 (2004), 623-641.
[32] C. Pan, L. Luo and C. T. Miller, An evaluation of lattice Boltzmann schemes for porous media simulations, Comput. Fluids, 35(8/9) (2006), 898-909.
[33] K. N. Premnach and J. Abraham, Three-dimensional multi-relaxation time (MRT) lattice-Boltzmann models for multiphase flow, J. Comput. Phys., 224 (2007), 539-559.
[34] Y. Qian, D. d'Humières and P. Lallemand, Lattice BGK models for Navier-Stokes equation, Europhys. Lett., 17 (1992), 479-484.
[35] M. Sbragaglia and S. Succi, Analytical calculation of slip flow in lattice Boltzmann models with kinetic boundary conditions, Phys. Fluids, 17 (2005), 093602.
[36] V. Sofonea and R. F. Sekerka, Boundary conditions for the upwind finite difference lattice Boltzmann model: Evidence of slip velocity in micro-channel flow, J. Comput. Phys., 207 (2005), 639-659.
[37] S. Succi, I. V. Karlin and H. Chen, Colloquium: Role of the H theorem in lattice Boltzmann hydrodynamic simulations, Rev. Mod. Phys., 74 (2002), 1203-1220.
[38] K. Schladitz, S. Peters, D. Reinel-Bitzer, A. Wiegmann and J. Ohser, Design of acoustic trim based on geometric modeling and flow simulation for non-woven, Comp. Mater. Sci., 38 (2006), 56-66.
[39] J. Tölke, S. Freudiger and M. Krafczyk, An adaptive scheme using hierarchical grids for lattice Boltzmann multi-phase simulations, Comput. Fluids, 35(8/9) (2006), 820-830.
[40] H.-J. Vogel, J. Tölke, V. P. Schulz, M. Krafczyk and K. Roth, Comparison of lattice-Boltzmann model, a full-morphology model, and a pore network model for determining capillary pressure-saturation relationships, Vadoze Zone J., 4 (2005), 380-388.
[41] D. Yu, R. Mei, L.-S. Luo and W. Shyy, Viscous flow computations with the method of lattice Boltzmann equation, Prog. Aerosp. Sci., 39 (2003), 329-367.
[42] H. Yu, L.-S. Luo and S. S. Girimaji, LES of turbulent square jet flow using an MRT lattice Boltzmann model, Comput. Fluids, 25 (2006), 957-965.
[43] J. R. Womersley, Method for the calculation of velocity, rate of flow and viscous drag in arteries when the pressure gradient is known, J. Physiol., 127 (1955), 553-563.